GLOBAL MODELLING OF THE GALACTIC DYNAMO DRIVEN BY COSMIC RAYS

Katarzyna Kulpa-Dybeł

Faculty of Physics, Astronomy and Applied Computer Science
of the Jagiellonian University

A thesis, written under the supervision of
prof. dr hab. Katarzyna Otmianowska-Mazur,
submitted to the Jagiellonian University
for the degree of Doctor of Philosophy

Kraków 2011

Acknowledgements

To my family and to all those who supported and encouraged me over the last 5 years.

Abstract

This work is dedicated to a dynamo action and a magnetic field evolution in different types of galaxies, namely in barred and ringed galaxies. The gas distribution as well as magnetic field structures are significantly different in barred and ringed galaxies than in normal spiral galaxies. To understand correctly physical processes occurring in galaxies we cannot focus only on normal spiral galaxies, but we have to study more complicated cases like bars and rings in galaxies.

The thesis presents the global evolution of the magnetic field and the interstellar medium of barred and ringed galaxies in the presence of nonaxisymmetric components of the gravitational potential, i.e. the bar and/or the oval. The magnetohydrodynamical dynamo is driven by cosmic rays, which are continuously supplied to the galactic disk by supernovae remnants. Additionally, a weak, dipolar and randomly oriented magnetic field is injected to the galactic disk during supernovae explosions. No magnetic field is present at the beginning of simulations. To compare my results directly with the observed properties of galaxies I constructed realistic maps of high-frequency polarized radio emission.

The main result is that the cosmic ray driven dynamo can amplify weak magnetic fields up to a few μG within a few Gyr in barred and ringed galaxies. In the case of the fastest amplification the e-folding time is equal to 104 Myr and the magnetic field reaches equipartition at time $t \sim 1.8$ Gyr. A completely random initial magnetic field evolves into large scale structures. In most models the even (quadrupole-type) configuration of the magnetic field with respect to the galactic plane can be observed. Only in one model the odd (dipole-type) symmetry is obtained.

The modelled magnetic field configuration resembles maps of the polarized intensity observed in barred galaxies. The modelled polarization vectors are distributed along the bar and between spiral gaseous arms. The drift of magnetic arms is observed during the whole simulation time. In the case of the simulated ringed galaxy NGC 4736, the cosmic ray driven dynamo also works, however the obtained synthetic polarization maps do not reflect all properties of the magnetic field visible in observations. To better reproduce all observational futures in NGC 4736 more complex numerical analysis is needed.

Many theoretical studies suggest that the galactic dynamo is responsible for the most of observational properties of the magnetic field in barred and ringed galaxies. For the first time this prediction is confirmed numerically and the obtained results are present below in this dissertation.

Contents

List of Figures

List of Tables

List of Symbols

a_{bar}	length of bar major axis
a_b	length scale of the bulge
a_d	length scale of the disk
a_{oval}	length scale of oval major axis
a_h	length scale of the halo
b_{bar}	length scale of bar minor axis
b_d	height scale of the disk
b_{oval}	length scale of oval minor axis
B	magnetic field
B^2	total magnetic field energy
B_{mean}	mean magnetic field
B_φ	azimuthal magnetic field
B_φ^{arms}	azimuthal magnetic field in magnetic arms in barred galaxy
B_φ^{bar}	azimuthal magnetic field in the bar in barred galaxy
B_φ^{ir}	magnetic field in the inner ring in NGC 4736
B_φ^{od}	magnetic field in the outer disk in NGC 4736
BS1, BS2, BS3, BS4, BS5	models of the barred galaxy
c_{bar}	length scale of bar vertical axis
c_{oval}	length scale of oval vertical axis
CR	corotation radius
c_s	speed of the sound
e_{cr}	cosmic ray energy
E_{mag}	magnetic field energy
f_{SN}	supernova frequency
IILR	Inner Inner Lindblad Resonance
ILR	Inner Lindblad Resonance
$K_\parallel$	parallel cosmic ray diffusion coefficient
$K_\perp$	perpendicular cosmic ray diffusion coefficient

M_b	bulge mass
M_{bar}	bar mass
M_d	disk mass
M_h	halo mass
M_{lost}	rate of mass outflow
M_{oval}	oval mass
OLR	Outer Lindblad Resonance
OILR	Outer Inner Lindblad Resonance
p	pitch angle
p_{cr}	cosmic ray pressure
p_{gas}	gas pressure
p_{mag}	magnetic field pressure
r_{SN}	SN radius
R_{CR}	CR position
RM (BS4)	reference model of the barred galaxy
R_{BG}	barred galaxy radius
R_{RG}	ringed galaxy radius
R_{ILR}	ILR position
R_{IILR}	IILR position
R_{OILR}	OILR position
R_{OLR}	OLR position
RS1, RS2, RS3, RS4, RS5	models of the ringed galaxy
SN	supernova
SFR	star formation rate
v	gas velocity
η	resistivity coefficient
ρ	gas denisty
τ	e-folding time
Ω_{bar}	bar angular velocity
Ω_{oval}	oval angular velocity

Chapter 1

Astrophysical context

1.1 Introduction

Magnetic fields are ubiquitous and exist in a wide variety of plasma environments. Both observations and numerical simulations indicate that magnetic fields are major agents in the interstellar and intracluster media. Magnetic fields play a crucial role in many astrophysical processes and bodies, e.g. they are vital in a formation of stars, as they remove an excess of angular momentum and stabilize gas clouds which results in reducing the star formation efficiency to the observed values (Price & Bate 2009), they are also probably crucial in protoplanetary disks, accretion disks, a formation and stability of jets, supernova (SN) remnants and galaxies. The idea of the global magnetic field of the Milky Way was proposed about 50 years ago, and that of external spiral galaxies about 30 years ago. It now seems clear that ordered, microgauss-level magnetic fields are common in spiral (normal and barred) galaxy disks and halos (Beck 2009b). It is wildly accepted that understanding the role of magnetic fields in the formation and structure of galaxies is central to understanding the evolution of galaxies. Although in the last decade, there has been significant progress in studies of magnetic fields of galaxies, many important questions, especially about magnetic field structures in barred and ringed galaxies, remain unanswered. For instance, we still do not know when were the first magnetic fields generated (in young galaxies or in the early Universe before galaxies were formed) or how important magnetic fields are for the physics of galaxies (do they influence a structure formation or a gas outflow). Most of the observed properties of magnetic fields in barred and ringed galaxies can be theoretically explained by the dynamo action and the gas distribution disturbed by the nonaxisymmetric gravitational potential of the bar and/or oval (Beck et al. 2002). However, global numerical simulations confirming this predication have not been made until now.

1.2 General observational properties of barred galaxies

Bars are ubiquitous and occur in all types of disk galaxies, from early to late Hubble types (Sandage & Bedke 1988). They can be found in large lenticular galaxies (Aguerri et al. 2005), in a significant fraction of spiral galaxies (Eskridge et al. 2000) and even in almost all Magellanic-type galaxies (Odewahn 1996; Valenzuela et al. 2007). In optical images almost half of all the nearby disk galaxies are barred (Marinova & Jogee 2007; Reese et al. 2007; Barazza et al. 2008). However, when near-infrared (NIR) images are used the fraction of barred galaxies increases to about 70% (Eskridge et al. 2000; Knapen et al. 2000; Menéndez-Delmestre et al. 2007). This is caused by the fact, that NIR observations are more sensitive to older stellar populations which are usually major parts of bars. The main properties of barred galaxies, such as the size of the bar relative to the galaxy size, the number of spiral arms in the outer disk, the degree of overall symmetry or the gas and dust content can be significantly different in different galaxies.

1.2.1 Dynamical structure

Bars are astrophysically important not only because they are very common in disk galaxies, but also because they can significantly affect a gas distribution. Radio observations of barred galaxies show that gas is accumulated in the central part of the disk and forms elongated structure called a bar (Sellwood & Wilkinson 1993). Bars are elongated, thus the gravitational potential produced by them is nonaxisymmetric. This potential causes that in the inner part of the disk the offset leading shocks are created, which are responsible for significant compression of the gas observed as dust lanes (Sandage 1961; Beck et al. 2002). The key role of a bar in formation of structures mentioned above was confirmed by numerical models (Athanassoula 1992; Piner et al. 1995). In those models the relation between the size of a bar and the degree of curvature of a main dust lanes was found, namely stronger bars have straighter dust lanes. Additionally, it is thought that the gravitational potential of a rotating bar drives interstellar gas through torques and dynamical resonances into spiral arms and rings, which are visible in observations of barred galaxies (e.g Erwin & Sparke 2002). Various theoretical studies (Lindblad 1960; Toomre 1969; Athanassoula 1992; Romero-Gómez et al. 2007; Kulesza-Żydzik et al. 2009, 2010) have shown that spiral arms are created due to the gas redistribution caused by a stellar bar. The observational correlation between bars and spirals is hard to be confirmed and has been widely considered in the literature. Some authors (Block et al. 2004; Buta et al. 2005, 2009) claimed that the correlation between a bar and a spiral exists while others (Seigar et al. 2003; Durbala et al. 2009) did not find any correlation. The recent and more detailed studies of observations made by Salo et al. (2010) have confirmed that spiral arms are driven by the bar both in early and late type of barred galaxies.

The length of the major axis of the bar a_{bar} is always smaller than the total galaxy size R_{25}, where R_{25} is a diameter at which the surface brightness of the galaxy falls below 25 magnitudes per square second of arc in blue (Elmegreen & Elmegreen 1985). Taking into account the above property, barred galaxies can be divided into two groups: early type galaxies when the ratio a_{bar}/R_{25} ranges from 0.2 to 0.3 and late type galaxies with the ratio a_{bar}/R_{25} larger than 0.3 and smaller than 0.6. What is more, for early type galaxies the ratio of the bar's major a_{bar} and minor b_{bar} axes is between $b_{bar}/a_{bar} = 0.3 - 0.1$, while bar in late type galaxies are more elliptical, shorter and weaker than their earlier counterparts (Sellwood & Wilkinson 1993).

The bar pattern speed Ω_b is one of the most important parameters which plays crucial role in the evolution of barred galaxies. The disk of a galaxy rotates differentially with the circular angular velocity Ω, while the bar rotates like a solid body. Resonances occur where the circular angular velocity of the disk and the bar pattern speed satisfy the following relationship of commensurability:

- $\Omega = \Omega_b$ - the most fundamental resonance called corotation radius (CR),
- $\Omega = \Omega_b - \kappa/2$ - the so-called Inner Lindblad[1] Resonance (ILR),
- $\Omega = \Omega_b + \kappa/2$ - the so-called Outer Lindblad Resonance (OLR),

where

$$\kappa = \frac{2\Omega}{R}\frac{d}{dR}(R^2\Omega) \tag{1.1}$$

is the epicyclic frequency and R is the radial coordinate. One of the most important relation which was found is that bars end just before the position of CR, thus $\mathcal{R} = R_{CR}/a_{bar} = 1.2 \pm 0.2$ (e.g Lindblad et al. 1996). What is more, the gas content is accumulated at resonances and a long-lived spiral structure can only exist between the ILR and the OLR (Sellwood & Wilkinson 1993).

The bar pattern speed controls a barred galaxy's dynamics and morphology, thus it is very important to determine Ω_b correctly. Usually, the bar pattern speed is parametrized by the ratio of the corotation radius R_{CR} to the length of the bar a_{bar} mentioned above. Following Corsini et al. (2007), longer bars end near the CR ($1.0 \leq \mathcal{R} \leq 1.4$) and are called fast, while slow bars are shorter ($\mathcal{R} > 1.4$). To specify the bar rotation parameter $\mathcal{R}$ the bar pattern speed, which is very hard to measure, is required. For late type barred galaxies a variety of indirect methods is used to determine the pattern speed of bars (Corsini 2010). They are based on the gas distribution and kinematics and allow to specify the value of the pattern speed from e.g. location of rings (Vega Beltrán et al. 1998) or from a comparison of velocity field data to dynamical models of a gas flow (Lindblad et al. 1996). The

[1] Named after Bertil Lindblad 1895-1965.

bar pattern speed can also be measured directly using the Tremaine-Weinberg method (Tremaine & Weinberg 1984), however this method is used mainly for early type barred galaxies (Corsini et al. 2007).

Many observations have shown (e.g Tubbs 1982) that the star formation rate (SFR) is not uniform in barred galaxies. Gas is driven to the centre by the bar's gravity torques, where it is transformed into young stars. For late type barred galaxies the star formation regions are observed along the whole bar, while for early type barred galaxies star formation regions are visible near the centre and/or at the ends of the bar. However, the average global SFR in barred galaxies is similar to the one found in unbarred galaxies (Phillips 1996).

1.2.2 Rings formation

About 50% of all spiral disk galaxies possess ring-like or pseudoring-like patterns (de Vaucouleurs 1963). Rings are usually related to barred galaxies, however they can also be found in nonbarred systems (Buta & Combes 1996). They are divided into three major categories: nuclear, inner and outer, and were classified by Buta (1986) as *nr*, *r*, and *R*, respectively. Nuclear rings surround the nucleus and are much smaller in size than the bar. The radius of the nuclear ring cannot be larger than one-quarter the size of the bar (Knapen 2010). Inner rings occur near the ends of the bar, while outer rings are the largest rings and they are bigger than the bar. When the structure of outer rings is unclosed or incomplete they are referred to as pseudorings and denoted by R'.

It is generally accepted that galactic rings are formed in galactic disks due to gravitational torques from bar-like patterns. The origin of the ring-like pattern has been studied by many authors (e.g. Schwarz 1981, 1985; Buta 1999). They suggested that rings are created by gas accumulation at the Lindblad resonances. Then, the ILR is linked to nuclear rings, the CR is associated with inner rings and the OLR is related to outer rings. Although, density waves have been commonly assumed to be responsible for formation of rings in barred galaxies, another theoretical model was proposed by Romero-Gómez et al. (2006, 2007). In this model rings are related to the invariant manifolds of orbits near unstable Lagrangian points. The same model is also used to explain the generation of two-armed, grand design spirals in barred galaxies. This theory is a possible alternative, however, to decide which one from the theories mentioned above is better (or maybe they complete each other), more theoretical and observational work is necessary (Athanassoula et al. 2009).

Rings in nonbarred systems may be related to resonances effects produced by a spiral mode. They also may be induced by tidal actions from a gravitationally bounded companion (Silchenko & Moiseev 2006) or by a past bar which is now dissolved (Athanassoula 1996).

Rings in nonbarred as well as in barred galaxies are active zones of star formation. Gas accumulated in rings usually changes phase from neutral to molecular as it is submitted to higher pressures. This may result in a strong enhancement of the SFR in rings. Recent results obtained by Grouchy et al. (2010) have shown that the SFR in rings (both in barred and nonbarred galaxies) depends weakly or does not depend on the strength of a nonaxisymmetric perturbation.

1.3 Magnetic fields in galaxies

Magnetic fields are ubiquitous in spiral, barred (Beck et al. 2002) and irregular galaxies (Chyży et al. 2000, 2003). They control the creation of structures in the interstellar medium as well as the distribution of cosmic rays. Magnetic fields in galaxies need illumination to be detectable and can be observed using indirect methods only. Information about magnetic fields distribution and strength is usually obtained from polarized emission at optical, infrared, submillimeter and radio wavelengths (Sofue et al. 1986; Beck 2009b). The optical polarization of star light is caused by the alignment of interstellar dust grains by magnetic fields in the interstellar medium (Davis & Greenstein 1951). However, light can also be polarized by simple scattering and it is difficult to estimate how much of the polarization is in fact due to magnetic alignment. Polarization measurements at infrared and submillimeter wavelengths are not affected by scattered light, hence the polarization originates in emission of dust particles aligned by a magnetic field (e.g Hildebrand et al. 2000). At radio wavelengths linearly polarized waves are produced by relativistic electrons accelerated in magnetic fields (synchrotron emission, Pacholczyk (1970)). The Faraday effect can be used to determine the strength and direction of the regular magnetic field component along the line of sight (Beck 2009a). The most direct method to measure the strength of magnetic fields in gas clouds of the Milky Way and in sturburst galaxies is the Zeeman splitting of spectral emission lines (Robishaw et al. 2008).

The large scale structure of the magnetic field in galaxies is generally represented as a superposition of modes with different azimuthal and vertical field directions and symmetries. In disks of galaxies the axisymmetric spiral (ASS) mode is the strongest mode, however the bisymmetric spiral mode (BSS) or a mixture of both with a preponderance of one of the two shapes is also observed. In Figure 1.1 a schematic view of the ASS and the BSS mode is presented. Rotation measure observations show that the ASS magnetic field exists in several galaxies, e.g., in M31 (Sofue &Takano 1981), IC 342 (Sokoloff et al. 1992) or LMC (Gaensler et al. 2004). The BSS mode has been with no doubt observed only in one galaxy, namely in M81 (Sokoloff et al. 1992). Many others observations indicate that the BSS mode can also exists in few more galaxies, e.g., in M33 or NGC 2276

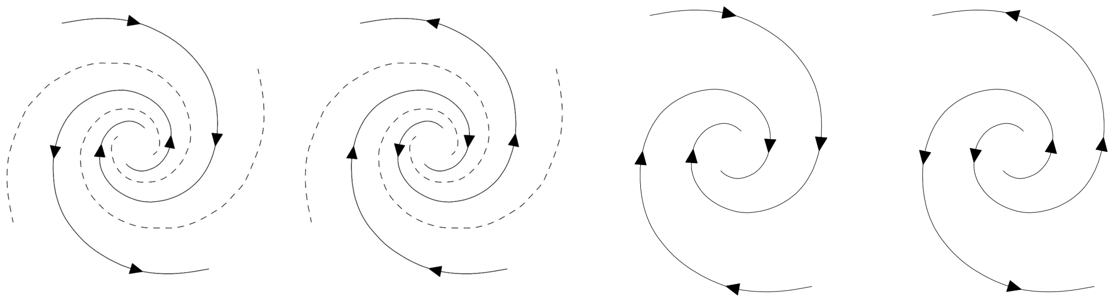

Figure 1.1: The bisymmetric (BSS, two left figures) and the axisymmetric (ASS, two right figures) magnetic field spirals. In the BSS mode the magnetic field is directed inwards along one gaseous arm and outwards along the other one. In the ASS mode the direction of the magnetic field is the same in the whole galactic disk and in different galaxies can be directed inwards or outwards.

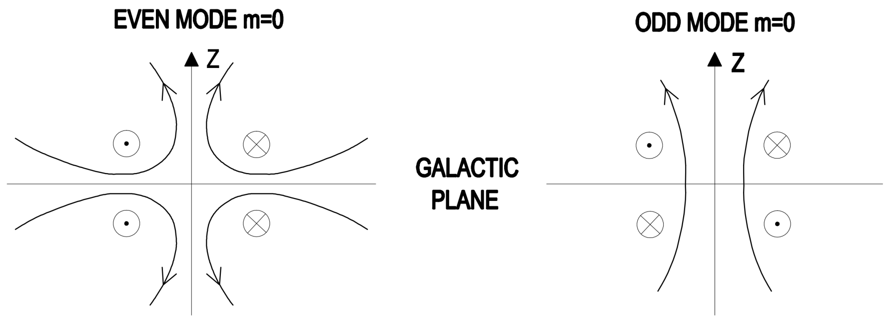

Figure 1.2: The even (quadrupolar, left figure) and the odd (dipolar, right figure) symmetry of the magnetic field with respect to the galactic plane. The direction of the magnetic field is marked by symbols: ⊙ - out of the page and ⊗ - into the page.

(Hummel & Beck 1995). The vertical symmetry perpendicular to the disk plane can be the even (quadrupolar) or the odd (dipolar) (Figure 1.2). It appears that galactic magnetic fields should have the even symmetry rather than the odd one. This is caused by the fact that global magnetic fields of spherical objects (including stars and planets) are likely to be predominantly dipolar, whereas those of flat objects (spiral galaxies) are quadrupolar. Although a clear ASS or BSS mode was detected in several galaxies, most of magnetic field structures seem to be a superposition of different dynamo modes. This may be a result of many processes occurring in disks of galaxies which may be correlated with density waves, shocks, bars or even with collisions and interactions of galaxies (Beck et al. 1996; Krause 2004).

1.3.1 Interstellar medium

Magnetic fields are one of three basic agents of interstellar media (ISM) of galaxies. The other two components are cosmic ray gas and ordinary matter (gas and dust) (Duric 1999). A cosmic ray gas consists of relativistic electrons, protons and heavier atomic nuclei. The galactic cosmic ray energy density is $1\,\mathrm{eVcm^{-3}}$ and the corresponding number density is about $10^{-10}\,\mathrm{cm^{-3}}$. This value is significantly smaller than the average thermal density ($0.1-1\,\mathrm{cm^{-3}}$), thus cosmic rays are weightless pressure components of the ISM. Since cosmic rays are usually charged particles, they are affected by the Lorentz force, i.e. they are coupled to magnetic fields. Because of the high electric conductivity of plasma, magnetic field lines follow plasma flows (the frozen-in condition). Thus magnetic fields are also coupled to the thermal background plasma. Consequently, three main components of the ISM, magnetic fields, gas and cosmic rays are dynamically coupled, i.e. an energy excess of each component can be converted into energy of other two components until equilibrium is reached (Hanasz & Lesch 2000). In other words, the cosmic ray gas is an essential dynamical ingredient of the ISM of galaxies because its energy density is comparable to the energy density of the magnetic field, thus the magnetic field and cosmic rays are in equipartition.

The strength of the total and regular magnetic field can be derived from the intensity of the total synchrotron emission if the equipartition mentioned above between the energy densities of the total magnetic field and the total cosmic rays is assumed (Beck & Krause 2005). Then, the typical average strength of the total magnetic field in spiral galaxies is about $10\,\mu$G (Beck 2009b). Mean equipartition strengths of the total magnetic field range from about $5\,\mu$G in radiofaint galaxies, like M33 (Buczilowski & Beck 1991), up to about $30\,\mu$G in gas rich galaxies with high star formation rates, like M51 (Fletcher et al. 2004).

1.3.2 Magnetic fields in barred galaxies

The nonaxisymmetric gravitational potential of the stellar bar strongly influences not only the motion of gas and stars in a galaxy, but also the magnetic field distribution. Radio polarization observations of barred galaxies (e.g Beck et al. 2002, 2005; Harnett et al. 2004) show that their magnetic field topology is significantly more complicated than in the case of grand-design spiral galaxies.

The first systematic observations of the polarized radio emission from a sample of 20 barred galaxies was made by Beck et al. (2002). Little or no polarized radio emission was detected in galaxies with large bars but small amount of gas and low star formation rate (NGC 1300 and 1433) or in small galaxies (NGC 1313, 1493 and 5068). In other galaxies the radio continuum morphology is formed as a result of star formation in spiral arms. The nearby barred galaxy NGC 1365 is the best example in this sample. In Fig. 1.3 the total (left panel) and polarized (right panel) intensity as well as the observed magnetic field vectors (dashes) for NGC 1365 galaxy are overlayed onto an optical image (both Figures were taken from Beck et al. (2002)). According to Fig. 1.3 the main magnetic field features observed in NGC 1365 can be summarized as follows. The polarized emission is strongest in the central part of the galaxy, where the bar is present. In this region the

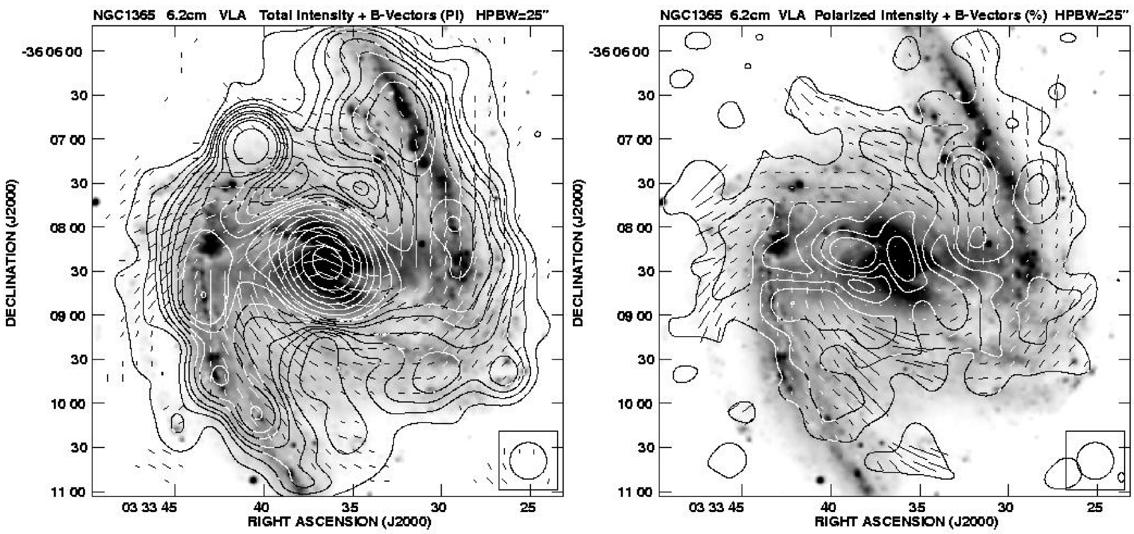

Figure 1.3: *Left panel:* The total intensity contours and magnetic field vectors of NGC 1365 at $\lambda = 6.2$ cm superimposed on the optical image. *Right panel:* The polarization map at $\lambda = 6.2$ cm of the barred galaxy NGC 1365. Polarized intensity (contours) and polarization angles (dashes) are superimposed on the optical image and were taken from (Beck et al. 2002).

polarized emission forms ridges coinciding with the dust lanes along the leading edges of the bar. The observed enhancement of the polarized emission is probably caused by shock compression of isotropic random fields into anisotropic ones. In the radio ridges the total radio intensity is also very strong and this amplification can be explained by shearing and shock compression of the isotropic random magnetic field. What is more, the enhancement of the total intensity is much higher than that of the polarized intensity. This disparity is observed because the regular magnetic field is strong enough to resist shearing and hence the amplification of the total magnetic field by shear is reduced[2]. Using the same argument, the difference between the magnetic and velocity fields in the dense gas in front of the ridges can be explained. The polarization vectors change quickly their pitch angles in the bar region whenever they are located upstream the dust lanes and this results in the depolarization valley where the polarized emission almost vanishes. Near shear shock areas the regions of vanishing polarized intensity are also observed. In the outer disk magnetic field vectors form a spiral pattern with the maxima of emission along spiral gaseous arms and in interarm regions. This spiral shape of the magnetic field and large pitch angles indicate that the galactic dynamo works in this galaxy. Similar properties of a magnetic field have been also observed in NGC 1672, NGC 7552 and NGC 1097. Polarization maps of the latter galaxy show that in the southern bar the value of pitch angle violently jumps from about $-15°$ to about $-75°$(Beck et al. 2005). This

[2]Strong regular magnetic field is coupled to diffuse gas and decoupled from dense gas. This causes that the Maxwell stress is strong enough to resist the development of a shear flow in diffuse gas (Beck et al. 2005).

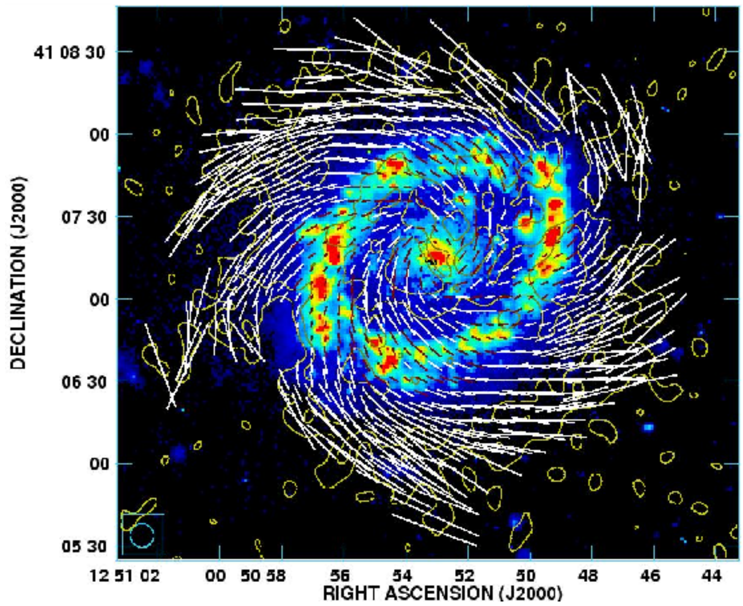

Figure 1.4: The polarization map at 8.46 GHz of the ringed galaxy NGC 4736 taken from Chyży & Buta (2008). The polarized intensity (contours) and polarization angles (dashes) are superimposed on the Hα image (Knapen et al. 2003).

behaviour may result from shearing of the regular magnetic field.

The average total (polarized and unpolarized) magnetic field strength for this sample of barred galaxies is $10 \pm 3\,\mu$G and is comparable to the mean equipartition value of $11 \pm 4\,\mu$G obtained for the sample of 146 late type galaxies (Fitt & Alexander 1993). The average regular magnetic field, calculated from polarized radio emission, is equal to $2.5 \pm 0.8\,\mu$G. The strongest total magnetic field is detected in the central star-forming regions (about $60\,\mu$G in NGC 1097) and in the radio ridges along bars of galaxies ($20\,\mu$G – $30\,\mu$G in NGC 1365). In spiral arms of barred galaxies the total magnetic field is about $20\,\mu$G, while the regular one is $4\,\mu$G.

1.3.3 Coherent spiral magnetic field in NGC 4736

Radio observations of the magnetic field distribution in ringed galaxies are excellent examples which can help us understand and explain the process of the generation of magnetic fields in disk galaxies. Figure 1.4 shows the distribution of the polarization angle and the polarized intensity superimposed onto the column density of gas within the nearest and the largest ringed galaxy NGC 4736 (Chyży & Buta 2008). This galaxy possesses a well visible inner gaseous ring with active zones of star formation. The magnetic field does not follow the gas distribution as expected under the assumption of passively advected magnetic fields and what is usually observed in grand-design spirals. Instead magnetic vectors cross the inner ring at a remarkably large and constant pitch angle of about $-35°$. Additionally, the distribution of the Faraday rotation measure is asymmetric and the strength of the magnetic field is up to 30 μG and 13 μG in the total and regular magnetic field, respectively. The magnetic field properties mentioned above strongly support the idea that the observed magnetic field structure within ringed galaxy NGC 4736 is caused by a pure large-scale MHD dynamo action (Chyży & Buta 2008).

1.4 Dynamo action in galaxies

To explain the origin of magnetic fields in galaxies two major models have been proposed: a primordial field and the dynamo theory (Kronberg 1994). The first model assumes that the large scale magnetic field observed in galaxies is just a primordial magnetic field twisted by a differential rotation. However, this very simple theory cannot explain the basic properties of the magnetic field in galaxies. For example, the large scale magnetic fields observed in galaxies have pitch angles ($p = \arctan B_r/B_\Phi$) between $-10°$ and $-35°$ [3] (Beck 1993), while the magnetic spiral produced by the differential rotation of the primordial field has the pitch angle of the order of $-1°$ (Shukurov 2002). The main argument against this model is the decay time of the large scale primordial magnetic field. If the primordial magnetic field does not need any support except the differential rotation, then due to the turbulent diffusivity any ordered magnetic field component will disappear within about 0.7 Gyr (Rohde et al. 1998). On the other hand, the dynamo theory is capable of maintaining and reproducing observed large scale magnetic fields in galaxies. Thus, to explain observational properties of the magnetic field in spiral, barred and ringed galaxies the dynamo action is necessary. To sum up, it is thought that the dynamo action can be responsible for the following observational properties of the large scale magnetic field in galaxies (most of them cannot be explained using the primordial magnetic field model):

- amplification of galactic magnetic fields up to several μG within a lifetime of a few Gyr,
- maintenance of the created magnetic fields in a steady state (magnetic energy in a turbulent flow rapidly cascades towards small scales and dissipates),
- large magnetic pitch angles between $-10°$ and $-35°$ (Beck 1993),
- vertical symmetry: even (quadrupolar) or odd (dipolar) of the observed regular magnetic field with respect to the plane of a galaxy,
- azimuthal symmetry: the ASS or the BSS mode, the dynamo theory favours the ASS mode, while the primordial theory the BSS mode,

[3] The negative value of the pitch angle indicates that the magnetic spiral is trailing with respect to the galactic rotation.

- magnetic field which does not follow the gas distribution, i.e. magnetic fields in NGC 4736 crossing the inner gaseous ring without any change of their direction (Chyży & Buta 2008) or magnetic arms in NGC 1365 which are located between gaseous spirals and the central part of the galaxy (Beck et al. 2002).

1.5 Cosmic ray driven dynamo

One of the most common approaches to the dynamo problem is the mean field dynamo model. The mean field dynamo theory (Ruzmaikin et al. 1988) can explain magnetic fields in many contexts: the Earth, the Sun, or stars. In galaxies the mean field dynamo allows the generation of the regular large scale magnetic field as a result of the joint action of differential rotation Ω and helical turbulent motions of interstellar gas (the so-called α-effect). However, in the case of galaxies the classical kinematic dynamo gives rather small timescale of the magnetic field amplification, i.e., about 10^9 yr. This timescale is too long to explain strong magnetic fields in high redshift galaxies beyond $z = 1$ (Bernet et al. 2008). A faster amplification is possible when the cosmic ray driven dynamo (Parker 1992; Hanasz et al. 2004, 2006) is used. This dynamo is based on two principle effects: First, the cosmic ray energy is continuously supplied by SNe remnants to the galactic disk, which becomes unstable due to the Parker instability. Second, the fast turbulent magnetic reconnection (Lazarian & Vishniac 1999; Kowal et al. 2009) allows small scale loops of a magnetic field to merge into large scale coherent structures in the limit of vanishing resistivity.

Another model of the fast galactic dynamo, the so-called supernova driven dynamo, was proposed by Gressel et al. (2008). In their model they assumed that the thermal energy is injected to the galactic disk during a SN explosion, while the cosmic ray component is neglected (this is in contrast to the cosmic ray driven dynamo model, where the cosmic ray energy is introduced to the galactic disk during a SN explosion, while the thermal energy is not taken into account). In the supernova driven dynamo the authors also applied a cooling and a heating function to reflect the multi-phase nature of the ISM. Numerical simulations in the shearing box approximation have shown that the supernova driven dynamo causes an exponential amplification of a magnetic field and can explain many observational features of magnetic fields in galaxies. However, in their method the time step for the cooling and the heating functions is very small. In fact, the computational cost of the global simulation of the supernova driven dynamo in barred and ringed galaxies far exceeds the amount of computational resources available[4].

[4]All numerical simulations presented here have been performed on the GALERA supercomputer in TASK Academic Computer Centre in Gdańsk. The GALERA cluster consists of 5376 cores.

1.5.1 Parker instability

The cosmic ray gas plays essential roles in the dynamics of the ISM because the energy density of cosmic rays is of the same order as that of the magnetic field and thermal gas (see Subsection 1.3.1). Relativistic electrons in the cosmic ray gas are accelerated by shocks which are produced during SNe explosions (Reynolds 1996). It was estimated that about $10 - 50\%$ of the total 10^{51} erg kinetic energy output from a single SN is converted to the cosmic ray energy (Jones et al. 1998). What is more, Giacalone & Jokipii (1999) showed that the cosmic ray gas diffuses anisotropically along magnetic field lines. Parker (1966, 1967) proposed that the ISM (which is composed of gas, magnetic fields and cosmic rays) stratified by vertical gravity in galactic disks becomes unstable against the Parker instability (PI). The reason for the instability is the buoyancy of the weightless ISM components, i.e. a magnetic field and cosmic rays. Although, the contribution of these components to the total pressure is significant, they do not contribute to the mass density of the ISM. When the PI works in a galactic disk, magnetic lobes are formed, which extend outward the disk to the distance of an order of 1 kpc. For a more detailed description of the PI I refer the reader to Appendix B.0.2.

1.5.2 Fast magnetic reconnection

In order to allow the cosmic ray driven dynamo to work smoothly, magnetic reconnection must proceed at speeds characteristic of local dynamical velocities. In other words the reconnection rate has to be comparable to the local Alfvén velocity. In that case, the magnetic reconnection is fast, which means that it does not depend on the resistivity or depends on the resistivity logarithmically (see Parker 1979). The first three dimensional (3D) model of the fast magnetic reconnection was proposed by Lazarian & Vishniac (1999). Their model is based on the Sweet-Parker reconnection scheme, where two oppositely directed magnetic field lines are brought into contact. However, it also includes effects of turbulence and substructure in the magnetic field. In this model the reconnection rate does not depend on the resistivity, but is determined only by turbulence, in particular by its strength and an injection scale. The results of numerical analysis (Kowal et al. 2009) confirmed that the reconnection rate in the Lazarian & Vishniac (1999) model is insensitive to the resistivity and depends only on turbulence properties. It is important to note that the magnetic reconnection model described above is fast only in 3D. Reconnection in 2D depends on the resistivity and is not fast (Kulpa-Dybeł et al. 2010).

1.5.3 Numerical model of the cosmic ray driven dynamo

The original concept of the fast cosmic ray driven dynamo was proposed by Parker (1992). Several researchers have approached this problem numerically, e.g. Hanasz et al. (2004, 2006); Otmianowska-Mazur et al. (2007); Siejkowski et al. (2010). According to authors listed above this dynamo involves the following elements. Cosmic rays are continuously supplied to the galactic disk due to SNe explosions. As was mentioned above the galactic disk stratified by gravity is unstable against the PI. Buoyancy effects induce the formation of magnetic loops in the frozen-in, predominantly horizontal magnetic fields. The rotation of the interstellar gas causes that magnetic field loops are twisted by the Coriolis force. Next, due to the fast magnetic reconnection small scale magnetic loops merge to form the large scale radial magnetic field component. The newly created magnetic field component is stretched by differential rotation, which results in the amplification of the large scale toroidal magnetic field component. Combined action of these effects is sufficient to trigger the exponential growth of the large scale magnetic field on timescales of $140 - 250$ Myr (Hanasz et al. 2006), which are comparable to the galactic rotation period.

Many 3D MHD numerical simulations in the shearing-box approximation have shown that the cosmic ray driven dynamo can exponentially amplify weak magnetic fields up to a few μG within a few Gyr in spiral galaxies (Hanasz et al. 2004, 2006, 2009a) as well as in irregular galaxies (Siejkowski et al. 2010). What is more, some of the observed magnetic fields' properties such as extended halo structures of edge-on galaxies, the so called X-shaped structures (Soida 2005; Krause 2009), can be explained using the cosmic ray driven dynamo (Otmianowska-Mazur et al. 2009). The first complete global-scale 3D numerical model of the cosmic ray driven dynamo has been demonstrated recently by Hanasz et al. (2009b). These simulations have given very interesting results and have shown that the CR driven dynamo is one of the most promising processes responsible for the amplification and maintance of galactic magnetic fields.

1.5.4 Seed fields

Any dynamo requires a seed field, however, the origin of the first magnetic fields in the Universe is still one of the most challenging problems in modern astrophysics (e.g Kulsrud & Zweibel 2008). Two different views on the generation of seed fields are being taken into account: one possibility is that seed fields can be essentially of cosmological (primordial) origin and the other possibility is that seed fields are generated in astrophysical processes occurring in the ISM. A variety of cosmological processes taking place in the early Universe were proposed. For example, magnetic fields may be generated in various phase transition, like the electroweak transition (Quashnock et. al. 1989) and the quark-hadron phase transition (Quashnock et. al. 1989), or during the Inflation era (Turner & Widrow 1988). These processes lead to the creation of very tiny magnetic fields of about $10^{-20} - 10^{-25}$ G (Widrow 2002; Subramanian 2010).

Another possibility is the generation of the seed fields due to astrophysical processes, such as the Biermann battery (Syrovatskii 1970; Xu et al. 2008). In this scenario, even if magnetic fields are initially absent in a star, a weak field is produced via the Biermann mechanism due to different inertia of electrons and ions. The newly created tiny magnetic fields are amplified by stellar dynamo. Next, a star may explode as a SN and release magnetized material which spreads into the ISM. Reese (1987) suggested that Crab-type SNe remnants have fields of an order of 10^{-4} G. He also estimated that in the early stage of the galactic evolution there could be 10^6 randomly oriented SNe remnants similar to the Crab Nebula, which may lead to rather significant seed fields of an order of 10^{-9} G. The recent simulations made by Hanasz et al. (2009b) have shown that small scale magnetic fields of stellar origin can be amplified exponentially by the cosmic ray driven dynamo to the observed values. It means that SNe explosions can produce a sufficiently strong seed field for the cosmic ray dynamo action.

Chapter 2

Numerical setup

2.1 Method

I performed all numerical simulations with the aid of the Godunov code (Kowal et al. 2009) based on the following methods:

- a third higher-order shock-capturing Godunov-type scheme and the essentially non oscillatory spatial reconstruction (see Londrillo & Del Zanna 2000; Del Zanna et al. 2003),
- a multi-state Harten-Lax-van Leer (HLLD) approximate Riemann solver for isothermal MHD equations (Mignone 2007),
- a second higher-order Runge-Kutta time integration (see Del Zanna et al. 2003).

The divergence of a magnetic field must vanish everywhere at all times ($\nabla \cdot \vec{B} = 0$). This condition is satisfied when the field interpolated constraint transport (CT) scheme based on the staggered grid is used (see Evans & Hawley 1988). All these methods together cause that the Godunov code is very efficient, robust and numerically stable. Additionally, the Godunov code has been extensively tested and successfully used by several authors (Kowal et al. 2009; Kulesza-Żydzik et al. 2009; Falceta-Gonçalvesal et al. 2010; Kulesza-Żydzik et al. 2010) working on different astrophysical processes.

During my calculations I used two clusters:

- the OCTOPUS cluster (48 CPUs) in the Astronomical Observatory of the Jagiellonian University - test problems,
- the GALERA supercomputer (5376 CPUs) in TASK Academic Computer Centre in Gdańsk - main simulations.

One simulation performed on the GALERA cluster takes approximately 74k CPU hours.

2.1.1 Basic equations

I investigated the evolution of galaxies using the magnetized fluid approximation governed by the isothermal non-ideal MHD equations of the form

$$\frac{\partial \rho}{\partial t} + \nabla \cdot (\rho \vec{v}) = 0, \tag{2.1}$$

$$\frac{\partial \vec{v}}{\partial t} + (\vec{v} \cdot \nabla)\, \vec{v} = -\frac{1}{\rho} \nabla \left(p + p_{cr} + \frac{B^2}{8\pi} \right) + \frac{\vec{B} \cdot \nabla \vec{B}}{4\pi\rho} - \nabla\Phi, \tag{2.2}$$

$$\frac{\partial e}{\partial t} + \nabla \cdot (e\vec{v}) = -p\,(\nabla \cdot \vec{v})\,, \tag{2.3}$$

$$\frac{\partial \vec{B}}{\partial t} = \nabla \times \left(\vec{v} \times \vec{B} - \eta \nabla \times \vec{B} \right), \tag{2.4}$$

$$\nabla \cdot \vec{B} = 0 \tag{2.5}$$

where $\vec{v}$ is the large-scale velocity of gas, ρ is the gas density distribution, p is the gas pressure, p_{cr} is the cosmic ray pressure, Φ is the gravitational potential, $\vec{B}$ is the magnetic induction, e is the energy and η is the turbulent magnetic diffusivity. As I described in Section 1.3.1 cosmic rays are weightless, thus they only contribute to the total pressure (not to the total mass) and are included in the gas motion equation as ∇p_{cr} (Berezinski et al. 1990). In all presented simulations I use an isothermal equation of state

$$p = \rho c_s^2, \tag{2.6}$$

where c_s is the constant, isothermal sound speed.

2.1.2 Transport of the cosmic ray component

To make the set of MHD Eqn. (2.1:2.5) complete the part responsible for the cosmic ray transport was added to them. Following Schlickeiser & Lerche (1985) the propagation of the cosmic ray component in the ISM is described by the diffusion-advection equation

$$\frac{\partial e_{cr}}{\partial t} + \nabla(e_{cr}\vec{v}) = \nabla(\hat{K} \nabla e_{cr}) - p_{cr}(\nabla \cdot \vec{v}) + CR_{source}, \tag{2.7}$$

where e_{cr} is the cosmic ray density, $p_{cr} = (\gamma_{cr} - 1)e_{cr}$ is the cosmic ray pressure, $\hat{K}$ is the diffusion tensor, $\vec{v}$ is the gas velocity and CR_{source} is the source term for cosmic ray energy. I assume that the cosmic ray energy is added to the system by SNe explosions (see Subsection 2.1.4). The adiabatic index γ_{cr} for the cosmic ray fluid is set to be 14/9.

Following Ryu et al. (2003) the anisotropic diffusion of the cosmic ray gas is described by diffusion tensor $\hat{K}$ as

$$K_{ij} = K_{\perp}\delta_{ij} + (K_{\parallel} - K_{\perp})n_i n_j, \tag{2.8}$$

where $K_\perp$ and $K_\parallel$ are perpendicular and parallel (with respect to the local magnetic field direction) cosmic ray diffusion coefficients and $n_i = B_i/B$ are components of the unit vectors tangent to magnetic field lines.

I added the cosmic ray diffusion algorithm to the Godunov code using the implementation method proposed by Hanasz & Lesch (2003) (see Appendix B.0.1).

2.1.3 Gravitational potentials

Parameter Φ in Eqn. 2.2 represents the total gravitational potential of the modelled galaxy. It can be divided into two parts: an axisymmetric and nonaxisymmetric one. The axisymmetric component consists of the rotating disk of stars, the large and massive halo and the central bulge. In all models the halo potential Φ_h has the same form as the bulge potential Φ_b and is described by a Plummer sphere

$$\Phi_{b,h} = -\frac{GM_{b,h}}{\sqrt{x^2 + y^2 + z^2 + a_{b,h}^2}}, \tag{2.9}$$

where b, h stands for the bulge and the halo (respectively), M is the mass of each component, x, y, z are Cartesian coordinates and $a_{b,h}$ corresponds to the length scale of the bulge and the halo. Depending on the model the stellar disk potential Φ_d is represented by the isochrone potential of the form

$$\Phi_d = -\frac{GM_d}{a_d + \sqrt{a_d^2 + x^2 + y^2}}, \tag{2.10}$$

or by the Miyamoto-Nagai potential (Miyamoto & Nagai 1975) of the form

$$\Phi_d = -\frac{GM_d}{\sqrt{x^2 + y^2 + (a_d + \sqrt{z^2 + b_d^2})^2}}, \tag{2.11}$$

where M_d is the disk total mass, a_d is the disk scalelength, b_d is the disk scaleheight.

The nonaxisymmetric component of the gravitational potential, i.e. the bar or the oval is modelled using a second-order ($n = 2$) Ferrers (1877) ellipsoid whose density $\rho(x)$ distribution is

$$\rho(x) = \begin{cases} \rho_c(1 - m^2)^2 & , \quad m < 1 \\ 0 & , \quad m \geq 1 \end{cases}, \tag{2.12}$$

where, $\rho_c = \frac{105}{32\pi}\frac{GM_b}{abc}$ is the central density, M_b is the bar (oval) total mass and

$$m^2 = \frac{x^2}{a^2} + \frac{y^2}{b^2} + \frac{z^2}{c^2}, \tag{2.13}$$

with $a > b \geq c$ as the respective semi-axes.

The corresponding potential is expressed by the integral

$$\Phi_b = -\pi G abc \frac{\rho_c}{n+1} \int_\lambda^\infty \frac{du}{\Delta(u)} (1 - m^2(u))^{n+1}, \tag{2.14}$$

where

$$m^2(u) = \frac{x^2}{a^2 + u} + \frac{y^2}{b^2 + u} + \frac{z^2}{c^2 + u}, \tag{2.15}$$

$$\Delta^2(u) = (a^2 + u)(b^2 + u)(c^2 + u), \tag{2.16}$$

$n = 2$ (second order Ferrers ellipsoid) and λ is the unique positive solution of

$$m^2(\lambda) = 1, \tag{2.17}$$

outside of the bar ($m \geq 1$) and $\lambda = 0$ inside the bar. If we put $a > b > c$ in Eqn. 2.12:2.16 we obtain an ellipsoid, however for $a > b = c$ we get a prolate spheroid.

2.1.4 SNe explosions

To determine the SNe probability distribution and its rate I use the Schmid (1959) law in the form of

$$\Sigma_{SFR} \propto \Sigma_{gas}^n \tag{2.18}$$

where Σ_{SFR} is the surface density of the star formation, Σ_{gas} is the surface density of gas and $n = 1 \div 1.4$ (Kennicutt 1998). Consequently, from Eqn. 2.18 I obtain that the probability of a single SN event is proportional to the local gas density.

Each SN explosion is a localized source of cosmic rays with uniform distribution in xy coordinates and Gaussian distribution in z coordinate. In all models I assume that 10% of 10^{51} erg SN kinetic energy output is converted into the cosmic ray energy, while the thermal energy from SNe explosions is neglected. In some models also weak and randomly oriented magnetic vector potential is injected during SNe explosions. Following Jackson (1999) and Kowalik & Hanasz (2007) the magnetic vector potential A of a dipolar magnetic field produced by a single SN explosion can be expressed as

$$A(r, \phi, \theta) = A_0 \frac{r \sin\theta}{(r_{SN}^2 + r^2 + 2 r r_{SN} \sin\theta)^{3/2}} e_\phi, \tag{2.19}$$

where r_{SN} is the size of the SN remnant, r, θ and ϕ are spherical coordinates and A_0 is the amplitude. Parameter r_{SN} also denotes the half-width of the Gaussian profile describing the distribution of the injected cosmic ray energy.

To obtain a model that is fully repeatable, a random distribution of SNe explosions is initialized using the same 'seed'[1]. Then the pseudo-random generator produces the same succession of random numbers used in the SNe explosions algorithm.

[1]Seed is the argument which initializes the pseudo-random number generator.

2.1.5 Polarization maps

Using the synthetic radio polarization maps, the obtained results can be compared directly with the observed properties of galaxies. To obtain the intensity and the polarization angle of B-vectors I integrated Stokes parameters along the line of sight and next I smoothed them with a Gaussian beam (see Appendix B.0.1). In all models I used the same position angle $\theta = 90°$ and two different inclinations: $i = 0°$ (face-on) and $i = 90°$ (edge-on). I assumed that the intrinsic polarization degree of synchrotron emission is 70% and energy spectral index of relativistic electrons $\gamma = 2.8$. All quantities (the magnetic field, the cosmic ray energy and the density of gas) needed for calculations of polarization maps were obtained during numerical simulations.

2.2 Initial conditions

In all models time is measured in Gyr, while mass, length, velocity and magnetic field are expressed in $M_\odot$, kpc, $\mathrm{km\,s^{-1}}$ and μG, respectively. The speed of sound is set to $c_s = 5.12\,\mathrm{km\,s^{-1}}$ and the initial gas density at the galactic midplane ρ_0 is equal to $1.0 n_H\,\mathrm{cm^{-3}}$, where n_H is a hydrogen atom. Following several detailed reviews of the theory of cosmic ray diffusion (e.g. Strong et al. 2007), the values of the cosmic ray diffusion coefficients assumed in all simulations are: $K_\parallel = 3 \times 10^{28}\,\mathrm{cm^2 s^{-1}} = 100\,\mathrm{kpc^2\,Gyr^{-1}}$ and $K_\perp = 3 \times 10^{26}\,\mathrm{cm^2 s^{-1}} = 1\,\mathrm{kpc^2\,Gyr^{-1}}$, while the resistivity coefficient η is set to be $3 \cdot 10^{24}\,\mathrm{cm^2 s^{-1}} = 0.1\,\mathrm{kpc^2\,Gyr^{-1}}$. According to the assumption that the cosmic ray pressure is equal to the gas pressure

$$\beta = \frac{p_{cr}}{p_{gas}} \tag{2.20}$$

I assume that β is constant and equal to 1. Additionally, along all directions I apply outflow boundary conditions. To obtain the most realistic results in all of the simulations I assume that no initial magnetic field is present ($\alpha = p_{mag}/p_{gas} = 0$) but the weak and randomly oriented magnetic field is introduced to the disk in 10% of SNe explosions (see Section 2.1.4). At the beginning of the calculation of all models the magnetic field is not present. It is added later to the galactic disk through randomly oriented SNe explosions in the period of time 0.1 Gyr – 1.1 Gyr. During this period weak $10^{-5}\,\mu$G and dipolar magnetic field is supplied in 10 % of SNe remnants. After $t = 1.1$ Gyr dipolar magnetic field is no longer injected because, due to the dynamo action, its contribution starts to be insignificant.

Parameters described above are the same in the model of a barred and a ringed galaxy. However, there are many other parameters which vary in those models. All of those parameters are listed in below descriptions of the barred and ringed galaxy models.

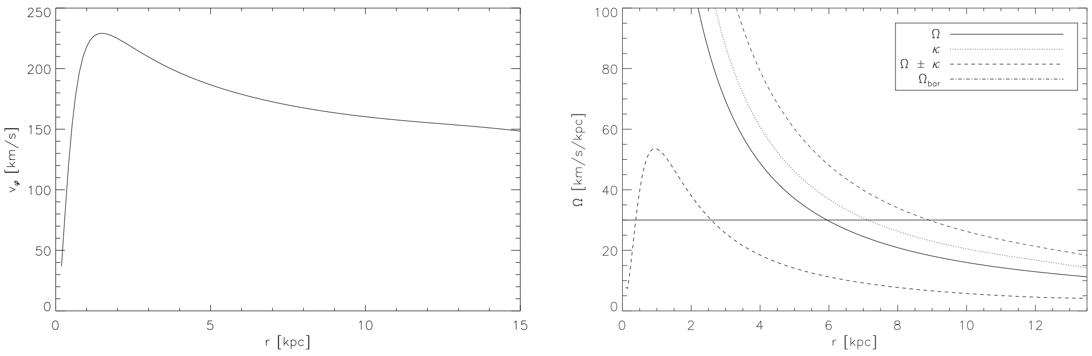

Figure 2.1: The rotation curve (left panel) and the angular frequency (right panel) for the modelled barred galaxy. The solid horizontal line $\Omega_{bar} = 30\,\mathrm{km\,s^{-1}kpc^{-1}}$ determines the resonances which positions is given in Table 2.1.

2.2.1 Numerical model of a barred galaxy

I numerically investigated the cosmic ray driven dynamo model in barred galaxies in a computational domain which covers 30 kpc × 30 kpc × 7.5 kpc of space with 300 × 300 × 75 cells of a 3D Cartesian grid, which gives 100 pc of spatial resolution in each direction. As I mentioned above, our model of a barred galaxy consists of four components: a large and massive halo, a central bulge, a rotating disk of stars and a bar. They are represented by different analytical gravitational potentials (see Section 2.1.3): the halo and the bulge components are described by two Plummer spheres, the stellar disk is represented by the isochrone gravitational potential, the bar is defined by the prolate spheroid. The bar component is introduced into the galaxy gradually in time, until it reaches its final mass M_{bar} (from t = 0.1 Gyr to t = 0.4 Gyr). In order to conserve the total mass of the galaxy I reduce the mass of the bulge, having $M_{bar}(t) + M_b(t) = const$ during the calculations. The bar rotates with a constant angular speed $\Omega_{bar} = 30\,\mathrm{km\,s^{-1}kpc^{-1}}$, which determines the values of $R_{ILR} = 4\,\mathrm{kpc}$, $R_{CR} = 5\,\mathrm{kpc}$ and $R_{OLR} = 6\,\mathrm{kpc}$. In Figure 2.1 the rotation curve of gas (left panel) generated by gravitational potentials as well as the position of Lindblad resonances (right panel) are present. The obtained rotation curve has a velocity peak ($228\,\mathrm{km\,s^{-1}}$) at radii 1.0 – 1.5 kpc and stays approximately flat up to large distances. This shape of the rotation curve is similar to the one usually observed in barred and non-barred spiral galaxies (Sofue et al. 1999). All quantities which characterize the model of the barred galaxy are summarized in Table 2.1.

In the beginning the modelled galactic disk is in hydrostatic equilibrium (Figure 2.2, left panel). The density and velocity field resulting from the total gravitational potential are shown in Figure 2.2. The galactic disk extends up to R_{BG} where the gas density distribution is being cut down. I made five different simulations of the barred galaxy. In each of them I analyze the evolution of the barred galaxy for a different SN frequency f_{SN}. Following Ferrière (1998) the observed SN frequency for the Galaxy is $1/445\,\mathrm{yr^{-1}}$

parameter	name	value	units
M_d	disk mass	$4.0 \cdot 10^{10}$	$M_{\odot}$
a_d	length scale of the disk	0.6	kpc
M_b	bulge mass	$1.5 \cdot 10^{10}$	$M_{\odot}$
a_b	length scale of the bulge	5.0	kpc
M_h	halo mass	$1.2 \cdot 10^{11}$	$M_{\odot}$
a_h	length scale of the halo	15.0	kpc
M_{bar}	bar mass	$1.5 \cdot 10^{10}$	$M_{\odot}$
a_{bar}	length scale of bar major axis	6.0	kpc
b_{bar}	length scale of bar minor axis	3.0	kpc
c_{bar}	length scale of bar vertical axis	2.5	kpc
Ω_{bar}	bar angular velocity	30.0	$\mathrm{km\,s^{-1}kpc^{-1}}$
CR	corotation radius	6.0	kpc
IILR	Inner Inner Lindblad Resonance	0.4	kpc
OILR	Outer Inner Lindblad Resonance	3.0	kpc
OLR	Outer Lindblad Resonance	8.5	kpc
R_{BG}	galaxy radius	13.5	kpc

Table 2.1: Adopted parameters for the barred galaxy model.

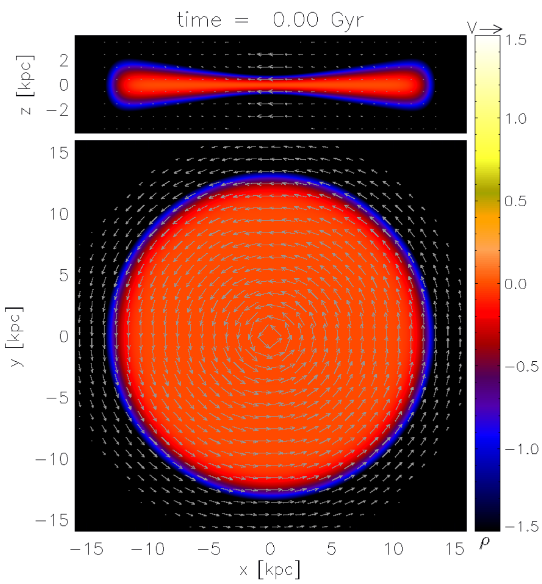

Figure 2.2: The initial distribution of the density with overploted vectors of the velocity field for the modelled barred galaxy.

Model	f_{SN}[yr^{-1}]
BS1	1/25
BS2	1/50
BS3	1/100
BS4 (RM)	1/200
BS5	1/500

Table 2.2: Parameters of the barred galaxy simulations presented in this thesis. Subsequent columns show: simulation name and the SN frequency f_{SN}.

for Type I and $1/52\,\mathrm{yr}^{-1}$ for Type II SNe. Taking into account both types of SNe, one explosion is expected every 47 years. In my simulations I use the following values of the SN frequency: $f_{SN} = 1/25\,\mathrm{yr}^{-1}$ for model BS1 $f_{SN} = 1/50\,\mathrm{yr}^{-1}$ for model BS2, $f_{SN} = 1/100\,\mathrm{yr}^{-1}$ for model BS3, $f_{SN} = 1/200\,\mathrm{yr}^{-1}$ for model BS4 and $f_{SN} = 1/500\,\mathrm{yr}^{-1}$ for model BS5. The time frequency of SN explosion f_{SN} equal to 25 means that one SN explodes per 25 years. Because the modelled barred galaxy has slightly smaller size than the Milky Way, three of the values above of the SN frequency are smaller than those observed in our Galaxy. In Table 2.2 all models of the barred galaxy presented in this thesis are listed.

2.2.2 Numerical model of the ringed galaxy NGC 4736

NGC 4736 (M94) is a bright, nearby ringed galaxy classified as (R)SAB(rs)ab type by Buta et al. (2007). Although, this galaxy is a member of a large group of galaxies *Canis Venatici I* (Geller & Huchra 1983) it does not possess any sizable nearby companions. NGC 4736 also shows no signs of recent mergers or close interactions, which means that all observed morphological structures are triggered by an intrinsic mechanism occurring in the galaxy. Optical, ultraviolet and infrared photographs (Trujillo et al. 2009) show that this galaxy consists of certain features, e.g. an inner and an outer ring and an extensive spiral structure. The object has been made the subject of numerous studies and several good reviews about its morphology can be found in the literature (e.g. Mulder & van Driel 1993; Möllenhoff et al. 1995). Using optical and HI observations Bosma et al. (1977) identified five morphological regions in this system:

1. A bright central region within a radius of $R_{GR} < 480\,\mathrm{pc}$ (15" at a distance of 6.3 Mpc as used by Gerin et al. (1991)) where the evidence of recent star formation activity has been found (see Beckman et al. 1991). The isophotal twisting in this region could be the consequence of sub-structures, such as a triaxial bulge (Beckman et al. 1991) or a long central bar (Kormendy 1993; Möllenhoff et al. 1995).

2. The zone of an inner spiral structure, 480 pc < R_{GR} < 1.6 kpc (15" to 50") bounded by the inner ring where the majority of HII regions and young blue objects (characteristic for strong star formation) are located. Several interpretations have been proposed to explain the origin of the inner ring. van der Kruit (1976) suggested that ring-like structures in NGC 4736 are the manifestation of nuclear activity. On the other hand, using Fabry-Perot data, Buta (1988) concluded that the inner ring is related to the ILR produced by some nonaxisymmetric gravitational potential.

3. An outer spiral structure with a multiple arm pattern 1.6 kpc < R_{GR} < 6.4 kpc (50" to 200"). This region probably forms a massive oval disk with an axis ratio of 0.8. The nonaxisymmetric gravitational potential produced by the oval disk could be responsible for the existence of the inner and the outer ring. In fact, simulations made by Gerin et al. (1991); Gu et al. (1996) show that stable and long-lived rings located at the ILR and the OLR are created due to this potential.

4. A gap of lower surface brightness.

5. A faint outer ring at $R_{GR} \sim$ 10.6 kpc (330"), which (as was mentioned above) is created due to the nonaxisymmetric gravitational potential of the oval disk. However, recent investigation of non-optical data made by Trujillo et al. (2009) strongly support the idea that the outer part of the galaxy is formed by an extensive structure of spiral arms rather than by a closed stellar ring. Trujillo et al. (2009) presented also the numerical model in which the oval distrotion is responsible for the development of spiral arms and for the inner ring formation.

Following observations of NGC 4736, the modelled ringed galaxy consists of five components: the large and massive halo, the central bulge, the outer disk, the oval distortion and the small bar. As in the case of the barred galaxy, the halo and the bulge are described by Plummer spheres, however the disk is modelled using the Miyamoto & Nagai potential (Eqn. 2.11). Parameters in gravitational potentials (masses and length scales) have essentially been chosen by fitting the observed rotation curve with the model potentials described above. In Figure 2.3 (left panel) the obtained rotation curve for the adopted values of the parameters (see Table 2.3) is shown. Similar values of masses and length scales were retrieved from the fit to the stellar mass surface density by Trujillo et al. (2009).

The nonaxisymmetric perturbing gravitational potential from the oval distortion can be described by a very mild ellipsoid bar. In this case the bar major a_{oval}, minor b_{oval} and vertical c_{oval} axes are equal to 4.8 kpc, 4.1 kpc and 0.5 kpc, respectively. The obtained axis ratio is equal to 0.85 and is consistent with observations made by Bosma et al. (1977). The additional weak bar component is represent by prolate spheroid with a_{bar} = 0.6 kpc and $b_{bar} = c_{bar}$ = 0.4 kpc. Taking into account the above nonaxisymmetric gravitational potentials, we obtain a so-called double-barred galaxy, where the smaller bar is nested

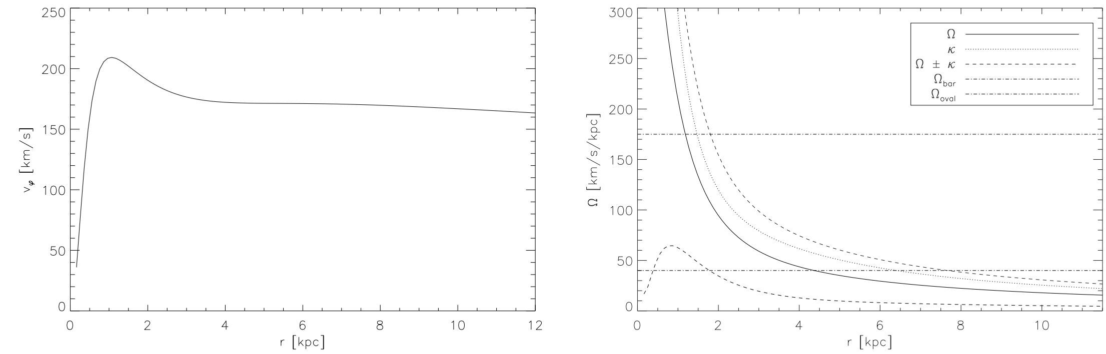

Figure 2.3: The rotation curve (left panel) and the angular frequency (right panel) for the modelled ringed galaxy. Solid horizontal lines $\Omega_{bar} = 40\,\mathrm{km\,s^{-1}kpc^{-1}}$ and $\Omega_{oval} = 175\,\mathrm{km\,s^{-1}kpc^{-1}}$ determine the resonances which positions are given in Table 2.3.

inside the larger bar (here the oval). Many authors (e.g. Shlosman et al. 1989) have studied the dynamically possible pattern speeds of double bars and have concluded that the “inner“ small bar should rotate much faster than the “outer“ large bar.

The most important issue in the presented model of the ringed galaxy is the determination of the bar and the oval pattern speeds which can explain a number of features in NGC 4736. Several pattern speeds for the bar and oval distortions have been proposed in the literature. In the case of the oval disk the suggested value of the pattern speed Ω_{oval} ranges from $35\,\mathrm{km\,s^{-1}kpc^{-1}}$ (Waller et al. 2001) to $56\,\mathrm{km\,s^{-1}kpc^{-1}}$ (Mulder & Combes 1996). The pattern speed Ω_{oval} adopted in my simulations is equal to $40\,\mathrm{km\,s^{-1}kpc^{-1}}$ and agrees nicely with previous studies made by Trujillo et al. (2009), where $\Omega_{oval} = 38\,\mathrm{km\,s^{-1}kpc^{-1}}$. Using this pattern speed, the following positions of Lindblad resonances and CR are obtained: $R_{IILR} = 0.4$ kpc, $R_{OILR} = 1.8$ kpc, $R_{OLR} = 7.7$ kpc and $R_{CR} = 4.4$ kpc. Comparing these numbers with observations of NGC 4736 made by Bosma et al. (1977) I get quite good agreement. Additionally, using the given sequence of resonances I obtain the following ratios: $R_{CR}/R_{oval} = 0.92$ and $R_{OLR}/R_{CR} = 1.75$. These ratios match well the theoretical values proposed by Buta & Combes (1996), where $R_{CR}/R_{oval} = 1.04$ and $R_{OLR}/R_{CR} = 1.70$.

The inner bar rotates much faster than the outer oval disk and, what is more, the OLR of the inner bar should coincide with the OILR of the oval disk. To meet these two constraints, the pattern speed of the inner bar in my model is set to be $\Omega_{bar} = 175\,\mathrm{km\,s^{-1}kpc^{-1}}$. Because, I do not use the same numerical model of NGC 4736 as the one used by previous authors, the bar angular velocity is lower than that applied by Möllenhoff et al. (1995), where $\Omega_{bar} = 290\,\mathrm{km\,s^{-1}kpc^{-1}}$. In the resonance-diagram (Figure 2.3, right panel) locations of Lindblad resonances produced by the inner bar and the oval disk are marked.

Both nonaxisymmetric gravitational potentials are introduced into the galaxy slowly in time (from $t = 0.1$ Gyr to $t = 0.4$ Gyr), until they reach their final masses M_{bar} and M_{oval}.

parameter	name	value	units
M_d	disk mass	$3.5 \cdot 10^{10}$	$M_\odot$
a_d	length scale of the disk	5.5	kpc
b_d	height scale of the disk	0.5	kpc
M_b	bulge mass	$1.7 \cdot 10^{10}$	$M_\odot$
a_b	length scale of the bulge	0.5	kpc
M_h	halo mass	$2.0 \cdot 10^{11}$	$M_\odot$
a_h	length scale of the halo	25.0	kpc
M_{bar}	bar mass	$7.5 \cdot 10^{9}$	$M_\odot$
a_{bar}	length scale of bar major axis	0.6	kpc
b_{bar}	length scale of bar minor axis	0.4	kpc
c_{bar}	length scale of bar vertical axis	0.4	kpc
Ω_{bar}	bar angular velocity	175.0	$\mathrm{km\,s^{-1}kpc^{-1}}$
CR	corotation radius	1.2	kpc
ILR	Inner Lindblad Resonance	–	kpc
OLR	Outer Lindblad Resonance	1.8	kpc
M_{oval}	oval mass	$3.5 \cdot 10^{10}$	$M_\odot$
a_{oval}	length scale of oval major axis	4.8	kpc
b_{oval}	length scale of oval minor axis	4.1	kpc
c_{oval}	length scale of oval vertical axis	0.5	kpc
Ω_{oval}	oval angular velocity	40.0	$\mathrm{km\,s^{-1}kpc^{-1}}$
CR	corotation radius	4.4	kpc
IILR	Inner Lindblad Resonance	0.4	kpc
OILR	Inner Lindblad Resonance	1.8	kpc
OLR	Outer Lindblad Resonance	7.7	kpc
R_{RG}	galaxy radius	11.5	kpc

Table 2.3: Adopted parameters for the ringed galaxy NGC 4736 model.

In order to conserve the total mass of the galaxy I reduce the bulge mass and the disk mass, having $M_{bar}(t) + M_b(t) = const$ and $M_{oval}(t) + M_d(t) = const$ during the calculations. All quantities which characterize the model of the ringed galaxy are summarized in Table 2.3. Computational domain covers 26 kpc $\times$ 26 kpc $\times$ 6.4 kpc of space with 256 $\times$ 256 $\times$ 64 cells of 3D Cartesian grid, which gives 100 pc of spatial resolution in each direction. Initially, the modelled ringed galaxy is in hydrostatic equilibrium (Figure 2.4, left panel). The density and velocity field resulting from the total gravitational potential are shown in Figure 2.4. The galactic disk extends up to R_{RG} where the gas density distribution is being cut down. As in the case of the barred galaxy, I tested the evolution of the ringed galaxy for five different SN frequencies. In my simulations I use the following values of the SN frequency: $f_{SN} = 1/50\,\mathrm{yr}^{-1}$ for model RS1 $f_{SN} = 1/100\,\mathrm{yr}^{-1}$ for model RS2, $f_{SN} = 1/200\,\mathrm{yr}^{-1}$ for model RS3, $f_{SN} = 1/300\,\mathrm{yr}^{-1}$ for model RS4 and $f_{SN} = 1/500\,\mathrm{yr}^{-1}$ for model RS5. The time frequency of SN explosion f_{SN} equal to 50 means that one SN

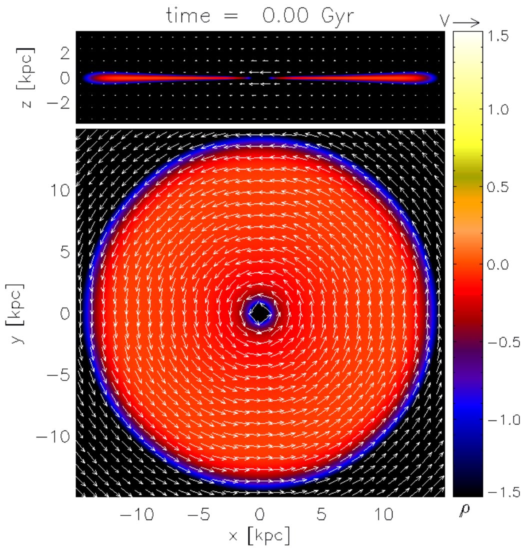

Figure 2.4: The initial distribution of the density with overploted vectors of the velocity field for the modelled ringed galaxy.

Model	$f_{SN}[\,\mathrm{yr}^{-1}]$
RS1	1/50
RS2	1/100
RS3	1/200
RS4	1/300
RS5	1/500

Table 2.4: Parameters of ringed galaxy simulations presented in this thesis. Subsequent columns show: simulation name and the SN frequency f_{SN}.

explodes per 50 years. In Table 2.4 all models of the ringed galaxy presented in this thesis are listed.

Chapter 3

Results

3.1 Simulations of the barred galaxy

In the following section the outcome of simulations of the barred galaxy evolution is discussed. An overview of the various models can be found in Table 2.2, where five models with different SN frequency are listed. For all of these models the distribution of the gas density and cosmic ray energy density, polarization maps, pitch angles, the distribution of the toroidal magnetic field component and the growth rate of the magnetic field energy are studied. All simulations are stopped when the magnetic field reaches the equipartition, thus, depending on the model, between $t = 4\,\mathrm{Gyr}$ and $t = 6\,\mathrm{Gyr}$. By testing many different models the range of SN frequency f_{SN} for which the magnetic field amplification in barred galaxies is most efficient can be determined.

3.1.1 General evolution for the reference model RM (BS4)

To show basic dynamical and magnetic features of the simulated barred galaxy I present below the complete description of the time evolution of the reference model RM (BS4, $f_{SN} = 1/200\,\mathrm{yr}^{-1}$). I chose this model as the main model because, in my opinion, it is the best example from the available sample of the barred galaxy models (see Table 2.2). During the first stage of all simulations, ahead I start to activate SNe explosions or nonaxisymmetrical gravitational potentials, the system evolves to reach a dynamical equilibrium between gas and cosmic rays. After that time ($t = 0.1\,\mathrm{Gyr}$) the influence of the cosmic ray driven dynamo action on the evolution of the barred galaxy model can be studied in detail.

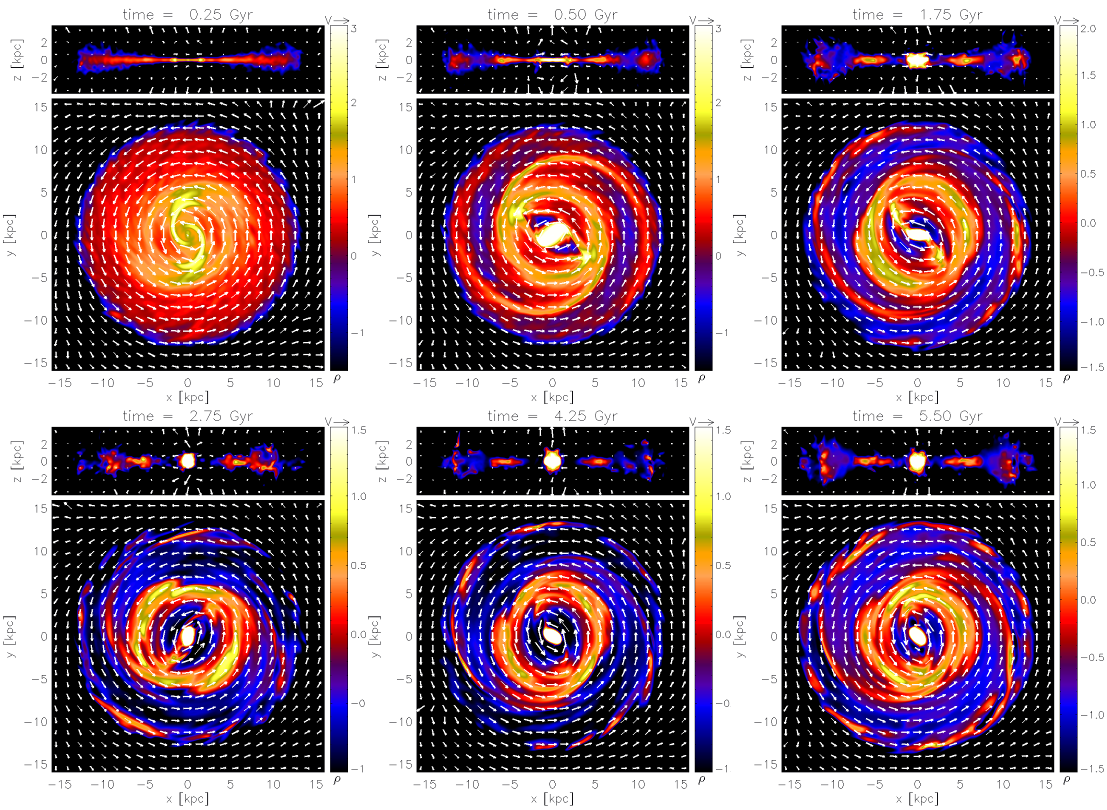

Figure 3.1: The logarithm of the gas density and the gas velocity field (vectors) in vertical and horizontal slices through the disk center for selected time steps for the reference model RM (BS4). The gas density is expressed in units of hydrogen atom per cubic centimeter ($1.0 n_H\,\mathrm{cm}^{-3}$).

3.1.1.1 Gas density and velocity field

To present and shortly describe basic dynamical features of the reference model RM, I show the logarithm of the gas density distribution and velocity field for selected time steps of galactic evolution (see Figure 3.1). In the galactic midplane the well defined structures, i.e., spiral arms, dust lanes and the central bulge, are visible and change their appearance during the whole simulation time. As it was mentioned in the previous section (Section 2.2.1), the bar is introduced into the galaxy gradually in time from 0.1 Gyr to 0.4 Gyr (it takes about 1.2 rotation of the bar). During this time two arc-like structures appear in the central part of the galaxy (see the time step t = 0.25 Gyr, Figure 3.1). From time step t = 0.4 Gyr the mass of the bar does not change. Additionally, the nonaxisymmetric gravitational potential produced by the bar has a strong influence on the gas distribution in the disk. Namely, two arcs formed earlier evolve into two streams of gas along the leading edges of the bar. These gas density structures can be identified with the dust lanes (very well defined at time steps t = 0.5 Gyr and t = 1.75 Gyr, Figure 3.1), with strong density enhancements at their outer ends and in the galactic center. Density enhancements are also observed in the outer galactic disk, where spiral arms are generated. Initially, at time $t = 0.5$ Gyr (Figure 3.1) gaseous spiral arms are thick and slightly disturbed by the SN activity. At later time steps outer spiral arms are still well defined, however due to SNe explosions their structures are not plain and many discontinuities can be observed (e.g., time steps $t = 2.75$ Gyr or $t = 4.25$ Gyr, Figure 3.1).

The presence of the bar strongly disturbs the gas velocity field. Rapid changes of the velocity direction can be seen in the innermost region of the bar (e.g., time steps 1.75 Gyr or 2.75 Gyr, Figure 3.1). Gas flows out of the centre just before it passes through the shock, and then it turns back into the centre along the leading edge of the bar. Additionally, as the simulation proceeds gas streams inside the bar are less visible, while shocks in these regions are still strong, which is confirmed by velocity vectors pattern (see time steps 1.75 Gyr or 2.75 Gyr, Figure 3.1). During a few rotations of the bar almost the whole gas from the central part of the galaxy transfers to its outer regions and to its nucleus. In vertical slices the configuration of velocity field vectors indicates that the gas component outflows above and below the central part of the disk. Indeed, the gas component is initially located mainly in the disk plane (see the time step $t = 0.5$ Gyr, Figure 3.1), but at later time steps (e.g., time steps 2.75 Gyr or 5.5 Gyr, Figure 3.1) is subsequently transferred by SNe explosions from the galactic disk to the galactic halo. The vertical wind produced by SNe remnants triggers the mass outflow, whose averaged rate is equal to $1.1 M_\odot$ per year.

3.1.1.2 Distribution of the cosmic ray energy density

The logarithm of the cosmic ray energy density distribution for the evolution of the reference model RM is shown in Figure 3.2. Presented time steps are the same as those for the gas density distribution (see Figure 3.1). The enhancement of the cosmic ray energy and the gas density are visible in the same regions (compare Figure 3.1 and Figure 3.2). Again, all main features of the barred galaxy are present during the whole simulation time, however, well defined spiral arms at time steps $t = 0.5$ Gyr, $t = 1.75$ Gyr and $t = 2.75$ Gyr in Figure 3.2 are less visible at later time steps. As the simulation proceeds most of the cosmic ray gas is transported to the central part of the galaxy (compare e.g., time steps 0.25 Gyr and 5.5 Gyr, Figure 3.2). Additionally, some amount of the cosmic ray gas is also transferred to the outer part of the galaxy. In contrast to the gas distribution, the cosmic ray gas is present both in the galactic disk and galactic halo from the very beginning of the simulation, which can be noticed in all vertical planes in Figure 3.1. At each time step in Figure 3.2 traces of the SN activity can be observed. They are indicated by the growth of the cosmic ray energy density and visible as small spots. Star formation rate enhancements correspond to high gas density regions. It is clearly visible at the time step $t = 0.5$ Gyr in Figure 3.2 and harder to see at later time steps, when the contrast between injected and already present cosmic ray gas is smaller than the initial one.

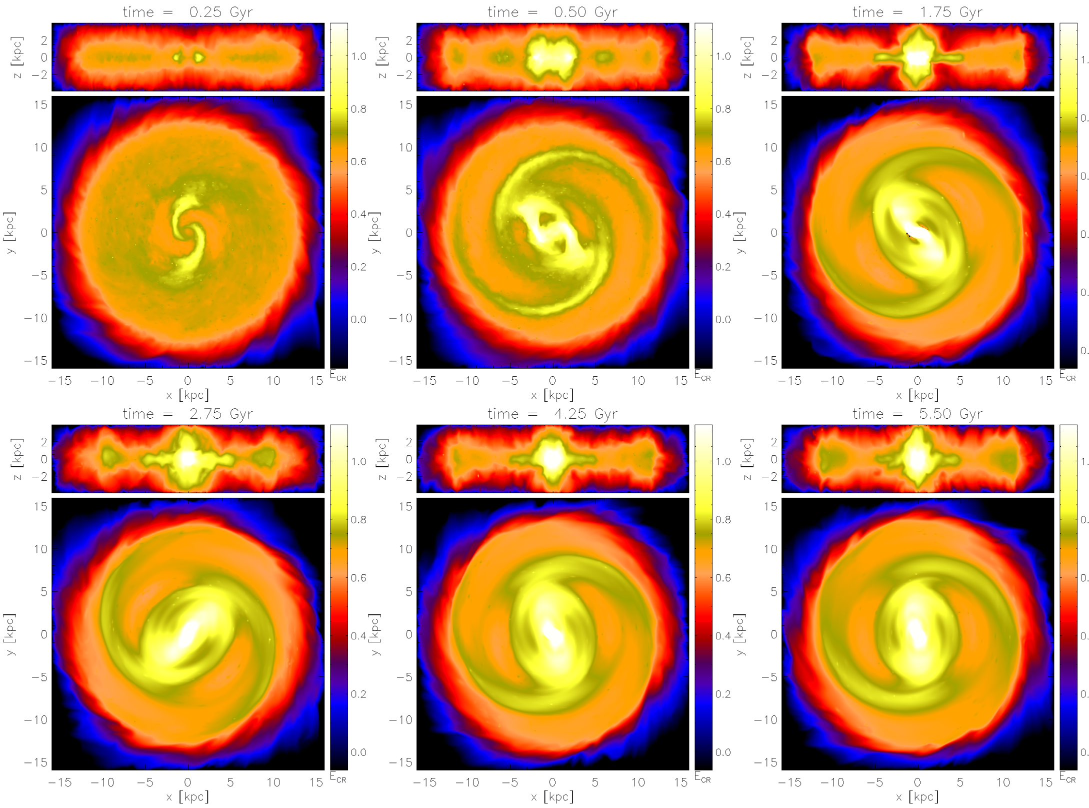

Figure 3.2: The logarithm of the cosmic ray energy density distribution in vertical and horizontal slices through the disk center for selected time steps for the reference model RM (BS4). The cosmic ray energy density is expressed in units of electron volt per cubic centimeter $\mathrm{eVcm^{-3}}$.

3.1.1.3 Amplification and structure of the magnetic field

At the beginning of the calculation of the reference model RM the magnetic field is not present. As mentioned in Section 2.2, it is added later to the galactic disk through randomly oriented SNe explosions in the period of time 0.1 Gyr – 1.1 Gyr. After $t = 1.1$ Gyr the dipolar magnetic field is no longer injected because, due to the dynamo action, its contribution starts to be insignificant. In Figure 3.3 the toroidal magnetic field component in horizontal and vertical slices is plotted. Red colour represents regions with the positive toroidal magnetic field, blue with negative one, while unmagnetized regions of the volume are white. At time steps $t = 0.5$ Gyr and $t = 1.0$ Gyr the toroidal magnetic field is mostly random, as it originates from randomly oriented magnetic dipoles. The ordered magnetic field is visible in the inner part of the galaxy, where it follows the gas distribution, namely the bar and dust lanes. In this area the magnetic field also reaches the highest values during the whole simulation time. At later time step $t = 2.0$ Gyr (Figure 3.3) the toroidal magnetic field component forms well defined magnetic arms which can be observed till the end of the simulation. The total magnetic field in magnetic arms is approximately ten times weaker than the magnetic field in the bar region (compare Table 3.1 and Table 3.2).

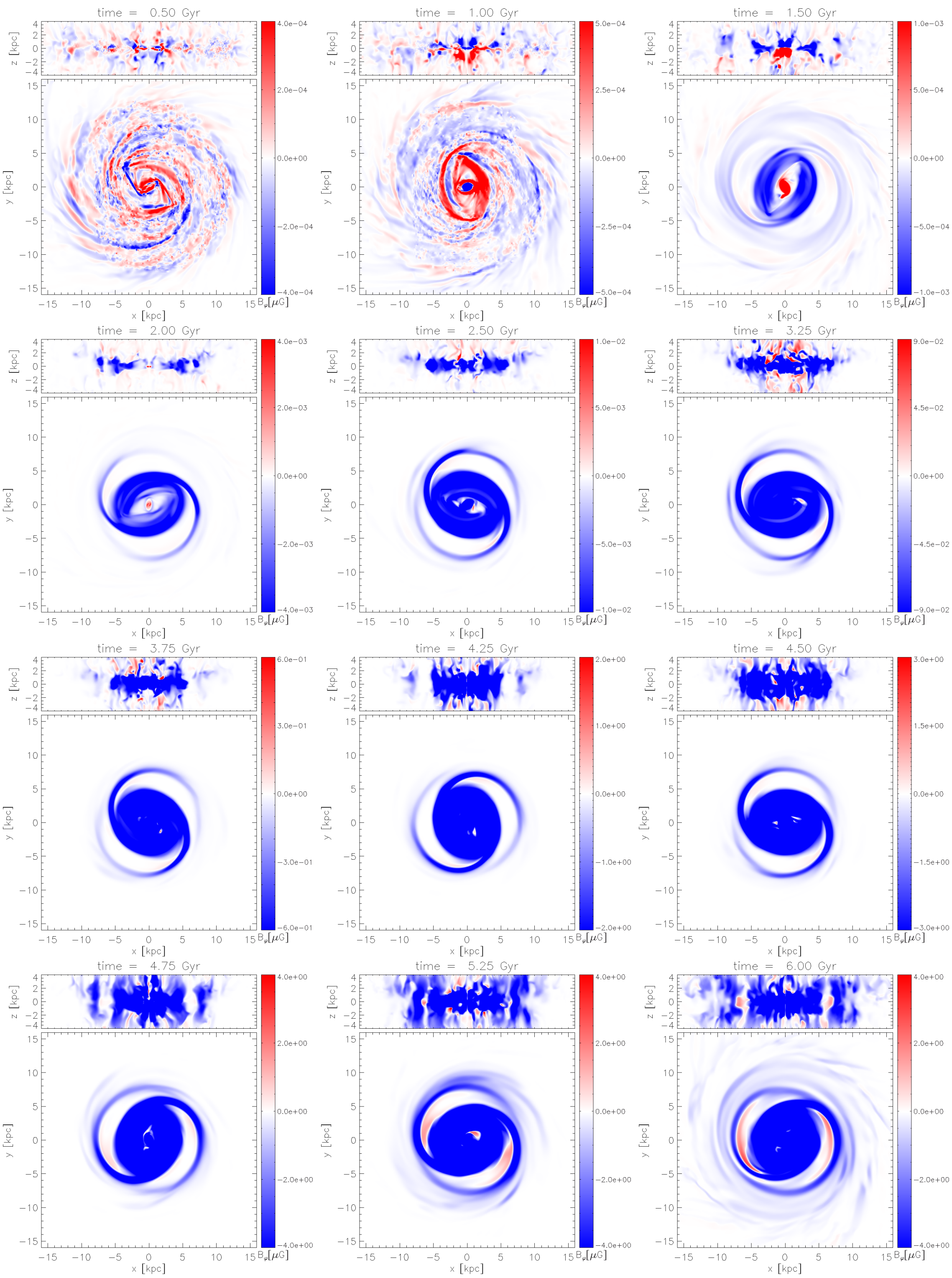

Figure 3.3: The distribution of the toroidal magnetic field in vertical and horizontal slices through the disk center for selected times steps for the reference model RM (BS4). Red colour represents regions with the positive toroidal magnetic field, blue with negative, while unmagnetized regions of the volume are white. To enhance weaker structures of the magnetic field in the outer galactic disk (e.g. magnetic arms) the colour scale in magnetic field maps is saturated. The maximum magnetic field strengths in galactic bar and in magnetic arms for selected times steps are given in Table 3.1 and Table 3.2, respectively.

Gas motions in the bar region generate shocks which together with the dynamo action cause that the magnetic field is strongest in this area.

Due to the nonaxisymmetric gravitational potential of the bar and the cosmic ray driven dynamo, the positive toroidal magnetic field component gradually reaches higher values, both in the bar and magnetic arms. Additionally, in the galactic disk and halo the volume occupied by the positive toroidal magnetic field component expands continuously till the end of the simulation. Reversals of the magnetic field can be observed at a few time steps. For instance, at time steps $t = 1.5$ Gyr (Figure 3.3) and $t = 2.0$ Gyr (Figure 3.3) in the very inner part of the bar the negative toroidal magnetic field component is present. However, these reversals disappear almost completely at subsequent time steps. Moreover, due to influence of the nonaxisymmetric gravitational potential, magnetic reversals are visible between the bar and magnetic arms at time steps $t = 4.75$ Gyr or $t = 6.0$ Gyr in Figure 3.3.

In vertical slices at the beginning of the calculation the mainly randomly distributed toroidal magnetic field is present. Next, at the time step $t = 1.5$ Gyr (Figure 3.3) the odd (dipole-type) configuration of the magnetic field with respect to the galactic plane can be observed. However, this configuration is not permanent and from the time step $t = 2.0$ Gyr in Figure 3.3 the even (quadruple-like) symmetry of the magnetic field is dominant. Additionally, in vertical slices small reversals appear during the whole simulation time.

The cosmic ray driven dynamo action in barred galaxies causes that the total magnetic field (left panel, Figure 3.4) and azimuthal flux (right panel, Figure 3.4) grow exponentially. The magnetic field starts to increase at time $t = 0.1$ Gyr, thus at the beginning of the introducing magnetic dipoles to the galactic disk through SNe explosions. The first phase of the growth is very rapid because the magnetic energy, generated by injected dipoles, accumulates quickly (left panel, Figure 3.4). The second phase of the growth is due to the pure cosmic ray driven dynamo action and lasts until a saturation level is reached at time $t = 4.5$ Gyr. Between $t = 1.45$ Gyr and $t = 1.72$ Gyr the total magnetic energy stops to grow and even decreases. This may be caused by the change of the magnetic field symmetry with respect to the galactic plane: from dipole-like into quadrupole-like (see vertical slices in Figure 3.3 for time steps $t = 1.0$ Gyr, $t = 1.5$ Gyr and $t = 2.0$ Gyr).

The growth of the regular magnetic field due to any dynamo process is defined by the amplification of the azimuthal magnetic flux component (Figure 3.4, right panel). The regular magnetic field grows up on an average timescale (e-folding time) equal to 300 Myr (see Table 3.3). At the beginning of the simulation, especially from $t = 0.1$ Gyr to $t = 0.6$ Gyr, the magnetic flux rapidly changes sign and its absolute value differentiates randomly around the exponential curve. Between $t = 0.72$ Gyr and $t = 1.32$ Gyr the magnetic flux does not increase and remains at the same level. These time intervals correspond to time steps in which reversals and the even symmetry of the toroidal magnetic field are visible (see Figure 3.3). After the time step $t = 1.32$ Gyr the growth of the

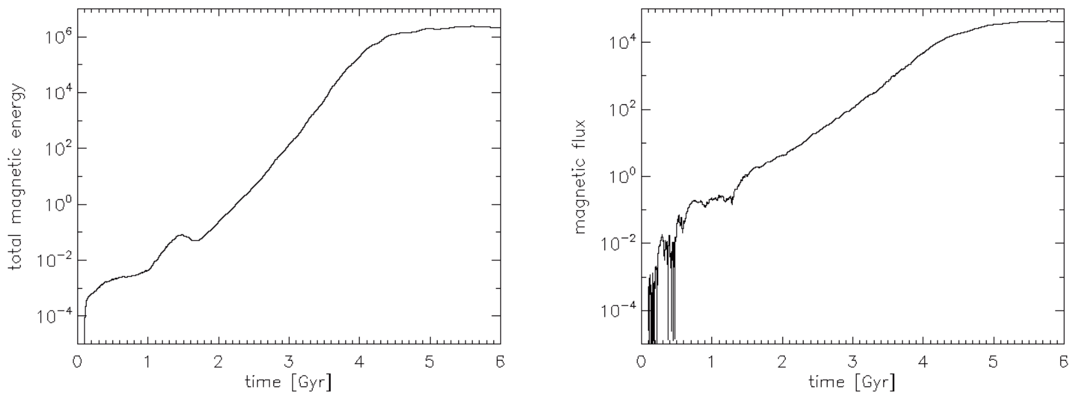

Figure 3.4: The time evolution of the total magnetic field energy B^2 (left panel) and the mean azimuthal flux B_ϕ (right panel) calculated for the reference model RM (BS4).

magnetic flux is clearly exponential and lasts until the equipartition is reached.

3.1.1.4 Polarization maps

In Figure 3.5 I present the magnetic field evolution in time as seen in radio polarymetry for the reference model RM for the same time steps as in Figure 3.3. Polarization maps show the distribution of the polarization angle and polarized intensity superimposed onto the column density during 6.0 Gyr of galactic evolution. All face-on and edge-on polarization maps have been smoothed down to the resolution 40″. Black colour represents regions with the lowest density, while yellow with the highest one. At first, the magnetic field maxima correspond to the gas density enhancements, where SNe explosions are located, what can be easily seen at the time step $t = 0.5$ Gyr (Figure 3.5). At this time step, the magnetic field is present in the gaseous arms as well as in the central part of the galaxy. Additionally, no regular magnetic field is observed in the interarm region. However, at the next time step ($t = 1.0$ Gyr, Figure 3.5) magnetic arms start to detach from gaseous spirals and drift into the interarm region. Thus, at time step $t = 1.5$ Gyr magnetic spiral is clearly visible between the bar and gaseous arms. The drift of magnetic arms is continuous and takes place during the whole simulation time. Its shape changes slightly during the time evolution. For instance, at time steps $t = 2.0$ Gyr or 4.25 Gyr (Figure 3.5) magnetic spiral is defined in the interam region, while at time steps $t = 5.25$ Gyr or 6.0 Gyr (Figure 3.5) it is less visible because it connects with the inner magnetic structures.

The drift of magnetic arms into the interarm area was described in a number of papers (e.g. Kulesza-Żydzik et al. 2009, 2010), where authors concluded that this behaviour is caused by a difference in the angular velocity of magnetic arms and the gaseous spiral. Namely, magnetic arms do not corotate with a gaseous spiral structure, but they follow the general gas motion in the disk, which has a slightly lower angular velocity. However, in

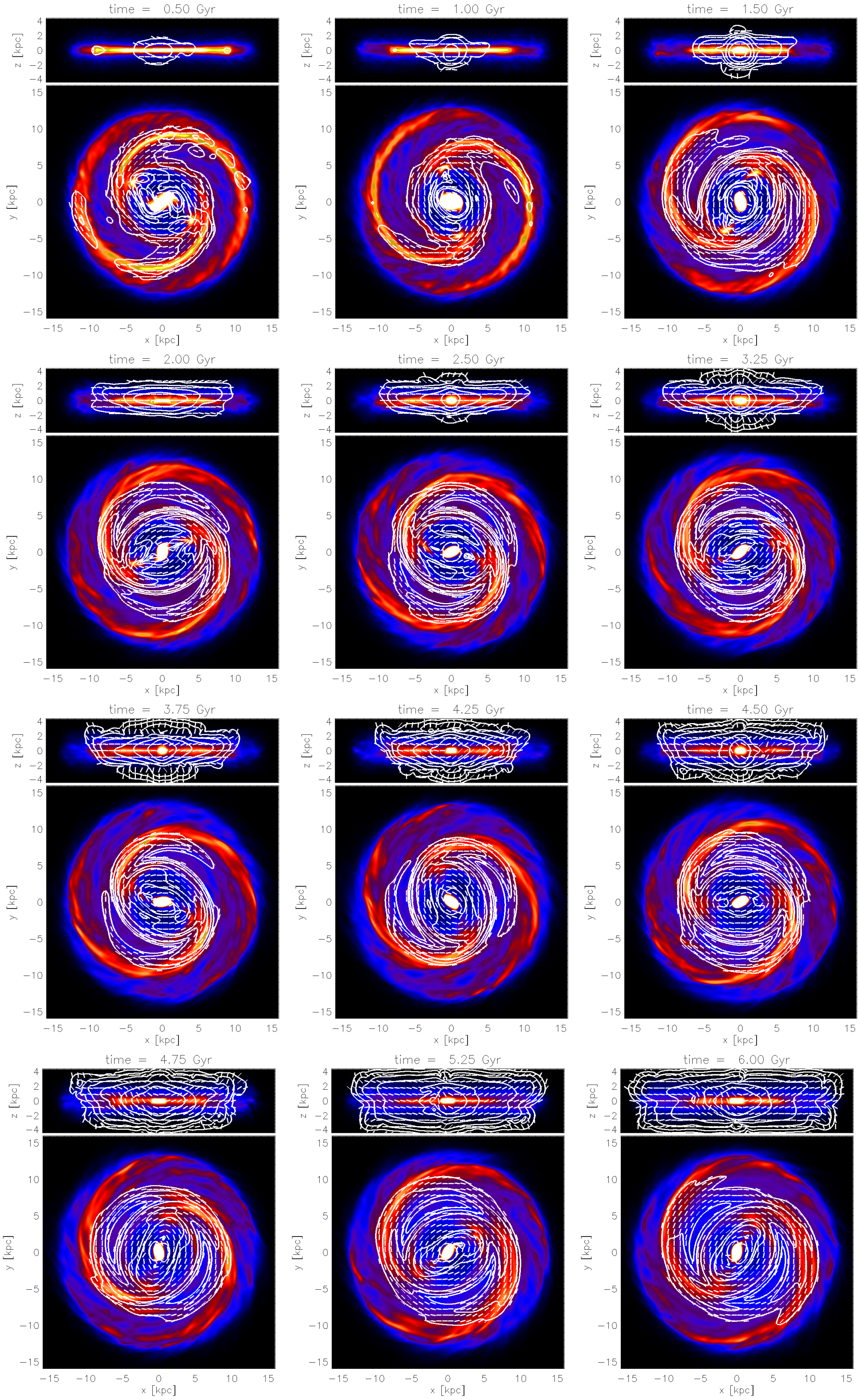

Figure 3.5: Face-on and edge-on polarization maps at $\lambda = 6.2\,\mathrm{cm}$ for selected times steps for the reference model RM (BS4). Polarized intensity (contours) and polarization angles (dashes) are superimposed onto column density plots.

these papers no dynamo action was included. Taking into account the cosmic ray driven dynamo action the similar effect was obtained, but contrary to the previous studies, this effect is observed during the whole simulation time, not only in a short period of the calculation. This difference can be explained as follows. SNe explosions in gaseous arms continuously produce the random magnetic field, which due to the cosmic ray driven dynamo action becomes regular. This regular field is also continuously shifted to the interarm region. Thus, due to the dynamo action and galaxy rotation the magnetic spiral is visible in the zone between the bar and gaseous arms during the whole evolution (see e.g. the time step $t = 4.25$ Gyr in Figure 3.5).

In edge-on maps in Figure 3.5 extended structures of polarization vectors are present. Near the disk plane the magnetic field is mainly parallel to the disk, while in the halo vertical magnetic field component can also be seen (see e.g. the time step $t = 3.75$ Gyr in Figure 3.5). A strong vertical field in the halo is probably transported by an outflow from the galactic disk. The most extended structures are apparent at the late time steps of the calculation (see time steps $t = 5.25$ Gyr or $t = 6.0$ Gyr in Figure 3.5).

Magnetic field vectors in the disk plane are not always parallel to the disk. At later time steps (from $t = 4.25$ Gyr, Figure 3.5), in the bar region, the configuration of the magnetic field changes very rapidly and magnetic field vectors perpendicular to the disk plane are visible (see e.g. the time step $t = 4.75$ Gyr in Figure 3.5). The observed variation of pitch angles is probably caused by large amount of SNe explosions in this region. Namely, the excess of the cosmic ray gas can trigger a very fast outflow from the disk plane in the bar region, which may change the direction of magnetic field vectors.

3.1.1.5 Pitch angles

In order to analyze and compare pitch angles of magnetic and gaseous arms the obtained results are shown in the frame of azimuthal angle in the disk and $\ln(r)$ (r being the galactocentric distance). In this case the logarithmic spiral is represented by a straight line inclined by its pitch angle. In Figure 3.6 the gas density (integrated along the line of sight) with over-plotted contours of the polarized intensity and B-vectors for four time steps ($t = 0.75,\ 1.50,\ 2.25,\ 5.5$ Gyr) are visible. Following these time steps the obvious drift of magnetic field arms into the interarm region occurs (between $r = 6.9$ kpc and $r = 9.5$ kpc). In fact, initially ($t = 0.75$ Gyr, Figure 3.6) magnetic and gaseous arms possess similar pitch angles which are of an order of $\sim -13°$. However, at later time steps magnetic structures move to the interarm region and significantly decrease their pitch angles. Additionally, the estimated mean pitch angle (averaged over azimuthal angle and radius in the galaxy's plane) changes only slightly during the evolution of the galaxy and ranges between $-7°$ and $-8°$.

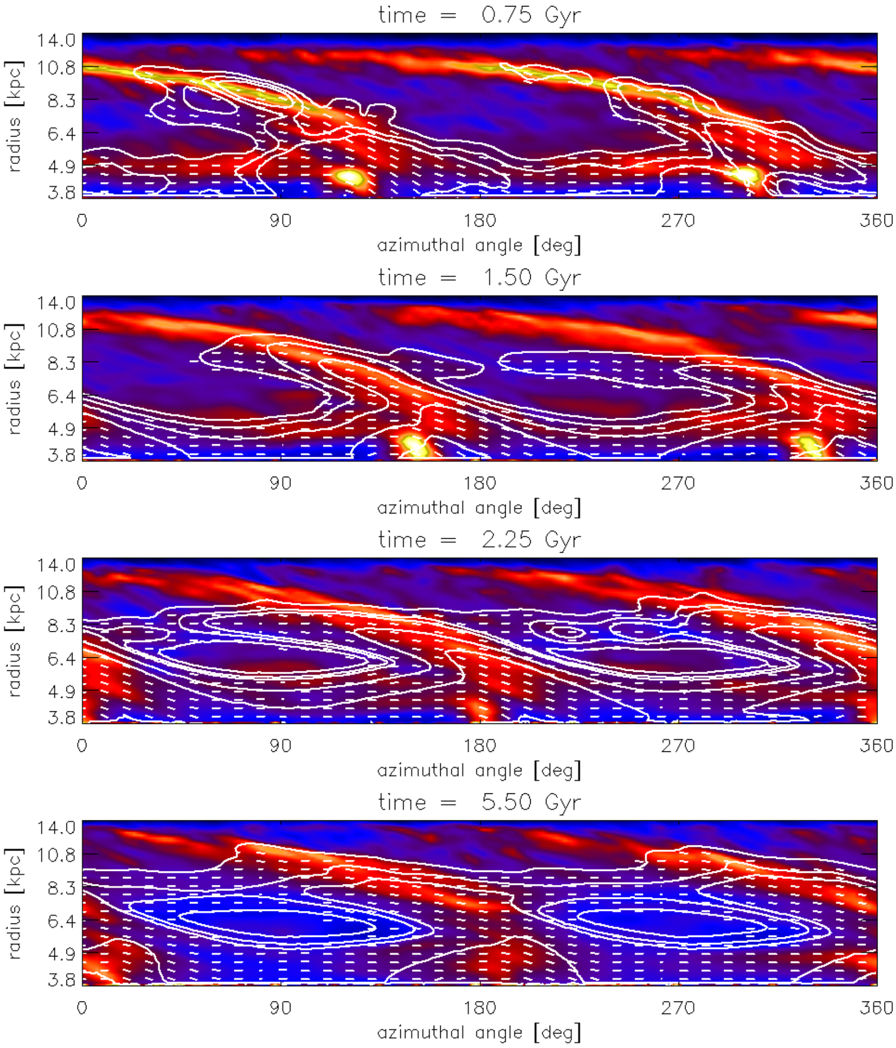

Figure 3.6: The distribution of the polarized intensity and B-vector orientations for the reference model RM (BS4) superimposed onto the gas density at $\lambda = 6.2$ cm in the frame of azimuthal angle in the disk and ln(r). The map has been smoothed to the resolution 40″.

3.1.2 Dependence on the SN frequency

To check how the overall evolution of the barred galaxy and the e-folding time depend on SNe explosions I made several simulations with different values of the SN frequency f_{SN} (see models BS in Table 2.2). Simulation series BS were performed for the following values of SN frequency: $f_{SN} = 1/25\,\mathrm{yr}^{-1}$ for model BS1 $f_{SN} = 1/50\,\mathrm{yr}^{-1}$ for model BS2, $f_{SN} = 1/100\,\mathrm{yr}^{-1}$ for model BS3, $f_{SN} = 1/200\,\mathrm{yr}^{-1}$ for model BS4 and $f_{SN} = 1/500\,\mathrm{yr}^{-1}$ for model BS5. The rest of the input parameters had the same value in all these models.

Gas and cosmic ray density. Gaseous structures produced during the galactic evolution of BS models are very similar. In all cases the nonaxisymmetric gravitational potential of the bar influences the gas density distribution and triggers the accumulation of the

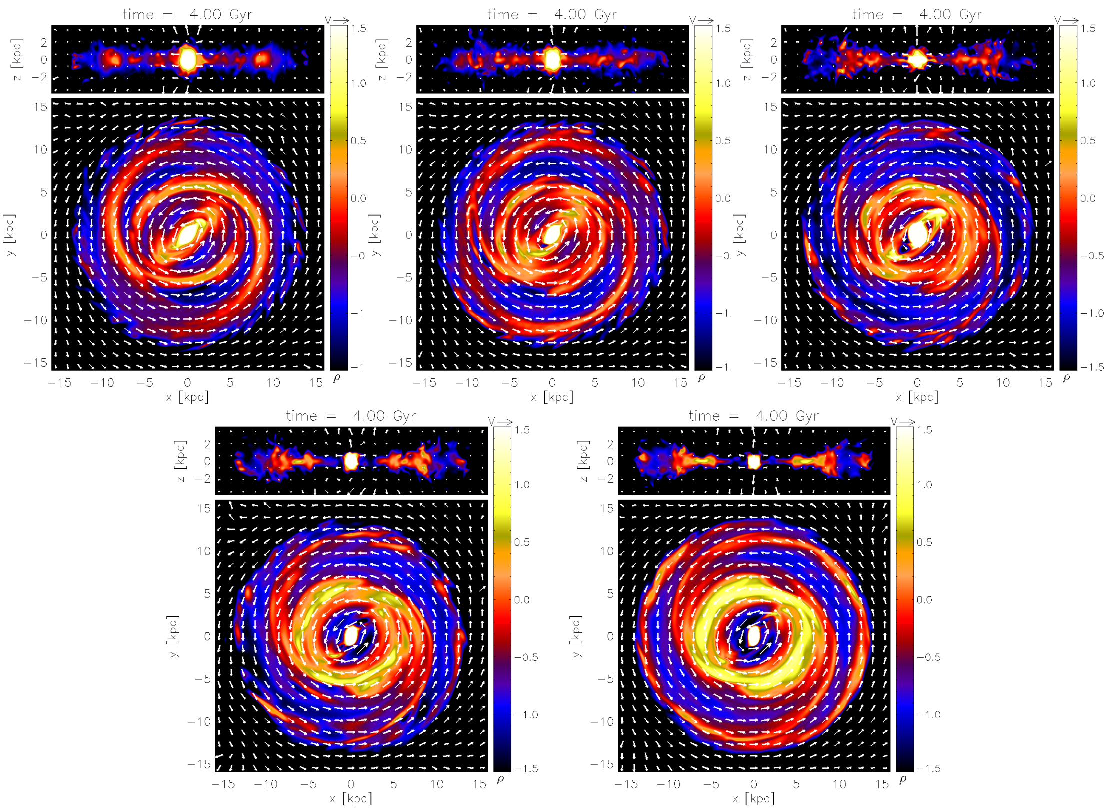

Figure 3.7: The logarithm of the gas density and the velocity field (vectors) in vertical and horizontal slices through the disk center at the time step $t = 4.0\,\mathrm{Gyr}$ for BS models evolution. Top left, middle and right panels correspond to models BS1, BS2 and BS3, respectively, while bottom left and bottom right to models BS4 (RM) and BS5, respectively. The gas density is expressed in units of hydrogen atom per cubic centimeter ($1.0 n_H\,\mathrm{cm}^{-3}$).

gas in the bar region and the creation of gaseous arms. The velocity vectors distribution also does not change with different SN activity. The overall time evolution of the gas and velocity field in BS models is almost the same as in the case of the reference model RM (see Section 3.1.1.1) and is not repeated here.

Although the evolution of gaseous structure looks very similar in all BS models, there are some differences. In Figure 3.7 I present the logarithm of the gas density distribution and velocity field at the time step $t = 4.0\,\mathrm{Gyr}$ for five BS models. To compare the obtained results the same scale values are used in all models. For the highest SN rate (model BS1, top left panel, Figure 3.7) gaseous arms are short and thick, while for the lowest SN activity (model BS5, bottom right panel, Figure 3.7) gaseous arms are thin, long and form an outer ring. In the case of BS3 and BS4 models gaseous spiral is more disordered by SNe explosions than in the other cases. What is more, the enhancement of the gas in the very inner part of the galaxy as well as in the bar region depends on the SN activity. Namely, the higher the SN rate the more gas is transported to the inner part of the galaxy, which can be seen in vertical slices (Figure 3.7). Additionally, for the lowest SN activity gas accumulates closer to the CR radius than to the central part of the galaxy (model BS5, bottom right panel, Figure 3.7). The averaged mass outflow rate grows with increasing SN frequency (Table 3.3). In fact, for model BS1 with the highest SN rate the overall rate of the mass outflow is $4.7 M_\odot$ per year, while for model BS5 with the lowest SN activity the overall rate of the mass outflow is only $0.6 M_\odot$ per year. The cosmic ray gas density distribution is not significantly different in BS models and is similar to that of the reference model RM (see Figure 3.2).

Magnetic field evolution: toroidal field, growth rate, polarization maps, pitch angles In Figures 3.8, 3.9, 3.10, 3.3 and 3.11 the toroidal magnetic field component in horizontal and vertical slices as well as face-on and edge-on polarization maps are shown for BS1, BS2, BS3, BS4 (RM) and BS5 models, respectively. In all models the magnetic field is injected to the galactic disk using the same conditions as in the reference model RM. Model BS4 (RM) was precisely described in the previous Subsection (3.1.1.3).

In the case of model BS1, with the highest SN activity ($f_{SN} = 1/25\,\mathrm{yr}^{-1}$), the initial random toroidal magnetic field component (Figure 3.8, top row, the time step $t = 0.5$ Gyr) evolves into well ordered structures. In the middle of the calculation two magnetic regions with opposite magnetic field direction can be observed (see time steps $t = 1.75$ Gyr or $t = 2.0$ Gyr, Figure 3.8, top row). In the very inner part of the bar, a volume with the positive toroidal magnetic field component is present, both in horizontal and vertical slices. The inner area is encircled by the zone occupied by the negative toroidal magnetic field. At next time steps (from $t = 2.5$ Gyr to $t = 4.5$ Gyr, Figure 3.8, second row) the large scale magnetic field is of even (quadrupole-like) parity with respect to the disk midplane. It is important to note, that no magnetic arms can be observed in BS1 model. Indeed, the amplification of the magnetic field occurs only in the bar region (Figure 3.8, top and second rows). The lack of magnetic arms is also obvious in polarizations maps (Figure 3.8, third and bottom rows). Although gaseous arms are present during the whole simulation time, no magnetic arms can be observed and, in consequence, there is no drift of magnetic arms into the interarm region. This fact is probably caused by a very high SN rate which I applied to this model. Namely, a large number of SNe explosions efficiently introduce turbulent magnetic field to the galactic disk. In the bar region, due to strong shearing and gas compression, turbulent magnetic field is able to evolve into the large scale magnetic field. On the other hand, physical conditions in the outer part of the galactic disk are not sufficient to transform turbulent magnetic fields produced in gaseous arms into regular fields.

The time evolution of the magnetic field for models BS2 ($f_{SN} = 1/50\,\mathrm{yr}^{-1}$), BS4 (RM, $f_{SN} = 1/200\,\mathrm{yr}^{-1}$) and BS5 ($f_{SN} = 1/500\,\mathrm{yr}^{-1}$) looks very similar (compare top and second rows in Figures 3.9, 3.3 and 3.11). In all cases the obtained magnetic fields throughout the disk and halo of the barred galaxy are of even (quadrupole-like) symmetry.

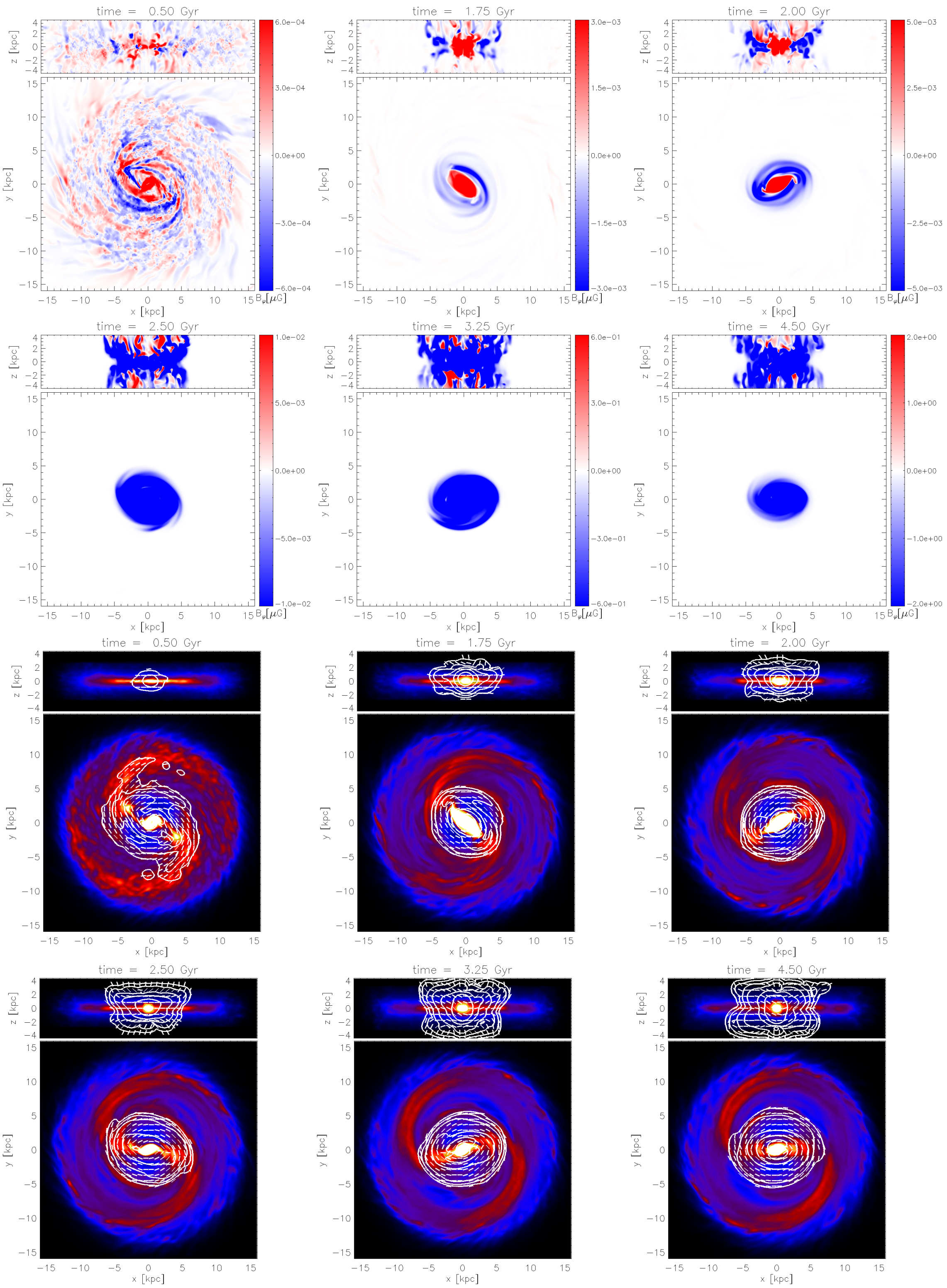

Figure 3.8: *Top panles:* The distribution of the toroidal magnetic field in vertical and horizontal slices through the disk centre for selected times steps for model BS1. Red colour represents regions with the positive toroidal magnetic field, blue with negative, while unmagnetized regions of the volume are white. To enhance weaker structures of the magnetic field in the outer galactic disk (e.g. magnetic arms) the colour scale in magnetic field maps is saturated. The maximum magnetic field strengths in galactic bar and in magnetic arms for selected times steps are given in Table 3.1 and Table 3.2, respectively. *Bottom panles:* Face-on and edge-on polarization maps at $\lambda = 6.2\,\mathrm{cm}$ for selected times steps for the model BS1. Polarized intensity (contours) and polarization angles (dashes) are superimposed onto column density plots.

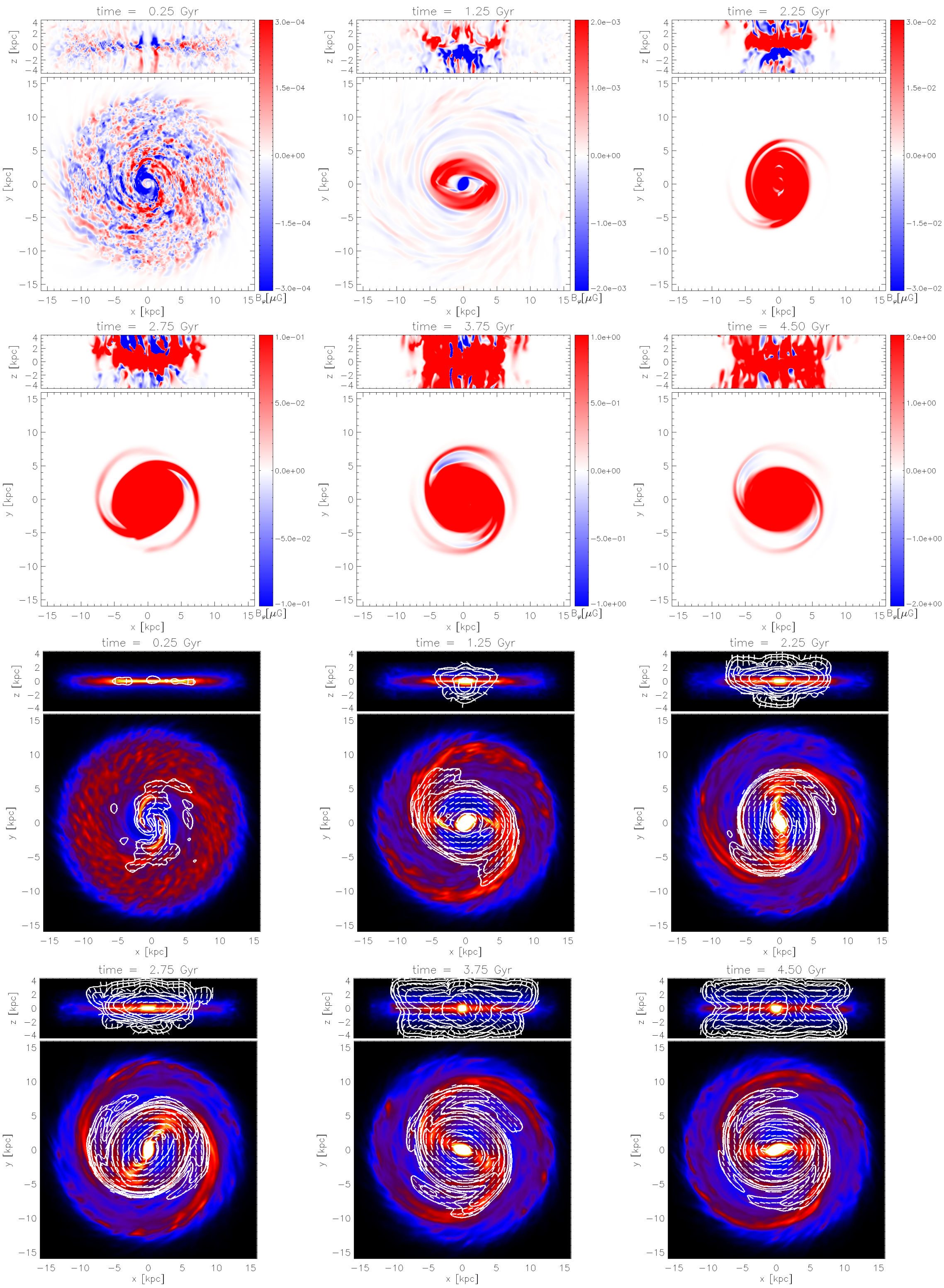

Figure 3.9: *Top panles:* The distribution of the toroidal magnetic field in vertical and horizontal slices through the disk centre for selected times steps for model BS2. Red colour represents regions with the positive toroidal magnetic field, blue with negative, while unmagnetized regions of the volume are white. To enhance weaker structures of the magnetic field in the outer galactic disk (e.g. magnetic arms) the colour scale in magnetic field maps is saturated. The maximum magnetic field strengths in galactic bar and in magnetic arms for selected times steps are given in Table 3.1 and Table 3.2, respectively. *Bottom panles:* Face-on and edge-on polarization maps at λ = 6.2 cm for selected times steps for the model BS2. Polarized intensity (contours) and polarization angles (dashes) are superimposed onto column density plots.

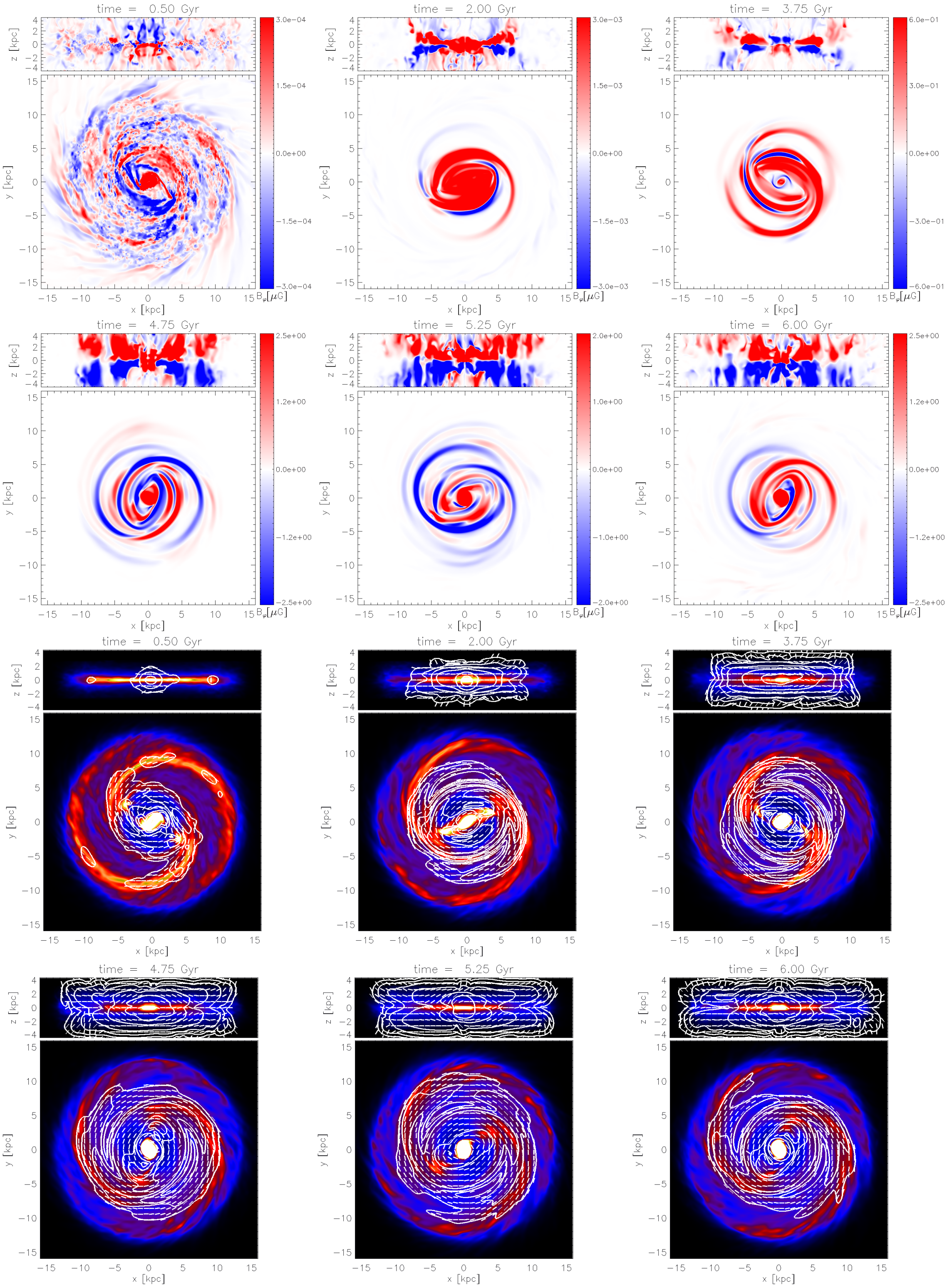

Figure 3.10: *Top panles:* The distribution of the toroidal magnetic field in vertical and horizontal slices through the disk centre for selected times steps for model BS3. Red colour represents regions with the positive toroidal magnetic field, blue with negative, while unmagnetized regions of the volume are white. To enhance weaker structures of the magnetic field in the outer galactic disk (e.g. magnetic arms) the colour scale in magnetic field maps is saturated. *Bottom panles:* Face-on and edge-on polarization maps at $\lambda = 6.2\,\mathrm{cm}$ for selected times steps for the model BS3. Polarized intensity (contours) and polarization angles (dashes) are superimposed onto column density plots.

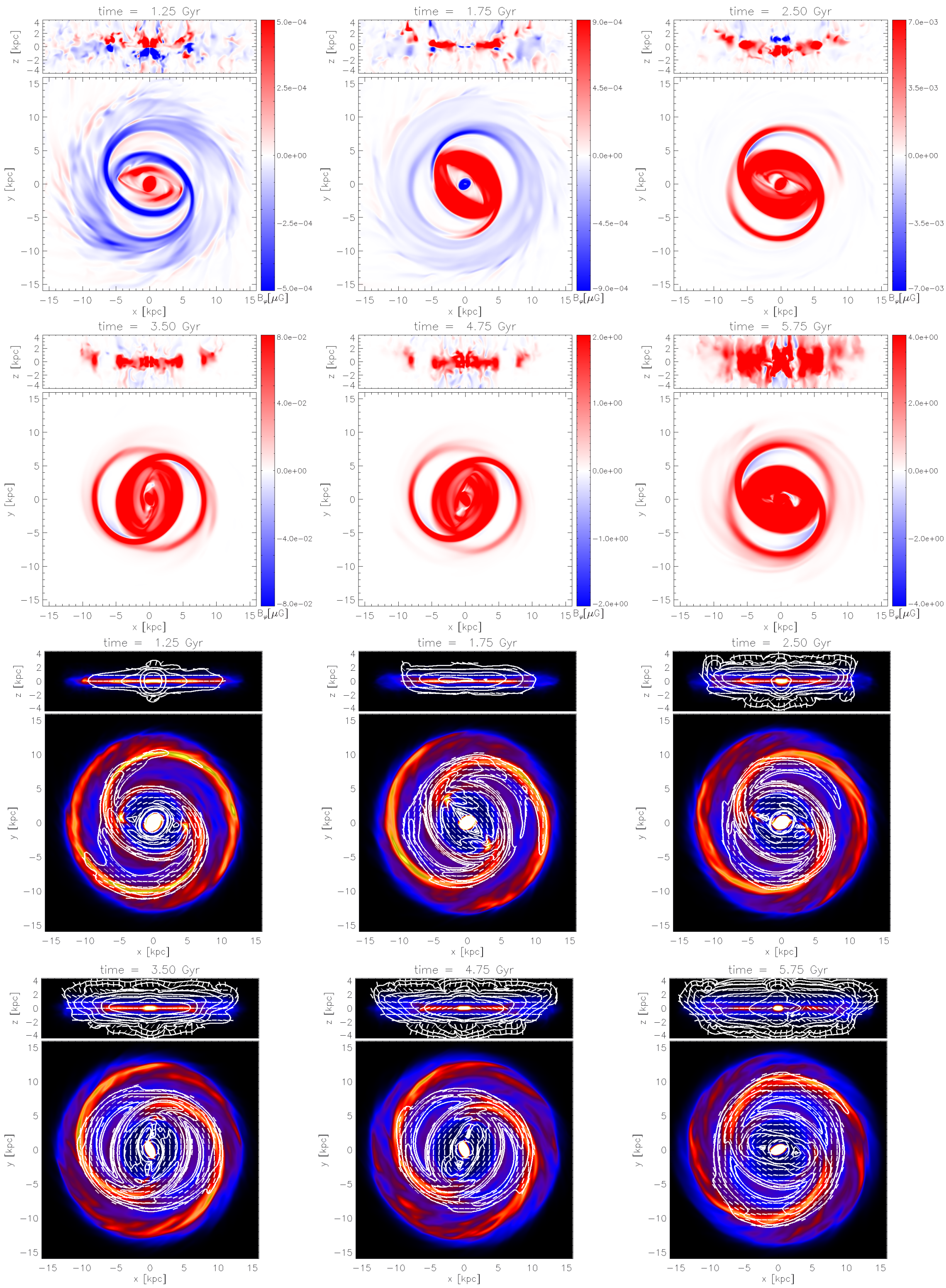

Figure 3.11: *Top panles:* The distribution of the toroidal magnetic field in vertical and horizontal slices through the disk centre for selected times steps for model BS5. Red colour represents regions with the positive toroidal magnetic field, blue with negative, while unmagnetized regions of the volume are white. To enhance weaker structures of the magnetic field in the outer galactic disk (e.g. magnetic arms) the colour scale in magnetic field maps is saturated. The maximum magnetic field strengths in galactic bar and in magnetic arms for selected times steps are given in Table 3.1 and Table 3.2, respectively. *Bottom panles:* Face-on and edge-on polarization maps at $\lambda = 6.2\,\mathrm{cm}$ for selected times steps for the model BS5. Polarized intensity (contours) and polarization angles (dashes) are superimposed onto column density plots.

What is more, in each model generation of magnetic arms can be observed (see e.g. the time step $t = 3.75$ Gyr in second row in Figure 3.9 or the time step $t = 4.25$ Gyr in top row in Figure 3.3 or the time step $t = 5.75$ Gyr in second row in Figure 3.11). However, in model BS2 magnetic arms are weaker and thinner than in models BS4 (RM) and BS5. In the case of polarization maps (see third and bottom rows in Figures 3.9, 3.3 and 3.11) magnetic arms and their drift to the interarm region can be observed in face-on maps in all models. Additionally, polarization vectors in edge-on maps reveal the so-called X-shaped structure.

An odd (dipole-type) configuration of the magnetic field with respect to the galactic plane appears in all models in the early stage of evolution. However, only in model BS3 ($f_{SN} = 1/100\,\mathrm{yr}^{-1}$) this configuration is observed from the time step $t = 2.0$ Gyr (top row in Figure 3.10) and lasts till the end of the simulation. The obtained symmetry of the magnetic field in model BS3 causes that the toroidal magnetic field in the galactic disk (Figure 3.10, top and second rows) often changes sign during the evolution. For instance, at first ($t = 2.0$ Gyr, top row in Figure 3.10) the toroidal magnetic field component in magnetic arms is positive in the southern arm and negative in the northern one, next it is positive ($t = 3.75$ Gyr, top row in Figure 3.10) or negative ($t = 4.75$ Gyr, second row in Figure 3.10) in both arms and, finally, ($t = 6.0$ Gyr, second row in Figure 3.10) it is again positive in the southern arm and negative in the northern arm. Reversals of magnetic field are also visible in the bar region almost at each time step. The presence of magnetic reversals in the galactic plane results from the vertical configuration of the magnetic field. Namely, in regions where the magnetic field from zones below the disk dominates, the negative toroidal magnetic field is observed in the galactic plane. On the other hand, in areas where the magnetic field above the galactic disk dominates, the positive toroidal magnetic field appears in the galactic plane.

In Table 3.1 and Table 3.2 maximum magnetic field strengths in magnetic arms and galactic bar for selected time steps for all BS models are present. The highest values of the magnetic field are reached for models with a strong SN activity. For models BS1 ($f_{SN} = 1/25\,\mathrm{yr}^{-1}$) and BS2 ($f_{SN} = 1/50\,\mathrm{yr}^{-1}$) the maximum magnetic field strengths in the bar region are $88.8\,\mu$G and $85.1\,\mu$G, respectively. On the other hand, for models with moderate (BS3, $f_{SN} = 1/100\,\mathrm{yr}^{-1}$ and BS4, $f_{SN} = 1/200\,\mathrm{yr}^{-1}$) and low (BS5, $f_{SN} = 1/500\,\mathrm{yr}^{-1}$) values of SN rate the maximum magnetic field strengths in the bar region are equal to $71.3\,\mu$G, $53.4\,\mu$G and $59.3\,\mu$G, respectively. In the case of magnetic arms, the maximum magnetic field strengths ($9.5\,\mu$G) is obtained for model BS4 (RM). Similar values are observed for model BS3 ($5.9\,\mu$G) and BS5 ($8.6\,\mu$G). For models with high SN activity the maximum field in magnetic arms is weaker, about $2.1\,\mu$G in model BS2 or almost none ($4.7 \cdot 10^{-2}\,\mu$G) in the case of model BS1. Maximum values of the magnetic field obtained for BS models are shown in Table 3.3.

For model BS1 ($f_{SN} = 1/25\,\mathrm{yr}^{-1}$), with the strongest magnetic field in the bar, the

	Model				
	BS1	BS2	BS3	BS4 (RM)	BS5
$f_{SN}[\,\mathrm{yr}^{-1}]$	1/25	1/50	1/100	1/200	1/500
Time [Gyr]			$B_{\varphi}^{bar}[\,\mu\mathrm{G}]$		
0.25	$1.6 \cdot 10^{-3}$	$1.2 \cdot 10^{-3}$	$1.1 \cdot 10^{-3}$	$1.0 \cdot 10^{-3}$	$4.6 \cdot 10^{-4}$
0.50	$5.3 \cdot 10^{-3}$	$3.4 \cdot 10^{-3}$	$5.2 \cdot 10^{-3}$	$1.9 \cdot 10^{-3}$	$3.3 \cdot 10^{-3}$
0.75	$9.8 \cdot 10^{-3}$	$4.6 \cdot 10^{-3}$	$8.9 \cdot 10^{-3}$	$2.7 \cdot 10^{-3}$	$4.1 \cdot 10^{-3}$
1.00	$1.9 \cdot 10^{-2}$	$1.6 \cdot 10^{-2}$	$2.1 \cdot 10^{-2}$	$3.6 \cdot 10^{-3}$	$4.1 \cdot 10^{-3}$
1.25	$2.3 \cdot 10^{-2}$	$4.0 \cdot 10^{-2}$	$2.8 \cdot 10^{-2}$	$1.2 \cdot 10^{-2}$	$4.8 \cdot 10^{-3}$
1.50	$5.6 \cdot 10^{-2}$	$4.1 \cdot 10^{-2}$	$7.8 \cdot 10^{-2}$	$3.8 \cdot 10^{-2}$	$9.0 \cdot 10^{-3}$
1.75	$7.9 \cdot 10^{-2}$	$4.3 \cdot 10^{-1}$	$3.9 \cdot 10^{-2}$	$2.1 \cdot 10^{-2}$	$1.0 \cdot 10^{-2}$
2.00	$1.5 \cdot 10^{-1}$	$6.8 \cdot 10^{-1}$	$6.5 \cdot 10^{-2}$	$1.1 \cdot 10^{-2}$	$1.4 \cdot 10^{-2}$
2.25	$1.4 \cdot 10^{-1}$	1.9	$7.5 \cdot 10^{-2}$	$2.4 \cdot 10^{-2}$	$3.0 \cdot 10^{-2}$
2.50	$4.0 \cdot 10^{-1}$	6.4	$1.6 \cdot 10^{-1}$	$1.1 \cdot 10^{-1}$	$6.9 \cdot 10^{-2}$
2.75	3.8	17.5	$2.5 \cdot 10^{-1}$	$2.5 \cdot 10^{-1}$	$9.3 \cdot 10^{-2}$
3.00	12.3	55.3	$7.9 \cdot 10^{-1}$	1.2	$1.7 \cdot 10^{-1}$
3.25	57.6	45.1	1.1	2.1	$3.1 \cdot 10^{-1}$
3.50	64.7	55.5	2.6	6.9	$5.3 \cdot 10^{-1}$
3.75	71.6	61.9	2.8	20.4	$9.6 \cdot 10^{-1}$
4.00	85.0	85.1	4.0	50.6	2.3
4.25	88.8	82.1	9.1	53.2	5.2
4.50	87.3	78.7	19.6	52.1	12.1
4.75	85.1	–	36.2	47.3	24.6
5.00	–	–	61.0	50.8	31.4
5.25	–	–	52.6	51.4	51.8
5.50	–	–	59.3	50.1	45.3
5.75	–	–	71.3	45.1	54.2
6.00	–	–	67.4	53.4	59.3

Table 3.1: The maximum magnetic field strengths in the galactic bar for selected time steps for models with different SN frequency f_{SN} (see models BS in Table 2.2).

lowest value of the mean magnetic field is obtained $B_{mean} = 3.7\,\mu$G (see Table 3.3). This is a consequence of a very low magnetic field (of an order of $10^{-2}\,\mu$G) in the outer part of the disk, outside the CR radius. On the other hand, for model BS4 ($f_{SN} = 1/200\,\mathrm{yr}^{-1}$) the mean magnetic field reaches the highest value $B_{mean} = 10.2\,\mu$G (see Table 3.3). Contrary to BS1 model, in BS4 model the strong value of the magnetic field in the spiral structure area (B_{φ}^{arms}) increases the mean magnetic field. For models BS2, BS3 and BS5 values of the mean magnetic field are very similar and approximately equal to $\sim 7\,\mu$G (see Table 3.3). Additionally, the estimated mean pitch angle (averaged over azimuthal angle and radius in the galaxy's plane) grows with increasing SN activity and ranges between $-13°$ for model BS1 and $-6°$ for model BS5 (see last column in Table 3.3).

In Figure 3.12 the evolution of the total flux (bottom panel) of the azimuthal magnetic

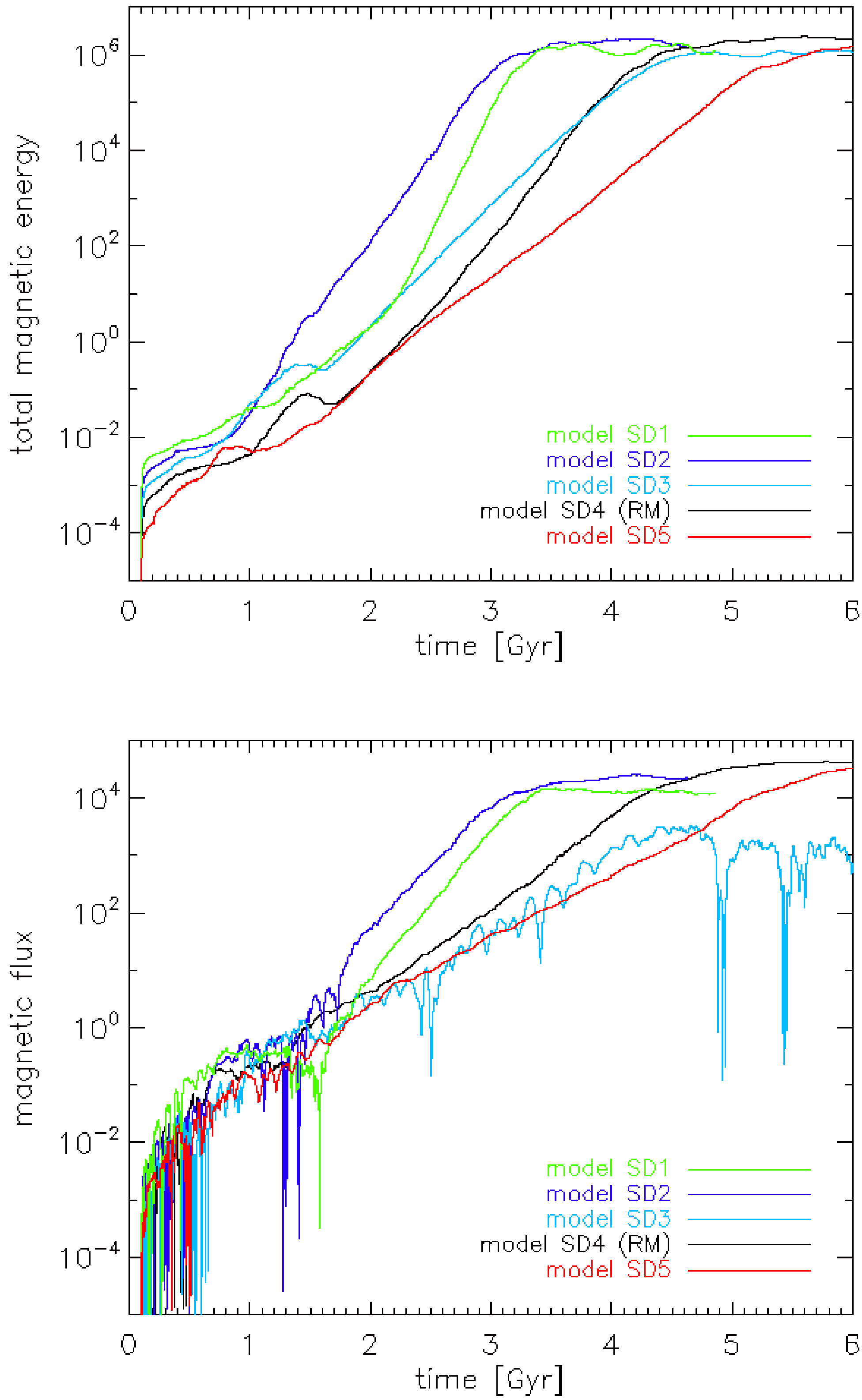

Figure 3.12: The time evolution of the total magnetic energy B^2 (top panel) and the mean azimuthal flux B_ϕ (bottom panel) for different values of the SN frequency f_{SN} in the simulation series BS. The colour curves represent respectively cases of $f_{SN} = 1/25\,\mathrm{yr}^{-1}$ (BS1), $f_{SN} = 1/50\,\mathrm{yr}^{-1}$ (BS2), $f_{SN} = 1/100\,\mathrm{yr}^{-1}$ (BS3), $f_{SN} = 1/200\,\mathrm{yr}^{-1}$ (BS4) and $f_{SN} = 1/500\,\mathrm{yr}^{-1}$ (BS5).

	Model				
	BS1	BS2	BS3	BS4 (RM)	BS5
$f_{SN}[\,\mathrm{yr}^{-1}]$	1/25	1/50	1/100	1/200	1/500
Time [Gyr]			$B_\varphi^{arms}[\,\mu\mathrm{G}]$		
0.25	$6.9\cdot10^{-4}$	$4.9\cdot10^{-4}$	$4.9\cdot10^{-4}$	$4.5\cdot10^{-4}$	$4.1\cdot10^{-4}$
0.50	$6.6\cdot10^{-4}$	$9.6\cdot10^{-4}$	$6.2\cdot10^{-4}$	$7.9\cdot10^{-4}$	$5.5\cdot10^{-4}$
0.75	$6.5\cdot10^{-4}$	$7.1\cdot10^{-4}$	$9.6\cdot10^{-4}$	$7.4\cdot10^{-4}$	$7.9\cdot10^{-4}$
1.00	$5.0\cdot10^{-4}$	$5.3\cdot10^{-4}$	$5.5\cdot10^{-4}$	$4.9\cdot10^{-4}$	$8.7\cdot10^{-4}$
1.25	$3.5\cdot10^{-4}$	$5.2\cdot10^{-4}$	$3.2\cdot10^{-4}$	$5.1\cdot10^{-4}$	$6.7\cdot10^{-4}$
1.50	$3.9\cdot10^{-4}$	$3.5\cdot10^{-4}$	$4.1\cdot10^{-4}$	$4.4\cdot10^{-4}$	$8.8\cdot10^{-4}$
1.75	$5.4\cdot10^{-4}$	$1.8\cdot10^{-3}$	$1.2\cdot10^{-3}$	$2.5\cdot10^{-3}$	$1.7\cdot10^{-3}$
2.00	$1.7\cdot10^{-4}$	$3.2\cdot10^{-3}$	$4.0\cdot10^{-3}$	$9.2\cdot10^{-3}$	$5.8\cdot10^{-3}$
2.25	$1.1\cdot10^{-4}$	$3.2\cdot10^{-2}$	$6.8\cdot10^{-3}$	$1.6\cdot10^{-2}$	$2.9\cdot10^{-2}$
2.50	$5.5\cdot10^{-5}$	$1.8\cdot10^{-1}$	$5.0\cdot10^{-2}$	$3.8\cdot10^{-2}$	$3.9\cdot10^{-2}$
2.75	$2.6\cdot10^{-4}$	$7.1\cdot10^{-1}$	$1.4\cdot10^{-1}$	$1.1\cdot10^{-1}$	$8.2\cdot10^{-2}$
3.00	$3.8\cdot10^{-3}$	$9.3\cdot10^{-1}$	$4.3\cdot10^{-1}$	$1.9\cdot10^{-1}$	$1.4\cdot10^{-1}$
3.25	$8.0\cdot10^{-3}$	1.7	$7.1\cdot10^{-1}$	$3.1\cdot10^{-1}$	$2.9\cdot10^{-1}$
3.50	$4.7\cdot10^{-2}$	2.1	1.9	$6.8\cdot10^{-1}$	$3.9\cdot10^{-1}$
3.75	$2.2\cdot10^{-2}$	1.3	2.3	1.8	$7.2\cdot10^{-1}$
4.00	$7.2\cdot10^{-3}$	1.4	2.4	2.7	1.2
4.25	$3.5\cdot10^{-3}$	1.8	5.9	5.5	2.3
4.50	$5.1\cdot10^{-3}$	1.7	5.6	7.6	3.4
4.75	–	–	5.5	9.1	5.4
5.00	–	–	4.6	9.2	6.8
5.25	–	–	4.9	9.5	7.8
5.50	–	–	3.8	8.9	7.9
5.75	–	–	3.7	7.3	8.4
6.00	–	–	2.9	8.7	8.6

Table 3.2: The maximum magnetic field strengths in magnetic arms for selected time steps for models with different SN frequency f_{SN} (see models BS in Table 2.2).

field component and the total magnetic field energy (top panel) for all BS models are shown. It is apparent that for all models a very similar exponential growth is obtained. The fastest amplification of the total magnetic field is observed for models with the highest SN rate, namely for models BS1 and BS2. In these cases the magnetic field reaches an equipartition approximately at time $t \sim 3.1 - 3.3\,\mathrm{Gyr}$. The equipartition in models BS3 and BS4 (RM) is achieved approximately one Gyr later than in models BS1 and BS2. For model BS5, with the lowest SN rate, the magnetic field energy attains its saturation value at time $t \sim 5.5\,\mathrm{Gyr}$.

The final saturation levels of the magnetic flux are the same as in the case of the total magnetic energy. The e-folding times of magnetic flux deduced from the bottom panel of Figure 3.12 are respectively 230 Myr for model BS1 ($f_{SN} = 1/25\,\mathrm{yr}^{-1}$), 194 Myr for

Model	f_{SN} [yr^{-1}]	τ [Myr]	M_{lost} [$M_\odot$ yr^{-1}]	max B_φ^{bar} [μG]	max B_φ^{arms} [μG]	B_{mean} [μG]	$-p$ [°]
BS1	1/25	230	4.7	88.8	$4.7 \cdot 10^{-2}$	3.7	12 – 13
BS2	1/50	194	3.2	85.1	2.1	6.4	10 – 11
BS3	1/100	326	1.7	71.3	5.9	7.1	9 – 10
BS4	1/200	300	1.1	53.4	9.5	10.2	7 – 8
BS5	1/500	360	0.6	59.3	8.6	7.9	6 – 7

Table 3.3: Overview of the obtained parameters characterizing BS models. Subsequent columns show: the model name, the SN frequency f_{SN}, e-folding time τ, the rate of the mass outflow M_{lost}, the maximum magnetic field in the galactic bar max B_φ^{bar} and in magnetic arms max B_φ^{arms}, the mean magnetic field B_{mean} (equipartition state) and pitch angles p.

model BS2 ($f_{SN} = 1/50\,\mathrm{yr}^{-1}$), 326 Myr for model BS3 ($f_{SN} = 1/100\,\mathrm{yr}^{-1}$), 300 Myr for model BS4 ($f_{SN} = 1/200\,\mathrm{yr}^{-1}$) and 360 Myr for model BS5 ($f_{SN} = 1/500\,\mathrm{yr}^{-1}$) (see Table 3.3). It can be noticed that by changing the number of SNe explosions, one does not get significantly different results. In fact, in all simulations two regions of growth of the magnetic flux can be distinguished. The first period starts at the beginning of calculations and lasts until time $t \sim 2.0$ Gyr (bottom panel in Figure 3.12). During this time interval the magnetic flux changes sign and its absolute value variates randomly around the exponential curve. These variations are associated with the evolution of magnetic field structures. Namely, in all models during this time the initial random toroidal magnetic field component evolves and forms large scale magnetic structures with odd symmetry with respect to the galactic plane. Reversals of the magnetic field are also visible, mostly in the bar region, almost at each time step until $t = 2.0$ Gyr (bottom panel in Figure 3.12). On the other hand, after time $t \sim 2.0$ Gyr the total azimuthal flux stops to reverse. Then the toroidal magnetic field direction becomes almost uniform and reversals, if any, are very weak and small (see panels in second row in Figures 3.8, 3.9, 3.3 and 3.11). The only exception is model BS3 where variations of the magnetic flux as well as reversals of the toroidal magnetic field component (Figure 3.10) are visible during the whole simulation time. At the end of the calculation, when the magnetic field reaches an equipartition, two periods with strong variations of the magnetic flux sign can be observed. What is more, in model BS3 the level at which the magnetic flux is in the saturation regime is ten times smaller than the equipartition level for other models.

The above results show that the magnetic field amplification in barred galaxies is relatively insensitive to the magnitude of SN rate. It means that the cosmic ray driven dynamo process is efficient for a wide range of SN activity.

3.2 Simulations of the ringed galaxy - NGC 4736

According to Chyży & Buta (2008) the observed configuration of the magnetic field in the ringed galaxy NGC 4736 may be explained by the pure dynamo action. In this section I revise this statement by checking how the cosmic ray driven dynamo influences the magnetic field and gas distributions in the ringed galaxy NGC 4736.

In the case of simulations of the barred galaxy I selected one model that, in my opinion, represents the best example from the sample of the barred galaxy models. However, for simulations of the ringed galaxy it is very hard to choose one reference model. Thus, below I describe the time evolution of all models of the ringed galaxy. As in the case of the barred galaxy I run several models with different SN frequency. An overview of the various models can be found in Table 2.4. The distribution of the gas density and cosmic ray energy density, polarization maps, pitch angles, the distribution of the toroidal magnetic field component and the growth rate of the magnetic energy are studied in the case of each model. Although in some models of the ringed galaxy magnetic field reaches the equipartition very fast (around 2 Gyr), all simulations are stopped at time $t = 6$ Gyr.

3.2.1 Gas dynamics and cosmic ray energy density - inner and outer rings

During the first stage of all simulations, when SNe explosions or nonaxisymmetrical gravitational potentials of the bar and oval are not present, the system evolves to reach dynamical equilibrium between gas and cosmic rays. After that time ($t = 0.1$ Gyr) the influence of the cosmic ray driven dynamo action on the evolution of the ringed galaxy model can be studied in detail.

In this section basic dynamical features of all models of the ringed galaxy are described. The distribution of the logarithm of the gas density with overplotted vectors of the velocity field in vertical and horizontal slices through the disk centre for selected time steps is shown in top and third panels in figures: model RS1 ($f_{SN} = 1/50\,\mathrm{yr}^{-1}$) Figure 3.13, model RS2 ($f_{SN} = 1/100\,\mathrm{yr}^{-1}$) Figure 3.14, model RS3 ($f_{SN} = 1/200\,\mathrm{yr}^{-1}$) Figure 3.15, model RS4 ($f_{SN} = 1/300\,\mathrm{yr}^{-1}$) Figure 3.16 and model RS5 ($f_{SN} = 1/500\,\mathrm{yr}^{-1}$) Figure 3.17. In the same figures in second and bottom panels I present the corresponding gas density distribution through the disk centre in the x and y directions. In order to improve readability of plots in second and bottom panels in Figures 3.13, 3.14, 3.15, 3.16 and 3.17 after the time step $t = 0.2$ Gyr the inner very dense part (where the small bar is present) is not being taken into account. Moreover, the position of the ILR and OLR Lindblad resonances is marked by red and green lines, respectively.

At the beginning of all simulations, the ringed galaxy is in magnetohydrodynamic equilibrium. From $t = 0.1$ Gyr to $t = 0.4$ Gyr the oval and the small bar are gradually

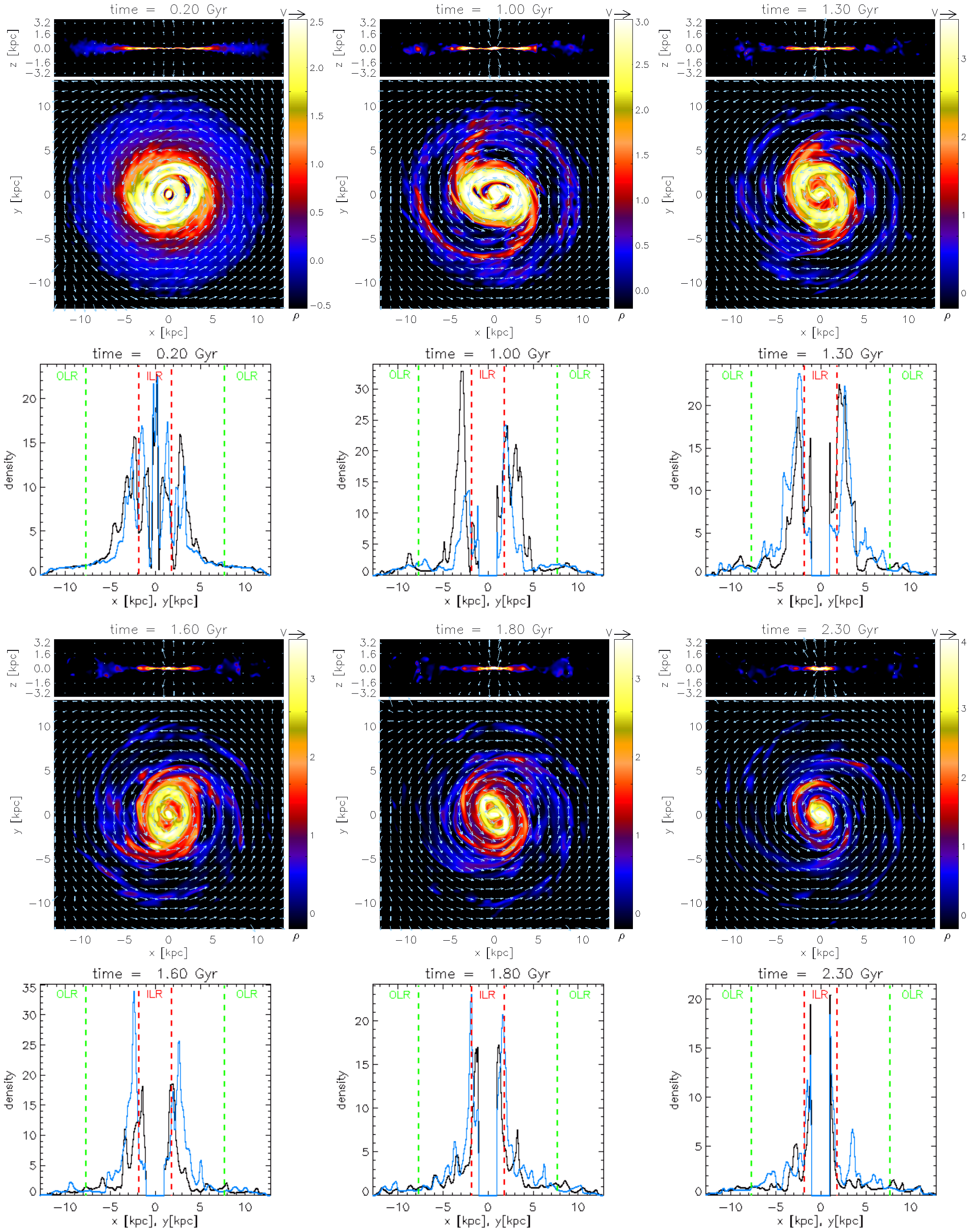

Figure 3.13: *Top and third panels:* The logarithm of the gas density and the gas velocity field (vectors) in vertical and horizontal slices through the disk centre for selected time steps for model RS1. The gas density is expressed in units of hydrogen atom per cubic centimeter ($1.0 n_H\,\mathrm{cm}^{-3}$). *Second and bottom panels:* The distribution of the gas density through the disk centre in the x (black line) and y (blue line) directions for selected time steps for model RS1.

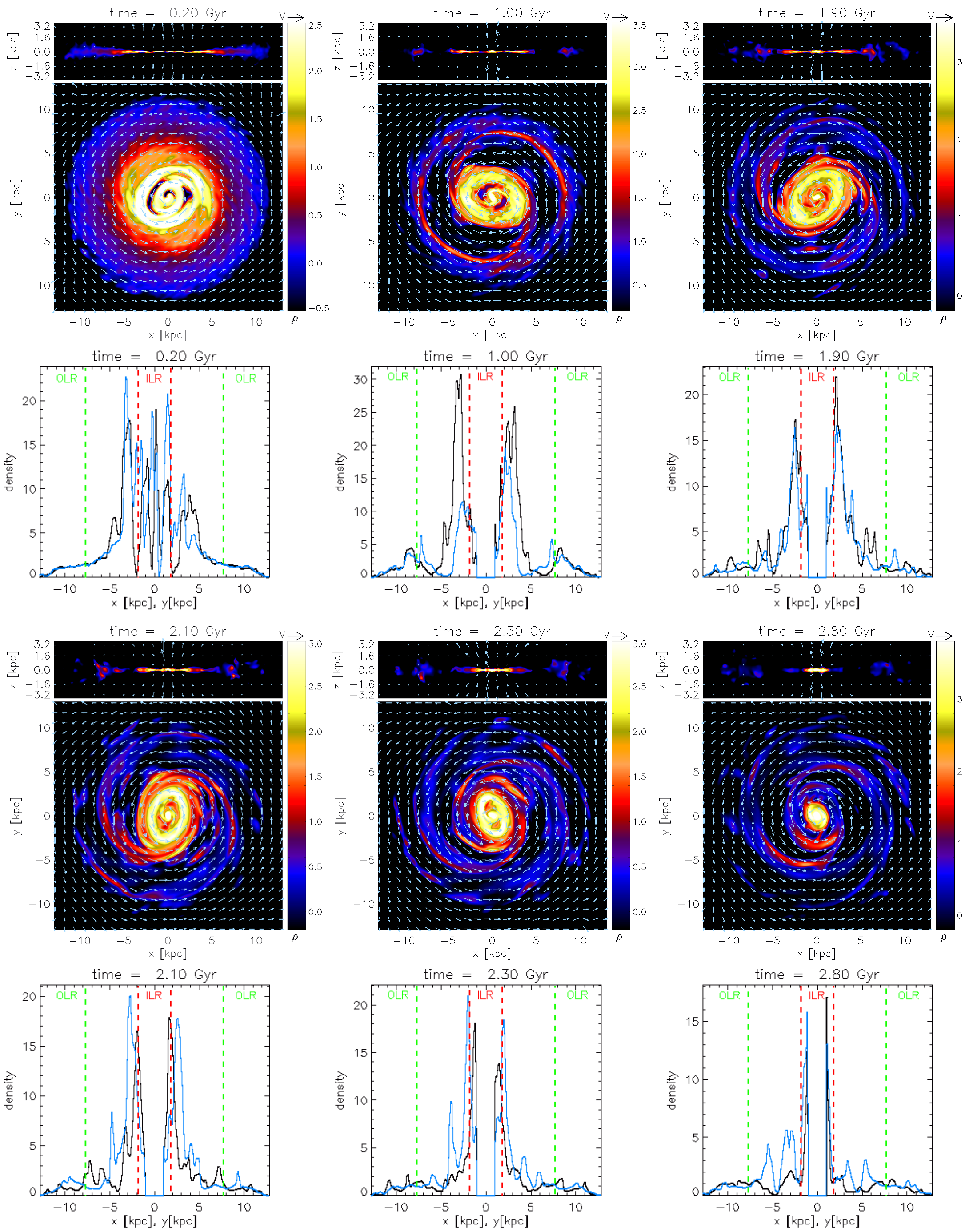

Figure 3.14: *Top and third panels:* The logarithm of the gas density and the gas velocity field (vectors) in vertical and horizontal slices through the disk centre for selected time steps for model RS2. The gas density is expressed in units of hydrogen atom per cubic centimeter ($1.0 n_H\,\mathrm{cm}^{-3}$). *Second and bottom panels:* The distribution of the gas density through the disk centre in the x (black line) and y (blue line) directions for selected time steps for model RS2.

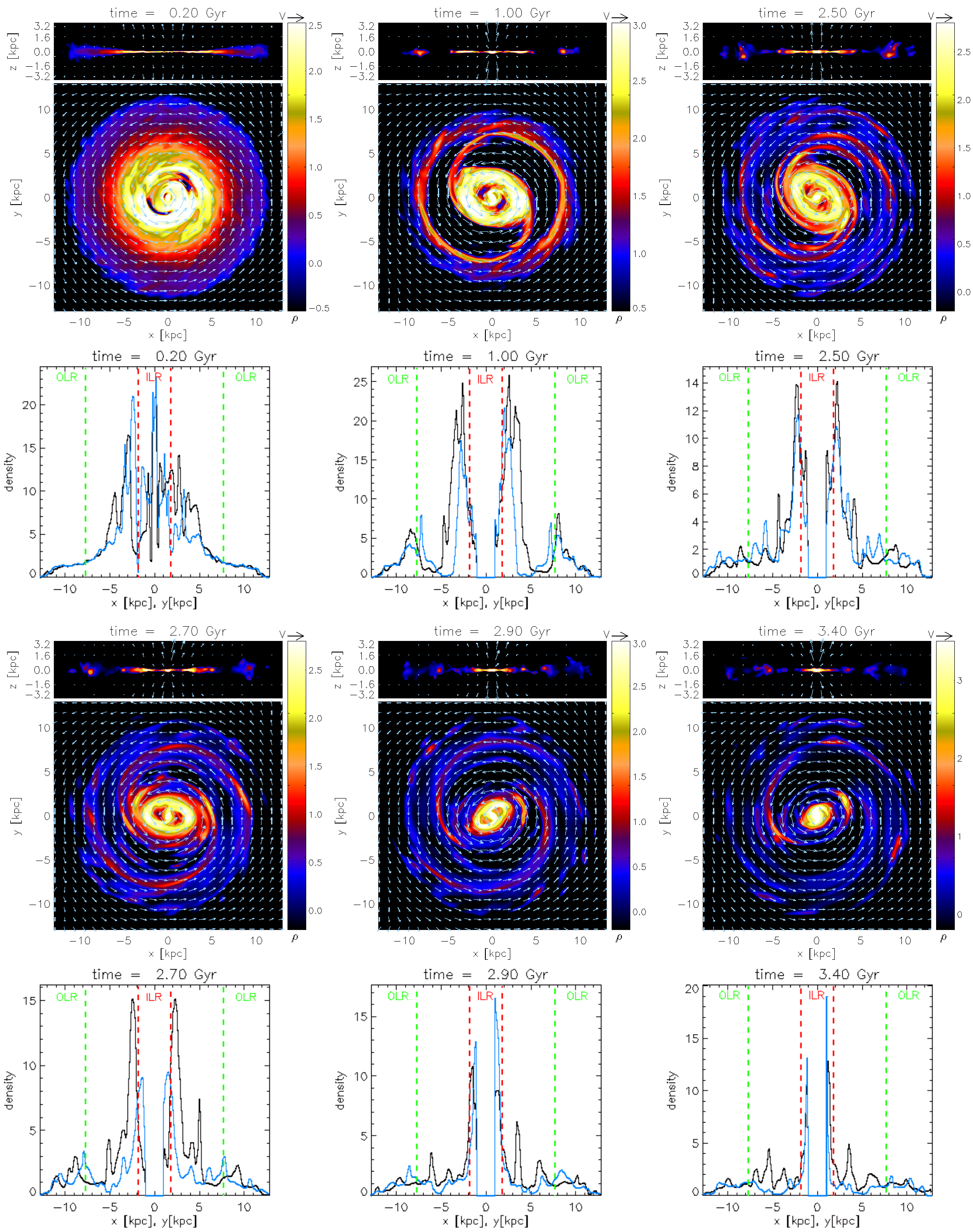

Figure 3.15: *Top and third panels:* The logarithm of the gas density and the gas velocity field (vectors) in vertical and horizontal slices through the disk centre for selected time steps for model RS3. The gas density is expressed in units of hydrogen atom per cubic centimeter ($1.0 n_H\,\mathrm{cm}^{-3}$). *Second and bottom panels:* The distribution of the gas density through the disk centre in the x (black line) and y (blue line) directions for selected time steps for model RS3.

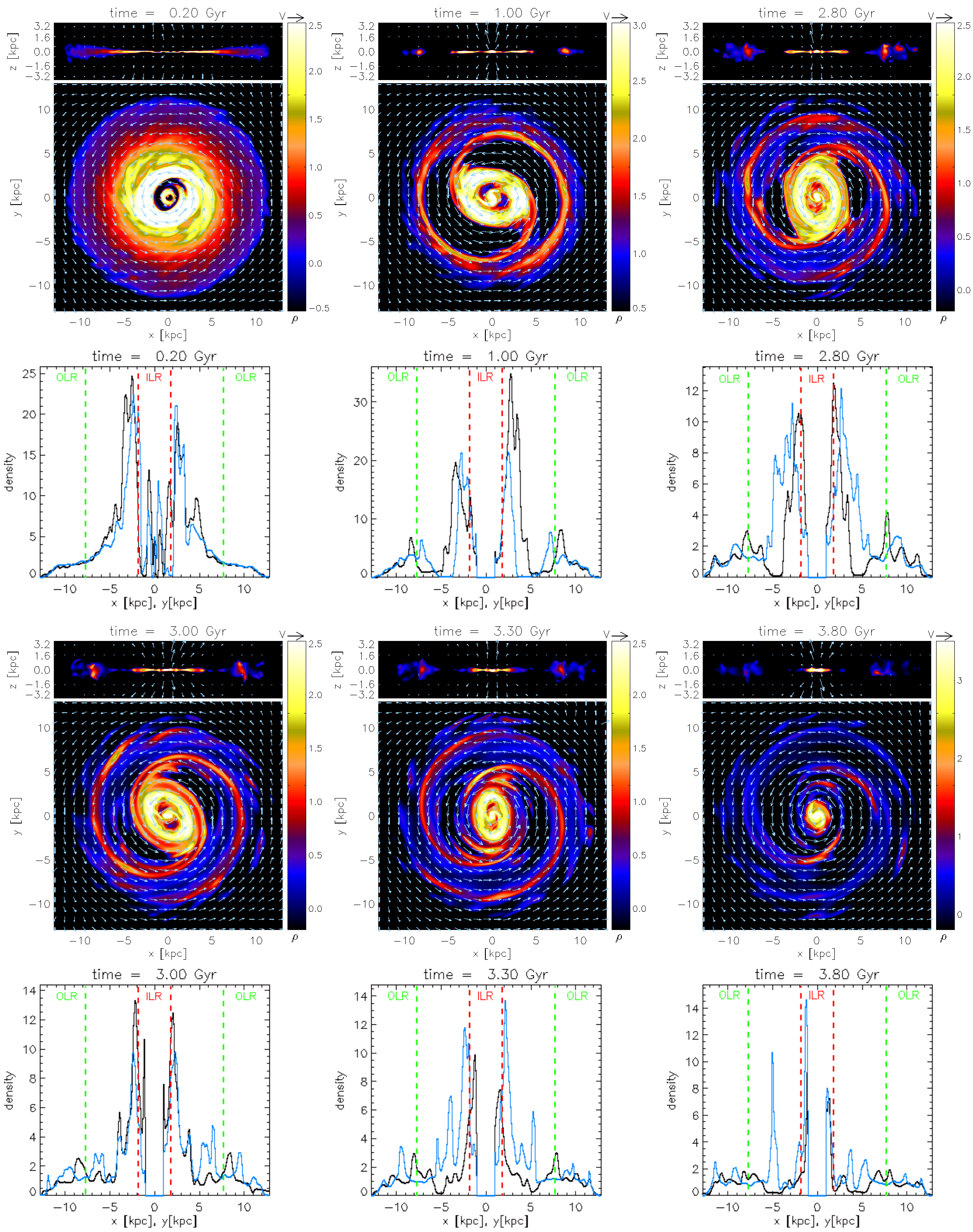

Figure 3.16: *Top and third panels:* The logarithm of the gas density and the gas velocity field (vectors) in vertical and horizontal slices through the disk centre for selected time steps for model RS4. The gas density is expressed in units of hydrogen atom per cubic centimeter ($1.0 n_H\,\mathrm{cm}^{-3}$). *Second and bottom panels:* The distribution of the gas density through the disk centre in the x (black line) and y (blue line) directions for selected time steps for model RS4.

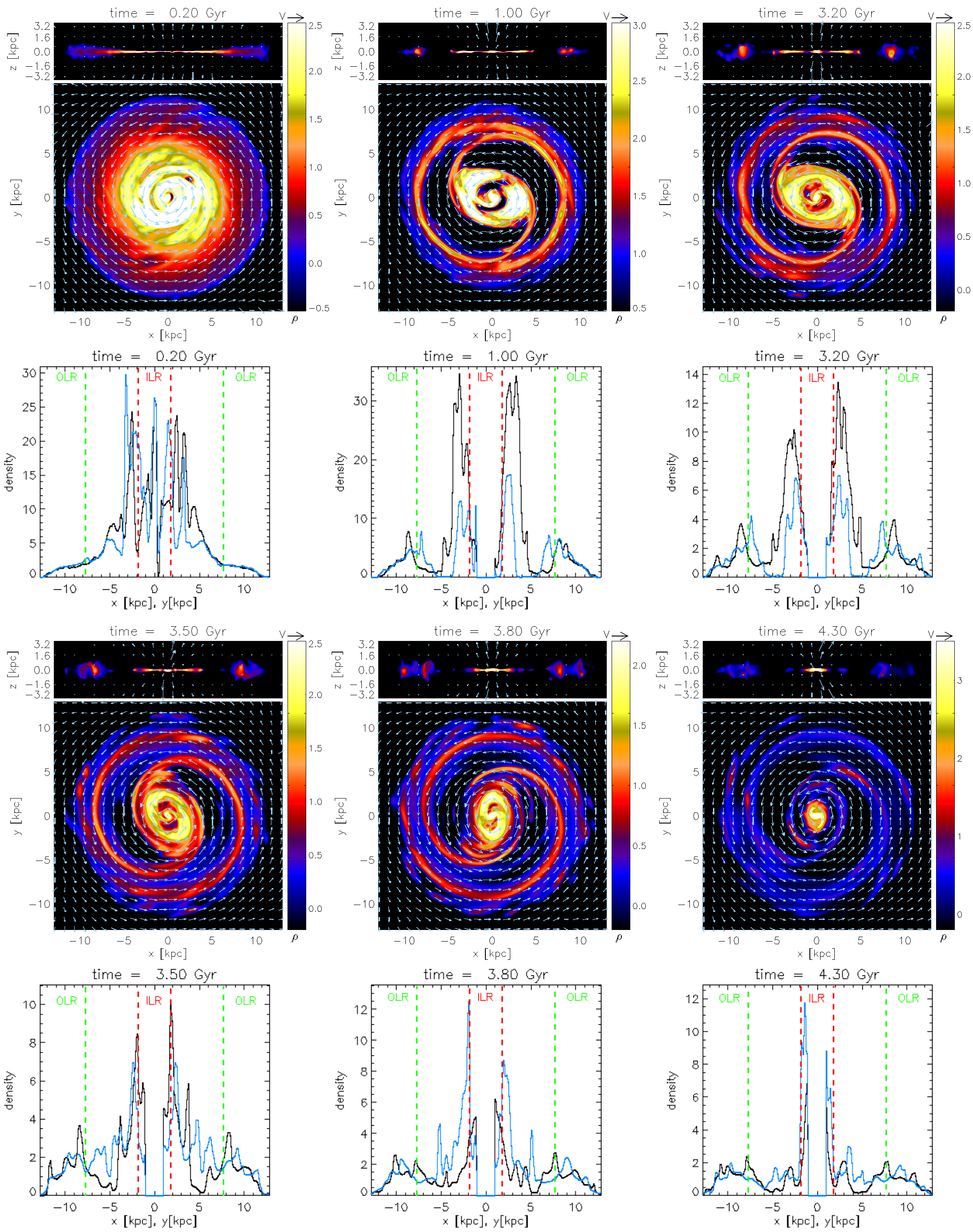

Figure 3.17: *Top and third panels:* The logarithm of the gas density and the gas velocity field (vectors) in vertical and horizontal slices through the disk centre for selected time steps for model RS5. The gas density is expressed in units of hydrogen atom per cubic centimeter ($1.0 n_H\,\mathrm{cm}^{-3}$). *Second and bottom panels:* The distribution of the gas density through the disk centre in the x (black line) and y (blue line) directions for selected time steps for model RS5.

introduced into the galaxy. As a result, nonaxisymmetrical gravitational potentials of the small bar and the oval disturb the initial configuration of the gas density in the galactic disk. Initially, the gas distribution looks very similar in all models of the ringed galaxy. Namely, in the region where the oval is present the intense accumulation of gas can be observed (see the time step $t = 0.2$ Gyr in top panel in Figures: 3.13, 3.14, 3.15, 3.16 and 3.17). The amount of gas collected in the oval region is similar in all models, which is visible for the time step $t = 0.2$ Gyr in second panel in Figures 3.13, 3.14, 3.15, 3.16 and 3.17.

When the bar and the oval reach their final masses (at time $t = 0.4$ Gyr) their influence on the gas distribution is very strong. The nonaxisymmetric gravitational potential of the oval triggers the formation of the outer spiral structure and the inner ring. On the other hand, the nonaxisymmetric gravitational potential of the small central bar supports the formation of the inner ring. It is also responsible for the presence of the inner spiral structure and gas accumulation in the inner part of the galaxy. The shape and evolution of these gaseous structures strictly depend on the SN activity.

At the time step $t = 1.0$ Gyr in all models the bar with the inner spiral structure, the inner ring, the outer spiral arms and the outer ring are visible (see top panel in Figures 3.13, 3.14, 3.15, 3.16 and 3.17). Moreover, between the oval and the outer ring the gap in gas density is present. Initially, in all models, the inner ring has an elongated shape and its thickness is about 2 kpc. It can be noticed from the time step $t = 1.0$ Gyr in second panel in Figures 3.13, 3.14, 3.15, 3.16 and 3.17 that, depending on the position, the inner ring extends from 1 kpc up to 3 kpc in y direction or from 2 kpc up to 4 kpc in x direction. The amount of mass accumulated in the inner ring is very similar in all models of the ringed galaxy, which can also be seen in the figures mentioned above. However, the shape of the outer spiral structure is not the same in different models and depends on the SN activity. Namely, for model RS1 (with the highest SN rate, $f_{SN} = 1/50\,\mathrm{yr}^{-1}$) the outer spiral arms are highly perturbed and form a very faint outer ring (see the time step $t = 1.0$ Gyr in top panel in Figure 3.13). For model RS2 ($f_{SN} = 1/100\,\mathrm{yr}^{-1}$) the outer spiral structure is less disturbed than that for model RS1, but the outer ring is still very faint. On the other hand, for models RS3 ($f_{SN} = 1/200\,\mathrm{yr}^{-1}$), RS4 ($f_{SN} = 1/300\,\mathrm{yr}^{-1}$) and RS5 ($f_{SN} = 1/500\,\mathrm{yr}^{-1}$) the outer spiral structure and the outer ring are coherent and clearly visible. The outer ring is formed as the result of tight winding of spiral arms and is obviously associated with the OLR which is located at $R = 7.7$ kpc. This is clearly visible e.g. for the time step $t = 1.0$ Gyr in second panel in Figure 3.14, where gaseous arms are well-defined. Moreover, the amount of gas accumulated in the OLR increases with the decreasing SN activity which can be seen at the time step $t = 1.0$ Gyr in second panel in Figures 3.13, 3.14, 3.15, 3.16 and 3.17.

As was mentioned above, gas is accumulated in the inner ring due to the combined action of the oval and the bar. In fact, negative torques drive the gas from the region between the CR and the OILR of the oval to the OILR, while positive torques between the galactic centre and the OILR of the oval cause the flow of the gas from this region to the OILR. Thus, as simulations proceed the inner ring becomes smaller and thinner. The final shape of the inner ring is very similar in all models, however the time evolution is not the same and differs in different models of the ringed galaxy. Namely, the period of time during which the inner ring changes its appearance and the amount of mass accumulated in the inner ring region are determined by the SN rate. For the highest SN activity (model RS1, $f_{SN} = 1/50\,\mathrm{yr}^{-1}$, Figure 3.13) the inner ring observed at the time step $t = 1.0$ Gyr becomes thinner, smaller and less elliptical in a very short period of time equal to 0.8 Gyr. At the time step $t = 1.8$ Gyr (third panel in Figure 3.13) the presented ring spans between $R = 1$ kpc and $R = 2$ kpc and its width is about 1 kpc (see the time step $t = 1.8$ Gyr in bottom row in Figure 3.13). The period of time during which the ring reaches its final shape grows with decreasing SN activity. In fact, for models SD2 ($f_{SN} = 1/100\,\mathrm{yr}^{-1}$), SD3 ($f_{SN} = 1/200\,\mathrm{yr}^{-1}$), SD4 ($f_{SN} = 1/300\,\mathrm{yr}^{-1}$) and SD5 ($f_{SN} = 1/500\,\mathrm{yr}^{-1}$) the mentioned time period is equal to 1.3 Gyr, 1.9 Gyr, 2.3 Gyr and 2.8 Gyr, respectively. Thus, the final ring is observed at time steps: $t = 2.3$ Gyr for model SD2 (third panel in Figure 3.14), $t = 2.9$ Gyr for model SD3 (third panel in Figure 3.15), $t = 3.3$ Gyr for model SD4 (third panel in Figure 3.16) and $t = 3.8$ Gyr for model SD5 (third panel in Figure 3.17). According to the previously mentioned time steps, the highest amount of gas in the inner ring is collected for model SD1 with the strongest SN activity, while the smallest for model SD5 with the lowest SN rate (compare bottom panels in Figures 3.13, 3.14, 3.15, 3.16 and 3.17). What is more, the final location of the inner ring corresponds to the position of the OILR which is equal to 1.8 kpc.

The inner ring is not observed during the whole simulation time. Shortly after the ring reaches its final mass, it starts to disappear. The last time step presented in third panel in Figures 3.13, 3.14, 3.15, 3.16 and 3.17 shows the appearance of the modeled ringed galaxy when the inner ring is no longer observed. The highest density region is indicated by the small bar and the inner spiral structure. Contrary to this, the outer ring is observed during the whole simulation time in all models. What is more, in all models the gas density is higher in the inner ring than in the outer faint ring (see e.g. all time steps in second and bottom panels in Figure 3.15).

Initially, in vertical slices, gas is mainly located in the galactic plane (see the time step $t = 0.2$ Gyr in vertical slices in Figures 3.13, 3.14, 3.15, 3.16 and 3.17). During the time evolution of the ringed galaxy gas is subsequently transferred from the galactic disk to the galactic halo by SNe explosions (see e.g., the time step $t = 2.8$ Gyr in Figure 3.16 or $t = 3.8$ Gyr in Figure 3.17). The configuration of velocity field vectors in vertical slices also indicates that the gas component outflows above and below the central part of the disk. The vertical wind produced by SNe remnants triggers mass outflow, which the averaged rate grows with increasing SN frequency (Table 3.4). The obtained values are: $3.4 M_\odot$ per year for model RS1 with the highest SN rate, $3.1 M_\odot$ per year for the RS2 model, $1.3 M_\odot$ per year for the RS3 model, $1.0 M_\odot$ per year for the RS4 model and $0.7 M_\odot$ per year for the RS5 model with the lowest SN activity.

The cosmic ray energy density distribution obtained for the ringed galaxy models is shown in Figure 3.18. In all models the cosmic ray energy density enhancements are visible in the same regions where the gas density is increasing (compare e.g. the time step $t = 2.3$ Gyr in bottom row in Figure 3.14 with the second plot in the top row in Figure 3.18). Thus, for models SD1, SD2, SD3, SD4 and SD5 only one time step with the cosmic ray energy density distribution is present. Selected time steps correspond to the evolution period when the inner ring reaches its final shape. As was mentioned above, the growth of the cosmic ray energy density is observed mainly in the high density regions. The cosmic ray gas is accumulated in the central part of the galaxy, where the bar is present. The inner ring and spiral arms are indicated by the enhancement of the cosmic ray energy density. For the model SD1 with the highest SN activity spiral arms are short and thick (first plot in the top row in Figure 3.18). Additionally, spiral arms become thinner and longer with the decreasing SN rate (compare e.g. model RS2 - second plot in the top row in Figure 3.18 with model RS5 - last plot in the bottom row in Figure 3.18).

3.2.2 Structure of the magnetic field

The distribution of the toroidal magnetic field component in vertical and horizontal slices through the disk centre is shown for models RS1, RS2, RS3, RS4 and RS5 in top and second panels in Figures 3.19, 3.20, 3.21, 3.22 and 3.23, respectively. Red colour represents regions with the positive toroidal magnetic field, blue with negative, while unmagnetized regions of the volume are shown in white. No magnetic field is present at the beginning of simulations and it is injected to the galactic disk using conditions described in Section 2.2.

In all models the evolution of the toroidal magnetic field component looks very similar in horizontal slices. In all cases the initial toroidal magnetic field is unordered and highly perturbed as it emerges from randomly oriented SNe explosions. This random configuration of the toroidal magnetic field component is well visible at the time step $t = 0.2$ Gyr in top row in Figures 3.19, 3.20, 3.21, 3.22 and 3.23. However, at the same time step in the central part of the galaxy small regions with ordered magnetic field can also be observed.

At the next time step, $t = 1.0$ Gyr, most of the volume of the ringed galaxy is occupied by the large scale magnetic field. In all models the well ordered toroidal magnetic field appears in the oval and spiral structure regions (see the time step $t = 1.0$ Gyr in top row in Figures 3.19, 3.20, 3.21, 3.22 and 3.23). The toroidal magnetic field component in the oval region is entirely negative for models RS2 (top row in Figure 3.20) and RS4 (top row in Figure 3.22), while for model RS3 (top row in Figure 3.21) it is completely positive. In the central part of the galaxy reversals of the magnetic field are visible for

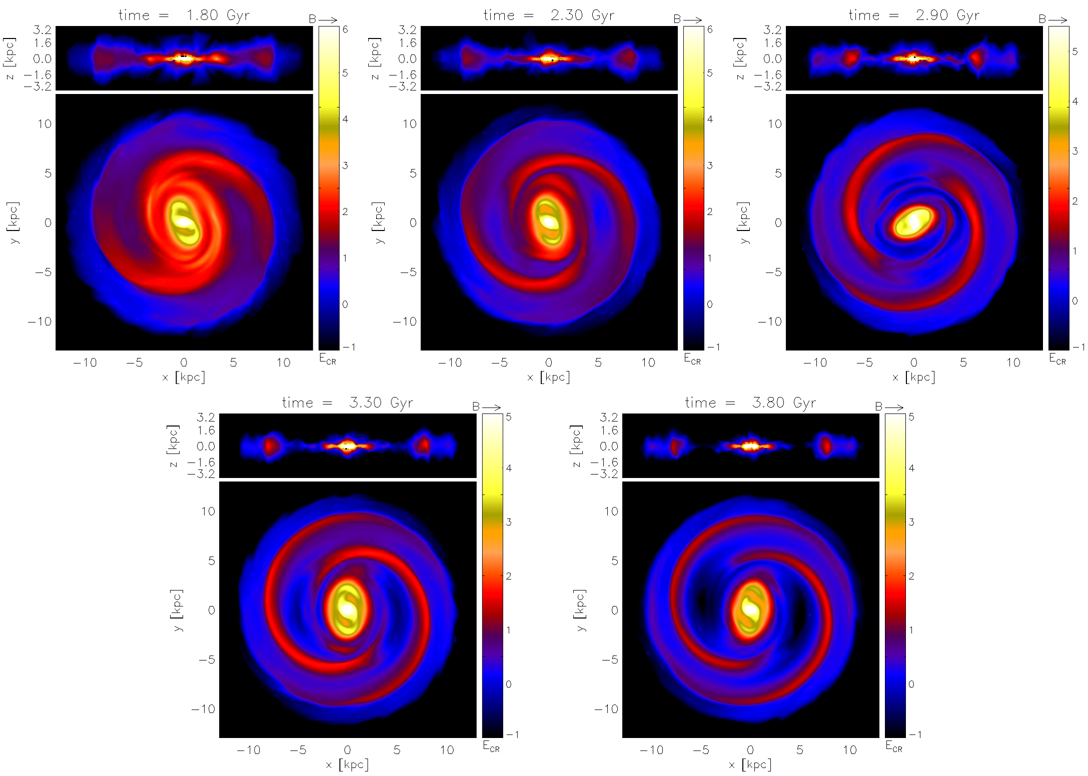

Figure 3.18: The logarithm of the cosmic ray energy density distribution in vertical and horizontal slices through the disk center for selected time steps for the ringed galaxy models RS1, RS2, RS3, RS4 and RS5. The selected time steps correspond to the period when the inner ring reaches its final shape, thus for the time step $t = 1.8$ Gyr, $t = 2.3$ Gyr, $t = 2.9$ Gyr, $t = 3.3$ Gyr and $t = 3.8$ Gyr for models RS1, RS2, RS3, RS4 and RS5, respectively. The cosmic ray energy density is expressed in units of electron volt per cubic centimeter eVcm^{-3}.

models RS1 (top row in Figure 3.19) and RS5 (top row Figure 3.23). The magnetic arms as well as reversals between the oval region and magnetic arms can be observed in all models. For models RS1 (top and second rows in Figure 3.20), RS2 (top and second rows in Figure 3.21), RS4 (top and second rows in Figure 3.22) and RS5 (top and second rows in Figure 3.23) the toroidal magnetic field component in magnetic arms is negative, whereas in reversals it is positive. On the other hand, for the model RS3 (top and second rows in Figure 3.22) the positive toroidal magnetic field component appears in magnetic arms, whereas in reversals it is negative.

As the simulations proceed the well ordered toroidal magnetic field is gradually observed at larger radii in the ringed galaxy. At time steps: $t = 1.6$ Gyr for model RS1 (top row in Figure 3.19), $t = 1.9$ Gyr for model RS2 (top row in Figure 3.20), $t = 2.5$ Gyr for model RS3 (top row in Figure 3.21), $t = 2.8$ Gyr for model RS4 (top row in Figure 3.22) and $t = 3.2$ Gyr for model RS5 (top row in Figure 3.23) magnetic arms merge and form the magnetic ring. The observed magnetic ring corresponds to the gaseous outer ring visible in polarization maps (compare e.g. the time step $t = 2.5$ Gyr in top and third rows in

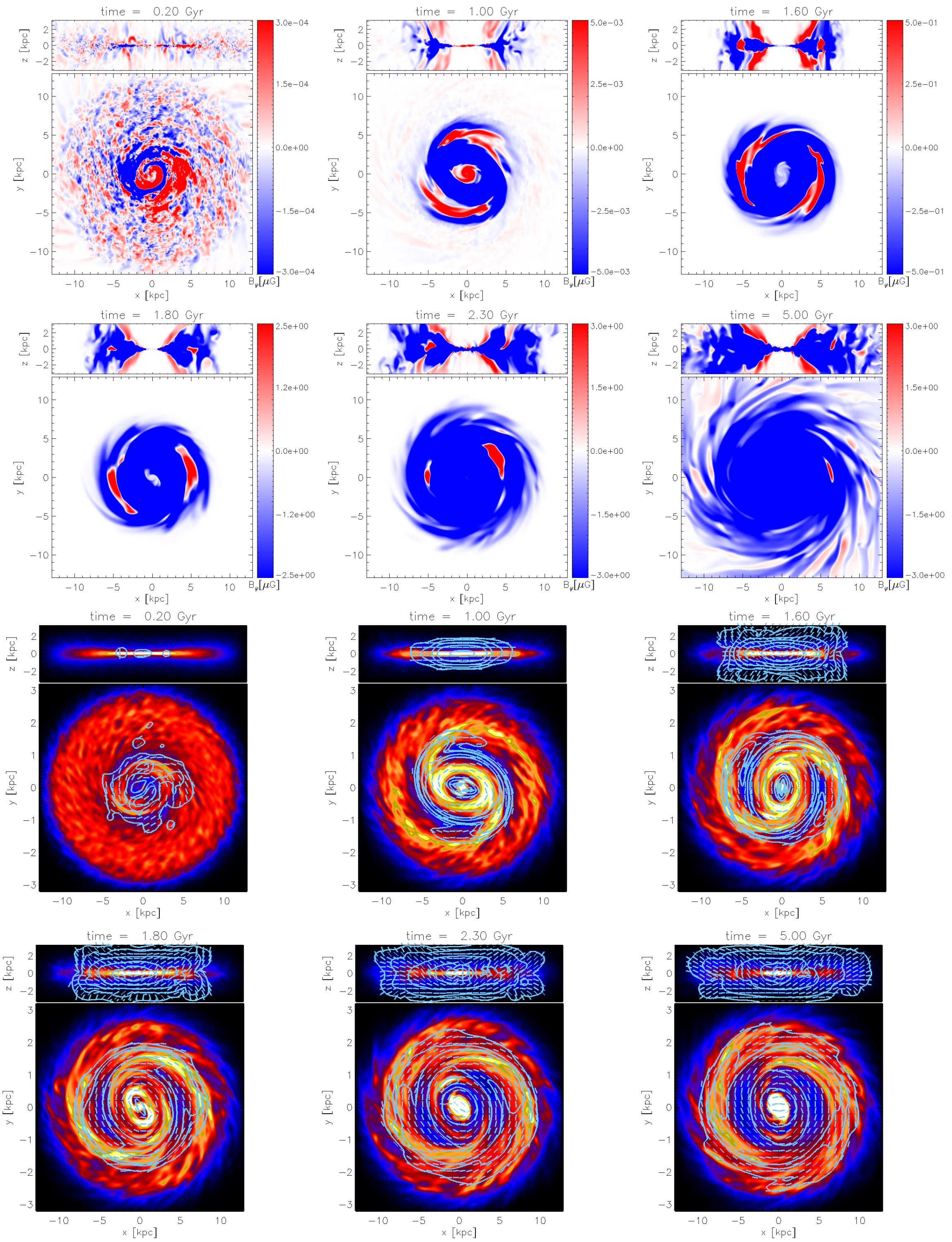

Figure 3.19: *Top panles:* The distribution of the toroidal magnetic field in vertical and horizontal slices through the disk centre for selected times steps for model RS1. Red colour represents regions with the positive toroidal magnetic field, blue with negative, while unmagnetized regions of the volume are white. To enhance weaker structures of the magnetic field in the outer galactic disk the colour scale in magnetic field maps is saturated. *Bottom panles:* Face-on and edge-on polarization maps at $\lambda = 6.2$ cm for selected times steps for the model RS1. Polarized intensity (contours) and polarization angles (dashes) are superimposed onto column density plots.

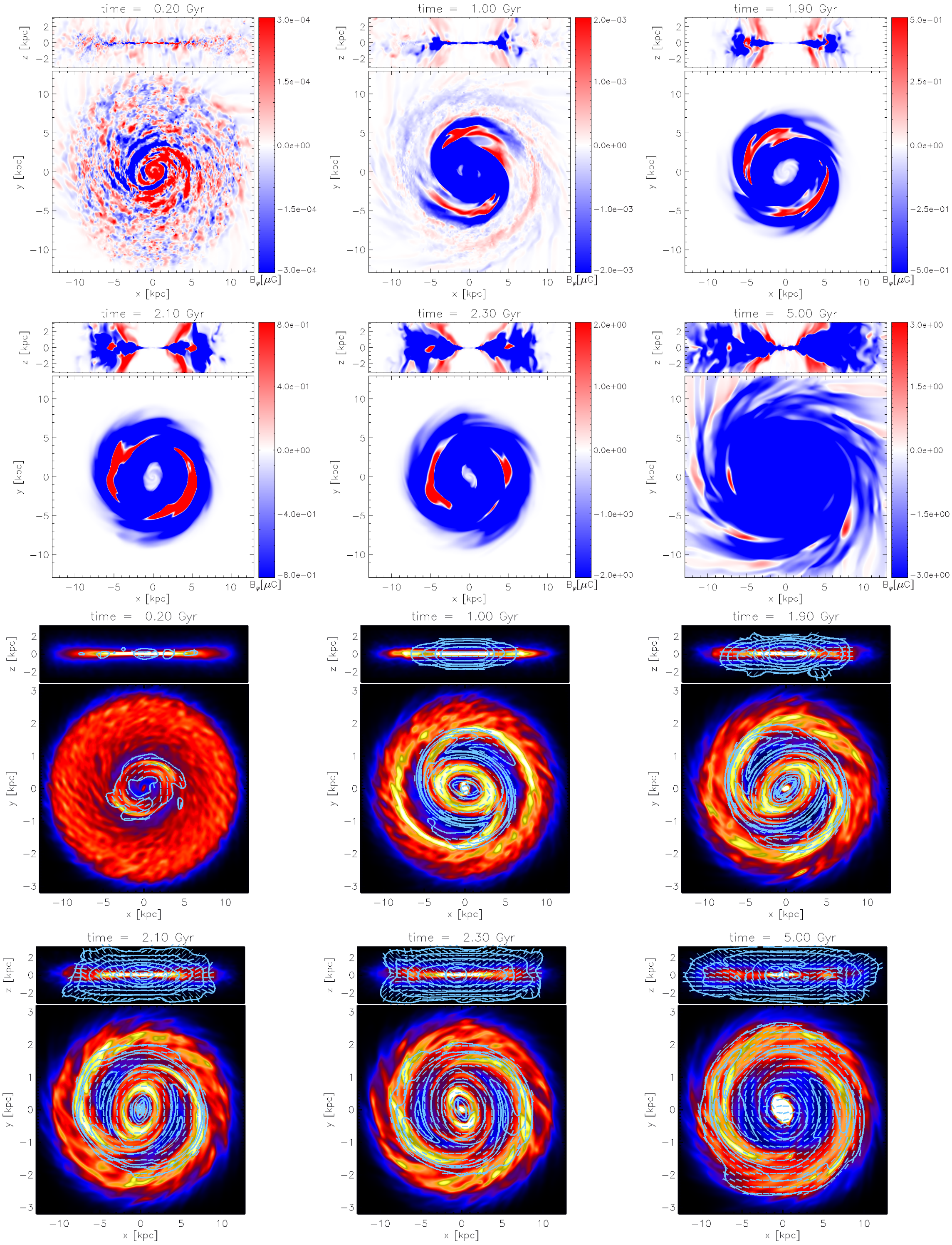

Figure 3.20: *Top panles:* The distribution of the toroidal magnetic field in vertical and horizontal slices through the disk centre for selected times steps for model RS2. Red colour represents regions with the positive toroidal magnetic field, blue with negative, while unmagnetized regions of the volume are white. To enhance weaker structures of the magnetic field in the outer galactic disk the colour scale in magnetic field maps is saturated. *Bottom panles:* Face-on and edge-on polarization maps at $\lambda = 6.2$ cm for selected times steps for the model RS2. Polarized intensity (contours) and polarization angles (dashes) are superimposed onto column density plots.

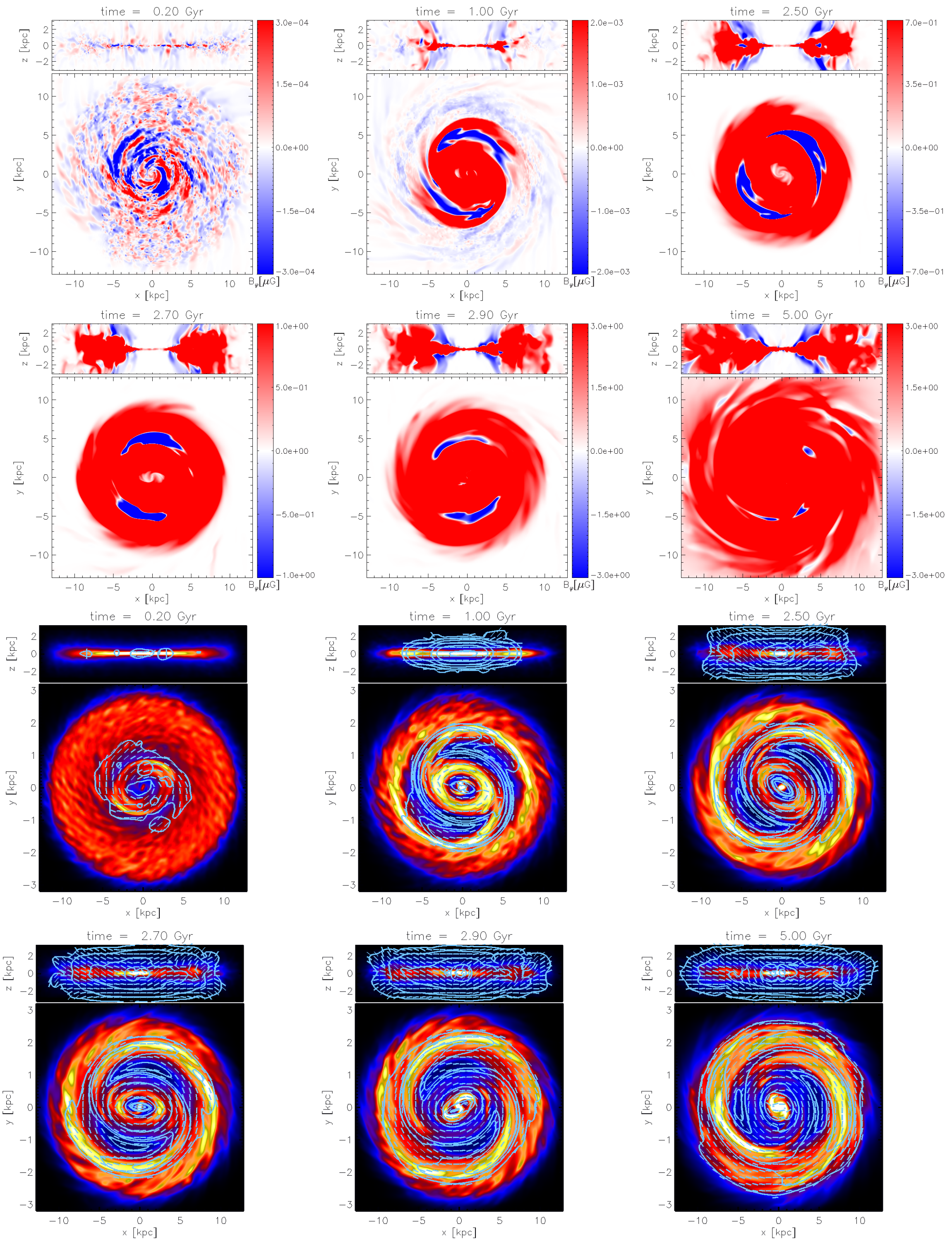

Figure 3.21: *Top panles:* The distribution of the toroidal magnetic field in vertical and horizontal slices through the disk centre for selected times steps for model RS3. Red colour represents regions with the positive toroidal magnetic field, blue with negative, while unmagnetized regions of the volume are white. To enhance weaker structures of the magnetic field in the outer galactic disk the colour scale in magnetic field maps is saturated. *Bottom panles:* Face-on and edge-on polarization maps at λ = 6.2 cm for selected times steps for the model RS3. Polarized intensity (contours) and polarization angles (dashes) are superimposed onto column density plots.

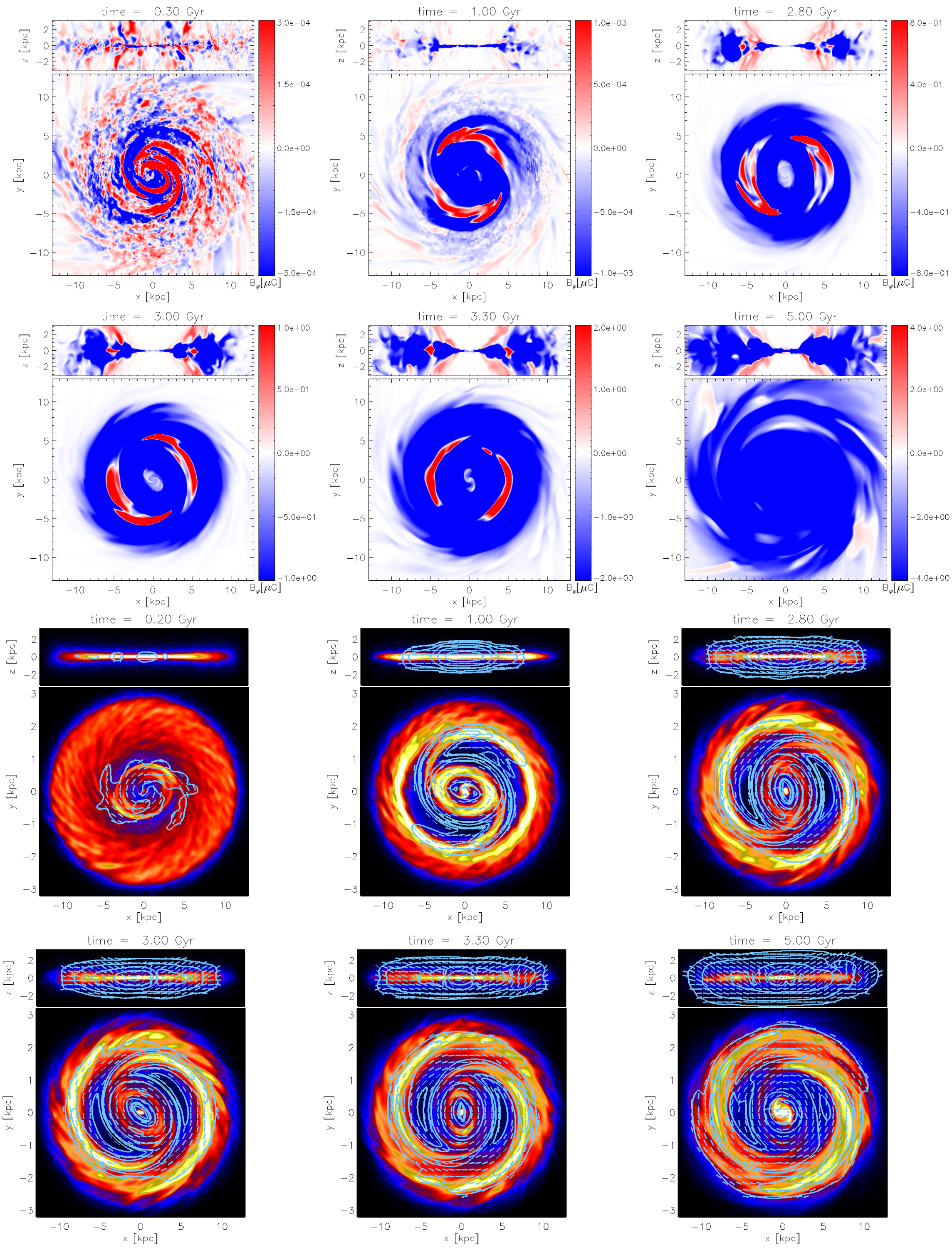

Figure 3.22: *Top panles:* The distribution of the toroidal magnetic field in vertical and horizontal slices through the disk centre for selected times steps for model RS4. Red colour represents regions with the positive toroidal magnetic field, blue with negative, while unmagnetized regions of the volume are white. To enhance weaker structures of the magnetic field in the outer galactic disk the colour scale in magnetic field maps is saturated. *Bottom panles:* Face-on and edge-on polarization maps at $\lambda = 6.2$ cm for selected times steps for the model RS4. Polarized intensity (contours) and polarization angles (dashes) are superimposed onto column density plots.

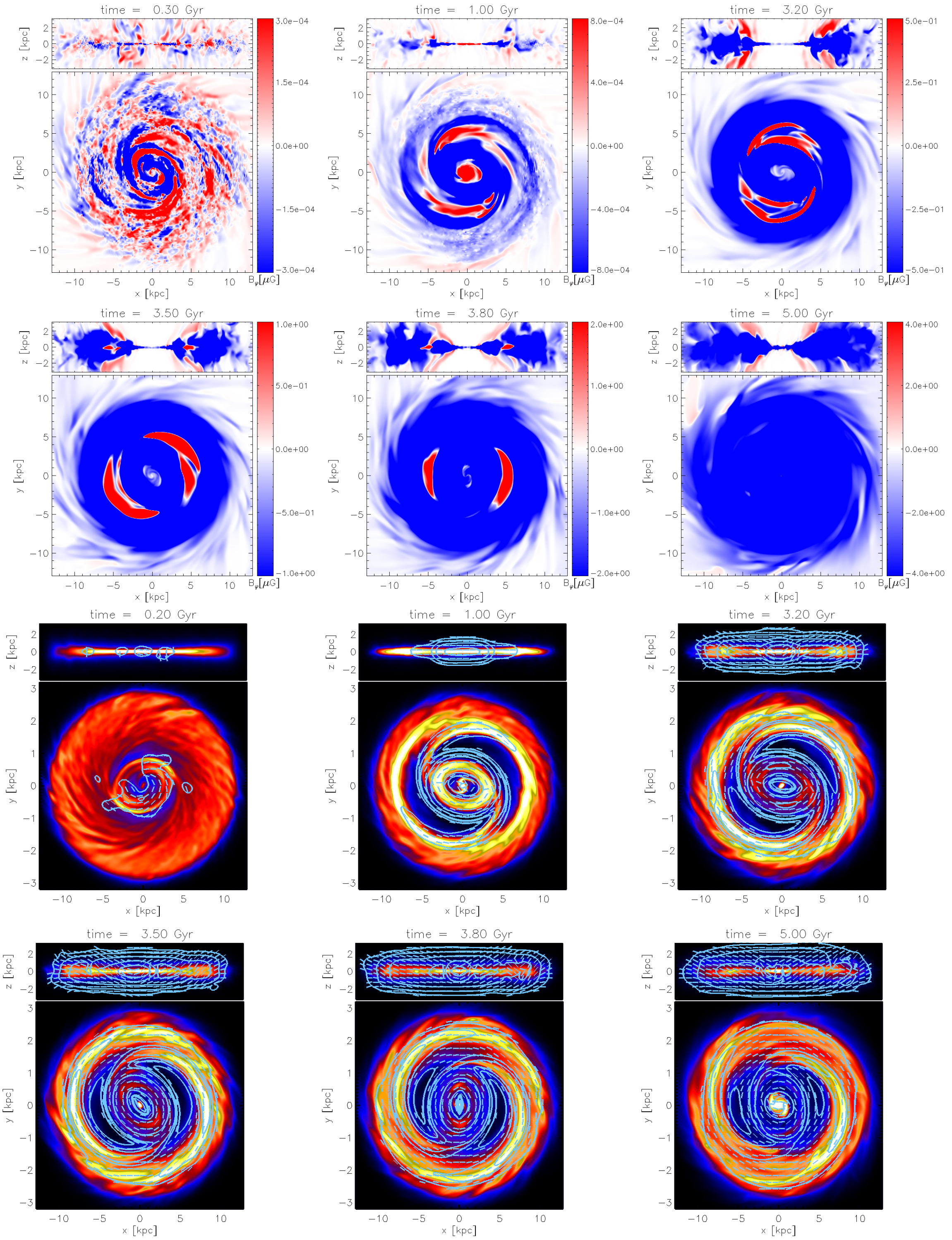

Figure 3.23: *Top panles:* The distribution of the toroidal magnetic field in vertical and horizontal slices through the disk centre for selected times steps for model RS5. Red colour represents regions with the positive toroidal magnetic field, blue with negative, while unmagnetized regions of the volume are white. To enhance weaker structures of the magnetic field in the outer galactic disk the colour scale in magnetic field maps is saturated. *Bottom panles:* Face-on and edge-on polarization maps at $\lambda = 6.2$ cm for selected times steps for the model RS5. Polarized intensity (contours) and polarization angles (dashes) are superimposed onto column density plots.

Figure 3.21 for model RS3 or the time step $t = 3.2$ Gyr in top and third rows in Figure 3.23 for the model RS5). Reversals in the central part of the galaxy, visible at the time step $t = 1.0$ Gyr in models RS1 (top row in Figure 3.19) and RS5 (top row in Figure 3.23), are no longer observed. However, in all models the nonaxisymmetrical gravitational potential of the bar causes that in the central part of the ringed galaxy the unmagnetized region, indicated by white colour, appears. On the other hand, reversals between the oval and magnetic arms are still visible in all models (see e.g. the time step $t = 2.5$ Gyr in top row in Figure 3.21).

During the further evolution of the magnetic field reversals between the oval region and the outer gaseous ring become smaller and finally almost disappear. This can be seen e.g. for model RS5 at the time step $t = 3.5$ Gyr (second row in Figure 3.23) when the magnetic reversals are roughly located in the gap with the lowest density (compare the time step $t = 3.5$ Gyr in second and third rows in Figure 3.23). At the next time step, $t = 3.8$ Gyr, magnetic reversals are smaller and at the last time step $t = 5.0$ Gyr they are completely invisible (see second row in Figure 3.23).

At the last time step $t = 5.0$ Gyr the large scale magnetic filed is observed in the whole volume of the ringed galaxy, even in the region where the gas density is very low (the area between the oval and the outer gaseous ring). Very small reversals are still present in models RS1 (second row in Figure 3.19), RS2 (second row in Figure 3.20) and RS3 (second row in Figure 3.21). In the case of models RS4 (second row in Figure 3.22) and RS5 (second row in Figure 3.23) no reversals are visible. The presence of the reversals in models RS1, RS2 and RS3 is probably caused by large amount of SNe explosions which very efficiently perturb the regular magnetic field in the galactic disk, which may result in reversal formation.

In vertical slices at the beginning of calculations the mainly randomly distributed toroidal magnetic field is present. An even (quadrupole-like) symmetry of the magnetic field with respect to the galactic plane appears in all models in the early stage of evolution (see vertical slices for the time step $t = 1.0$ Gyr in top row in Figures 3.19, 3.20, 3.21, 3.22 and 3.23) and is observed till the end of simulations (see vertical slices for the time step $t = 5.0$ Gyr in top row in Figures 3.19, 3.20, 3.21, 3.22 and 3.23). Additionally, in vertical slices magnetic field reversals are present during the whole simulation time. This reversals separate the unmagnetized region above and below the the central part of the galaxy and regions with the well ordered magnetic field in the outer part of the disk. This can be easily seen e.g. for the time step $t = 3.5$ Gyr for model RS5 (second row in Figure 3.23) or for the time step $t = 5.0$ Gyr for model RS2 (second row in Figure 3.20). Moreover, small reversals in vertical slices also appear from time to time in the outer part of the galactic disk (e.g. the time step $t = 5.0$ Gyr for model RS1, second row in Figure 3.19).

3.2.3 Polarization maps and pitch angles

In third and bottom panels in Figures 3.19, 3.20, 3.21, 3.22 and 3.23 I present the magnetic field evolution as seen in radio polarymetry. Polarization maps show the distribution of the polarization angle and polarized intensity superimposed onto the column density. All face-on and edge-on polarization maps have been smoothed down to the resolution of 40″. Black colour represents regions with the lowest density and yellow the ones with the highest density. The chosen time steps are the same as those selected for the toroidal magnetic field (top and second rows in Figures 3.19, 3.20, 3.21, 3.22 and 3.23) and gas density distribution (Figures 3.13, 3.14, 3.15, 3.16 and 3.17). Comparing the column density presented in vertical and horizontal slices in third and bottom panels in Figures 3.19, 3.20, 3.21, 3.22 and 3.23 with the gas density through the disk centre in vertical and horizontal slices in Figures 3.13, 3.14, 3.15, 3.16 and 3.17 one can notice significant differences. First of all, in the case of third and bottom rows in Figures 3.19, 3.20, 3.21, 3.22 and 3.23, where the column density is shown, outer spiral structures form thick and well defined outer rings, which extend between $R \sim 8\,\mathrm{kpc}$ and $R \sim 11\,\mathrm{kpc}$. These outer rings are significantly less visible in Figures 3.13, 3.14, 3.15, 3.16 and 3.17, where the gas density distribution through the disk centre is plotted. The distinction described above is visible by comparing e.g. the time step $t = 3.3\,\mathrm{Gyr}$ in Figure 3.16 and in bottom panel in Figure 3.22. What is more, for model SD5 (model with the lowest SN rate, $f_{SN} = 1/500\,\mathrm{yr}^{-1}$) the inner ring is very faint in the column density but is well defined in the case of the gas density distribution through the disk center (compare e.g. the time step $t = 3.8\,\mathrm{Gyr}$ in Figure 3.17 and in bottom row in Figure 3.23). Similarly, in the case of model RS4 ($f_{SN} = 1/300\,\mathrm{yr}^{-1}$) the inner ring in the column density (Figure 3.22) is less visible than this observed for the same model in the gas density distribution through the disk centre (Figure 3.16). For the other models, RS1 $f_{SN} = 1/50\,\mathrm{yr}^{-1}$, RS2 $f_{SN} = 1/100\,\mathrm{yr}^{-1}$ and RS3 $f_{SN} = 1/200\,\mathrm{yr}^{-1}$, with a high SN activity, the inner ring is well defined both in the column density plots and in the gas density distribution through the disk center.

Polarization maps in third and bottom panels in Figures 3.19, 3.20, 3.21, 3.22 and 3.23 show that magnetic field maxima at first appear in the central part of the galaxy (see the time step $t = 0.2\,\mathrm{Gyr}$). At the next time step $t = 1.0\,\mathrm{Gyr}$ the magnetic field maxima correspond to the gas density enhancements, where SNe explosions are located. Indeed, the magnetic field is present in gaseous arms as well as in the oval region. Additionally, for models RS1, RS2, RS3 and RS4 the regular magnetic field is also observed in the interarm region (see the time step $t = 1.0\,\mathrm{Gyr}$ in third panel in Figures 3.19, 3.20, 3.21 and 3.22, respectively). For model RS5 (with the lowest SN activity) no regular magnetic field is observed in the zone between the oval and gaseous arms. (Figure 3.23). For the further time steps the drift of magnetic arms into the interarm region is no longer visible in models RS1, RS2, RS3 and RS4. Instead, in the area between the oval and gaseous arms, regions with vanishing polarized intensity are observed. These zones correspond to areas where magnetic reversals are present (compare e.g. the time step $t = 2.1$ Gyr for model RS2 in second and bottom rows in Figure 3.20 or the time step $t = 3.3$ Gyr for model RS4 in second and bottom rows in Figure 3.22). As simulations proceed, the polarized emission gradually occupies the largest volume of the ringed galaxy and finally in the whole galactic disk the polarized intensity is observed (see e.g. the time step $t = 5.0$ Gyr in bottom row in Figure 3.19).

Polarization vectors in face-on maps in third and bottom panels in Figures 3.19, 3.20, 3.21, 3.22 and 3.23 indicate the mean magnetic field direction and reveal a regular spiral structure. Polarization vectors are rather aligned along the gaseous structures, e.g. they follow the gas distribution in the inner ring. Additionally, the estimated mean pitch angle (averaged over azimuthal angle and radius in the galaxy's plane) changes slightly during the evolution of the ringed galaxy and depending on model ranges between $-6°$ and $-13°$.

Edge-on polarization maps for models RS1, RS2, RS3, RS4 and RS5 are shown in third and bottom rows in Figures 3.19, 3.20, 3.21, 3.22 and 3.23, respectively. In all models in vertical slices the extended structures of polarization vectors are present. At the time step $t = 1.0$ Gyr (third row in Figures 3.19, 3.20, 3.21, 3.22 and 3.23) the magnetic field in the disk plane is mainly parallel to the disk, while the vertical magnetic field component can be seen in the halo. However, at later time steps the magnetic field in the disk plane is no longer parallel to the galactic disk. Indeed, the configuration of the magnetic field changes very rapidly and the magnetic field vectors are highly inclined with respect to the galactic disk (see e.g. the time step $t = 2.3$ Gyr in bottom row in Figure 3.19 or the time step $t = 3.3$ Gyr in bottom row in Figure 3.22). The most extended structures are apparent at the last time step of the calculation (see the time step $t = 5.0$ Gyr in bottom row in Figures 3.19, 3.20, 3.21, 3.22 and 3.23).

3.2.4 Amplification and strength of the magnetic field

In Figure 3.24 I present the exponential growth of the total magnetic energy (top panel) and the azimuthal flux (bottom panel) for all models of the ringed galaxy. As in the case of the barred galaxy the initial growth of the magnetic field (visible at the time step $t = 0.1$ Gyr, top panel in Figure 3.24) is caused by fast accumulation of the magnetic energy generated by injected dipoles. After the time step $t = 0.1$ Gyr the magnetic field in all models increases only due to the dynamo action. It is apparent that in the case of the ringed galaxy the rate of the amplification of the total magnetic field depends on the SN activity. Thus, the magnetic field reaches equipartition approximately at time steps $t \sim 1.9$ Gyr, $t \sim 2.3$ Gyr, $t \sim 2.9$ Gyr, $t \sim 3.5$ Gyr and $t \sim 4.0$ Gyr for RS1, RS2, RS3, RS4 and RS5 models, respectively (see top panel in Figure 3.24). The obtained equipartition times correspond to moments when the inner ring reaches its final shape (compare e.g.

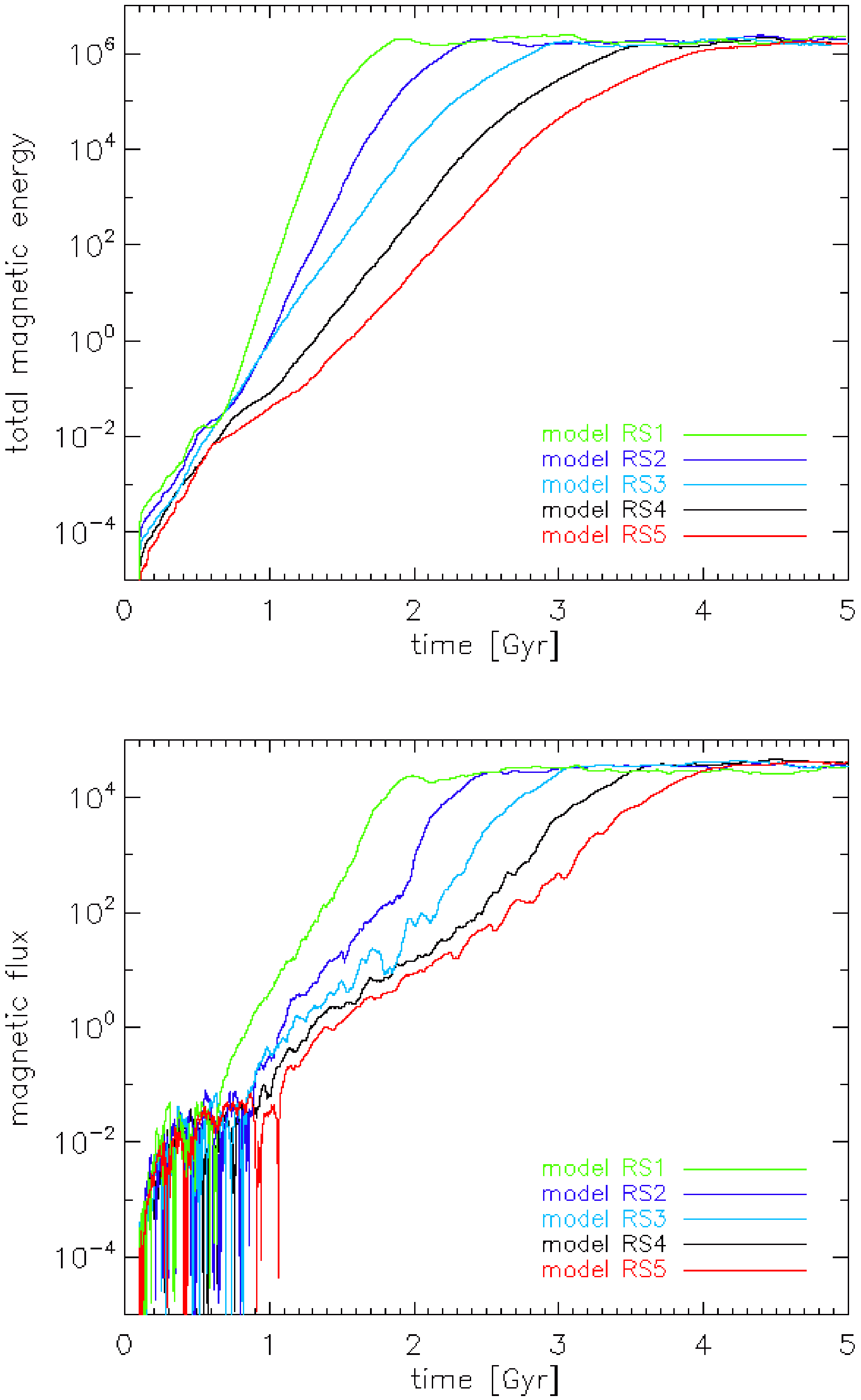

Figure 3.24: The time evolution of the total magnetic energy B^2 (top panel) and the mean azimuthal flux B_ϕ (bottom panel) for different values of the SN frequency f_{SN} in the simulation series RS. The colour curves represent respectively cases of $f_{SN} = 1/50\,\mathrm{yr}^{-1}$ (RS1), $f_{SN} = 1/100\,\mathrm{yr}^{-1}$ (RS2), $f_{SN} = 1/200\,\mathrm{yr}^{-1}$ (RS3), $f_{SN} = 1/300\,\mathrm{yr}^{-1}$ (RS4) , $f_{SN} = 1/500\,\mathrm{yr}^{-1}$ (RS5).

Model	f_{SN} [yr^{-1}]	τ [Myr]	M_{lost} [$M_{\odot}\,yr^{-1}$]	max B_{φ}^{ir} [μG]	i max B_{φ}^{od} [μG]	B_{mean} [μG]	$-p$ [°]
RS1	1/50	104	3.4	33.1	10.1	13.8	12 – 13
RS2	1/100	133	3.1	28.7	10.0	14.4	10 – 11
RS3	1/200	164	1.3	32.9	11.3	14.2	9 – 10
RS4	1/300	196	1.0	20.3	10.9	14.6	7 – 8
RS5	1/500	230	0.7	17.0	11.6	14.5	6 – 7

Table 3.4: Overview of the obtained parameters characterizing RS models. Subsequent columns show: the model name, the SN frequency f_{SN}, the e-folding time τ, the rate of the mass outflow M_{lost}, the maximum magnetic field in the inner ring max B_{φ}^{ir} and in outer disk (outside the oval) max B_{φ}^{od}, the mean magnetic field B_{mean} (equipartition state) and pitch angles p.

the time step $t = 2.3$ Gyr in Figure 3.14 and the dark blue line in top panel in Figure 3.24). Additionally, during the equipartition state the cosmic ray driven dynamo maintains the magnetic field in a steady state.

The cosmic ray driven dynamo action in the ringed galaxy also influences the amplification of the azimuthal magnetic flux component (Figure 3.24, bottom panel). The regular magnetic field grows up on an average e-folding time of $t = 104$ Myr, $t = 133$ Myr, $t = 164$ Myr, $t = 196$ Myr and $t = 230$ Myr for RS1, RS2, RS3, RS4 and RS5 models, respectively (see Table 3.4). At the beginning of all simulations, especially from $t = 0.1$ Gyr to $t = 1.0$ Gyr (Figure 3.24, bottom panel), the magnetic flux rapidly changes sign and its absolute value differentiates randomly around the exponential curve. The observed variation is probably caused by the random magnetic field which evolves into large scale magnetic structures with odd symmetry with respect to the galactic plane. After the time step $t \sim 1.0$ Gyr the total azimuthal flux almost stops to reverse which corresponds to the well developed regular magnetic field structures (compare e.g., the time step $t = 2.5$ Gyr in top row in Figure 3.21 with the blue line in bottom panel in Figure 3.24). Small variations of the total azimuthal flux correspond to reversals which appear in the toroidal magnetic field distribution in different time steps in Figures 3.19, 3.20, 3.21, 3.22 and 3.23. Moreover, the final saturation levels of the magnetic flux are the same as in the case of the total magnetic energy (compare top and bottom panels in Figure 3.24).

In fourth, fifth and sixth column in Table 3.4 I present the value of the maximum magnetic field in the inner ring B_{φ}^{ir} and in the outer disk (outside the oval) B_{φ}^{od} as well as the mean magnetic field B_{mean}, respectively. All above values are calculated at the time step when the inner ring reaches its final shape and the magnetic field attains the equipartition. As was mentioned above, this time step differs among models and is equal to: $t = 1.8$ Gyr for model RS1, $t = 2.3$ Gyr for model RS2, $t = 2.9$ Gyr for model RS3, $t = 3.3$ Gyr for model RS4 and $t = 3.8$ Gyr for model RS5. The mean magnetic field as well as the maximum value of the toroidal magnetic field in the outer disk (outside the oval region) are very similar in all models of the ringed galaxy. According to Table 3.4 the mean magnetic field varies between $10.0\,\mu$G and $11.6\,\mu$G while maximum value of B_{φ}^{od} ranges from $13.8\,\mu$G up to $14.6\,\mu$G. On the other hand, the maximum value of the magnetic field in the inner ring depends on the SN activity. Indeed, the highest value of the B_{φ}^{ir} is equal to $33.1\,\mu$G and is obtained for model RS1 (with the strongest SN activity) while the lowest value $17.0\,\mu$G is obtained for model RS5 (with the lowest SN rate) (compare rows in fourth column in Table 3.4).

Chapter 4

Discussion

In the previous section I have shown that the cosmic ray driven dynamo can amplify a weak magnetic field seeded by small scale magnetic dipoles introduced through SNe explosions. Having included a cosmic ray gas supplied in SNe remnants, the cosmic ray driven dynamo triggers an exponential growth of the magnetic field up to a few μG within few Gyr in barred and ringed galaxies. As a result of the dynamo action, large scale magnetic fields develop in the galactic disk and in the surrounding galactic halo. Results obtained in simulations described in this thesis can be compared with observations as well as with previous numerical studies.

4.1 Barred galaxies - relation to observations and other works

The most important part of this thesis is a comparison of the obtained magnetic field configuration with observations of real galaxies. In most of models the regular magnetic field shows the ASS symmetry. A clear ASS mode has been also found in real galaxies M31 (Sofue &Takano 1981) and IC342 (Krause et al. 1989). Model BD1 ($f_{SN} = 1/100\,\mathrm{yr}^{-1}$) seems to have a superposition of different modes (Figure 3.10). The dominance of ASS field configuration can be seen at the time step $t = 3.75$ Gyr, whereas of BSS mode at the time step $t = 6.0$ Gyr. A mixture of magnetic modes is observed in most of real spiral galaxies. However, the overbearing dominance of the ASS symmetry in presented numerical models is not surprising as the axisymmetric mode can be excited most easily by dynamo action (Krause 2003). To better reproduce complex configurations of magnetic fields observed in real galaxies more physical processes occurring in the ISM should be taken into account.

The edge-on distribution of the toroidal magnetic field is displayed in the first two rows in Figures 3.9, 3.10, 3.11 and in Figure 3.5. In models SD1, SD2, SD4 and SD5 the toroidal magnetic field component has the same direction above and below the galactic disk. This configuration corresponds to the even (quadrupole-type) symmetry of magnetic fields in galaxies. It is believed that the even symmetry should exist in most of spiral galaxies. This conjecture was supported by many theoretical studies (e.g. Ruzmaikin et al. 1988) and by most of observational evidence (e.g. Beck 2009c; Heesen et al. 2009) as well as by a number of numerical investigations (e.g. Brandenburg et al. 1993). The quadrupole-like symmetry was also obtained by Hanasz et al. (2009b) who studied the cosmic ray driven dynamo in normal spiral galaxies.

Results presented in this thesis confirm that the cosmic ray driven dynamo can also produce the odd symmetries of magnetic fields in barred galaxies. In the case of model SD1 the toroidal magnetic field component has different direction above and below the disk plane, what reveals the odd (dipole-type) configuration of the magnetic field with respect to the galactic plane. Following Moss et al. (2010) the odd symmetry of the magnetic field in galaxies can also be explained by the dynamo theory.

Several researches have studied numerically the evolution of the magnetic field in barred galaxies without the inclusion of the dynamo action. Otmianowska-Mazur et al. (1997, 2002) made N-body simulations and found that the magnetic field is weak in the bar region and concentrates in spiral arms in the interarm space. They also proposed the mechanism responsible for detaching of magnetic arms from the gaseous spiral and their drift into the interarm region. Namely, magnetic arms drift into the interarm space due to the difference between the pattern speed of the bar (together with gaseous arms) and the rotation speed of the disk. This process repeats a few times during galactic life. Similar results were obtained in 3D non-linear MHD numerical simulations taking into account back-reaction of the magnetic field to gas (Kulesza-Żydzik et al. 2009, 2010). Results presented in this thesis show that magnetic arms between gaseous spiral and the bar are observed in most of the barred galaxy simulations (see third and bottom rows in Figures 3.9, 3.10, 3.11 and in Figure 3.5). The drift of magnetic arms is caused by the same mechanism as was proposed by Otmianowska-Mazur et al. (2002) and Kulesza-Żydzik et al. (2009, 2010). However, in my simulations magnetic arms are continuously present in the interarm region, while in the work done by Otmianowska-Mazur et al. (2002) and Kulesza-Żydzik et al. (2009, 2010) magnetic arms appear periodically between the gaseous spiral and the bar. This distinction is probably due to the cosmic ray driven dynamo action, which continuously supplies random magnetic field in gaseous arms through SNe explosions. This field is constantly being transformed into a regular field and observed as magnetic spiral in the interarm area. Only in one model, BS1, no magnetic arms can be identified in gaseous arms or in the interarm area (third and bottom rows in Figure 3.8). The lack of magnetic arms can be caused by the very strong star formation rate ($f_{SN} = 1/25\,\mathrm{yr}^{-1}$) applied in this model. If SNe explosions continuously and violently generate random magnetic field, physical processes occurring in the outer part of the galaxy are too slow to transform it into a regular field. In that case the polarized magnetic field is visible only in the bar region. Results obtained for model SD1 resemble the observed radio polarization structure which is visible in barred galaxies, e.g. in NGC 986 (Beck et al. 2002). In this barred galaxy the polarized emission is observed only in the inner bar. What is more, following Kohno et al. (2008) the star formation rate in NGC 986 is high and could still be in a growing phase.

Moss et al. (1998, 1999, 2001, 2007) analyzed the role of the mean-field dynamo theory in generation and maintenance of the large-scale magnetic fields in barred galaxies. Moreover, they prepared global polarization maps in order to compare them directly with radio observations of NGC 1365. Although the whole range of input parameters was studied, none of them gave configuration of vectors of the polarization similar to the observed one. Contrary to their work, the calculated synthetic face-on polarization maps of barred galaxies presented in this thesis bear some resemblance to observations. The obtained results can be compared directly with observations of NGC 1365 and NGC 1097 (Beck et al. 2005), as these galaxies show roughly similar magnetic structures. Although, the modelled barred galaxy possesses different properties, e.g. it is much smaller than NGC 1365 or NGC 1097, the following similarities can be highlighted:

- The polarized radio emission is strongest in the inner part of the bar and in radio ridges that approximately follow the dust lanes indicated by the enhancement of the gas density (see e.g. time step $t = 2.5$ Gyr in Figure 3.5). The enhancement of the polarized intensity in the radio ridges may be caused by compression of random fields in shocks.

- Magnetic field vectors change quickly their pitch angles whenever they are located upstream to the dust lanes. This is visible almost at every time step in each simulation. In a real observation strong changes of magnetic field orientation results in depolarization valley within the telescope beam. In the case of synthetic polarization maps this effect is almost invisible. Small depolarization valley appears very rarely and an example of one is visible e.g. at the time step $t = 4.25$ Gyr in the bottom row in Figure 3.10.

- In the outer part of the disk magnetic vectors form a spiral pattern with maxima of polarized intensity along spiral gaseous arms and in interarm regions (see third and bottom rows in Figures 3.9, 3.10, 3.11 and in Figure 3.5).

- The total magnetic field reaches maximum values in the central part of the galaxy and depending on a model it ranges between $53.4\,\mu$G and $88.8\,\mu$G (see Table 3.1). The obtained values are very similar to those observed in real galaxies, e.g. in NGC 1365 the total magnetic field in the central region is about $60\,\mu$G.

- In spiral arms the maximum value of the total magnetic field taken from simulations ranges between 2.1 μG and 8.6 μG (see Table 3.2). These values are slightly smaller than those obtained from observations, where the total magnetic field in arms is about 20 μG. This distinction may be caused by differences in sizes of modelled and real galaxies. As mentioned above, the modelled barred galaxies are much smaller than NGC 1365 or NGC 1097. Thus, gaseous arms and corresponding magnetic arms in NGC 1365 and NGC 1097 are stronger than those obtained in numerical simulations.

- The average equipartition strength in modelled barred galaxies is between 3.7 μG and 12.1 μG (see Table 3.3). For comparison, the average total magnetic field strength for the sample of 20 barred galaxies is 10 ± 0.3 μG (Beck et al. 2002).

Polarization vectors in the edge-on view reveal the so-called X-shaped structure. It appears in the modelled galaxy as a result of buoyancy driven by cosmic rays via the PI. The galactic wind emerging from the disk is modified by the differential rotation in the halo and by the dynamo action. It is responsible for the transport of the magnetic field together with the cosmic ray gas to the galactic halo. The X-shaped configuration of the magnetic field is observed in radio-continuum emission at centimeter wavelengths of edge-on spiral galaxies (Tüllmann et al. 2000; Soida 2005; Krause et al. 2006). Edge-on synthetic radio maps obtained in this thesis bear some resemblance to radio maps of edge-on galaxies NGC 5775 (Soida 2005) or NGC 253 (Heesen et al. 2009). In both in synthetic and real maps the orientation of the magnetic field vectors is parallel in the disk and at small distances from the galactic midplane. On the other hand, the vertical field component becomes important with increasing radius and height above and below the galactic plane. Similar results were obtained by Hanasz et al. (2009b) and Otmianowska-Mazur et al. (2009). They claimed that using the cosmic ray driven dynamo the X-type structures can be successfully reproduced in spiral galaxies. Simulations presented in this thesis confirm this finding and extend it to barred and ringed (see Section 4.2) galaxies.

Edge-on spiral galaxies with very high (e.g. NGC 4666) and much smaller (e.g. NGC 4217) star formation rate possess very similar X-shaped configuration of the magnetic field. Contrary to this, synthetic edge-on polarization maps obtained for model BS1 with the highest SN activity differ from those calculated for other models with lower SN rates. For models BS2 ($f_{SN} = 1/50\,\mathrm{yr}^{-1}$) , BS3 ($f_{SN} = 1/100\,\mathrm{yr}^{-1}$), BS4 ($f_{SN} = 1/200\,\mathrm{yr}^{-1}$) and BS5 ($f_{SN} = 1/500\,\mathrm{yr}^{-1}$) the vertical magnetic field component occurs at large galactic radii, while for model BS1 ($f_{SN} = 1/25\,\mathrm{yr}^{-1}$) it is present only in the bar region.

The X-shaped magnetic field configuration in a starburst galaxy NGC 4631 is slightly different from those observed in galaxies mentioned above. In fact, magnetic vectors cross the disk plane at almost right angle. Soida (2005) suggested that this behaviour of B-vectors may indicate the dipolar symmetry of the magnetic field. However, in my simulations the X-shaped structures produced in the case of the dipolar and quadrupolar symmetry are very similar. No significant differences can be noted, thus the magnetic field configuration visible in edge-on maps of NGC 4631 may result from some physical processes occurring in the galactic disk rather than from the symmetry of the magnetic field.

In the barred galaxy simulations no significant dependence of the growth rate on the SN frequency can be observed. For models SD1, SD2, SD3, SD4 and SD5 the large scale magnetic field grows on timescales 230 Myr, 194 Myr, 326 Myr, 300 Myr and 360 Myr, respectively. The overall e-folding times presented in this thesis are comparable to values obtained in other numerical experiments. Hanasz et al. (2006, 2009a) made shearing box simulations of the cosmic ray driven dynamo and found that the e-folding timescale in normal spiral galaxies is about 150 – 250 Myr. Very similar results were presented by Gressel et al. (2008) who made galactic dynamo simulations in the box model and took into account turbulent ISM driven by multiple clustered SNe explosions. The box simulations of Siejkowski et al. (2010) showed that the exponential growth of the magnetic field in irregular galaxies is slower than in the case of spiral galaxies and ranges between 300 Myr and 600 Myr. In all shearing box experiments the e-folding time of the amplification mechanism shows only a minor dependence on the SN activity. Additionally, the time scale of the exponential growth of the large scale magnetic field in global simulations of the cosmic ray driven dynamo in normal spiral galaxies (Hanasz et al. 2009b) is 270 Myr.

The mean pitch angle calculated in simulations of the barred galaxy varies between $-6°$ and $-13°$. These values are smaller than the observed values by up to $-30°$, however similar results were also found by Hanasz et al. (2006), who estimated pitch angles to be $\sim 5°$. Obtained values of pitch angles in the barred galaxy simulations are almost independent of the SN frequency. On the other hand, the SN activity has significant influence on the overall rate of the mass outflow.

The mass outflow rate caused by galactic winds produced during SNe explosions in the barred galaxy simulations ranges from 0.6 to 4.7 $M_{\odot}\,\mathrm{yr}^{-1}$. The overall rate of the mass outflow grows with the increasing SN activity in the galactic disk. Galactic scale outflows (galactic winds) from galactic disks are common phenomena and can be observed both in nearby galaxies (Tüllmann et al. 2006) and in the high-redshift universe (Tapken et al. 2007). Following observations, one of the main sources of galactic winds are SNe explosions (e.g. Matsubayash et al. 2009). According to the recent review of galactic winds (Bland-Hawthorn et al. 2007) the mass outflow rate ranges between 0.1 to 10 $M_{\odot}\,\mathrm{yr}^{-1}$. Additionally, the authors suggested that the outflow rate increases with increasing star formation rate. Results presented in this thesis support this statement and perfectly fit to the observed values.

In all models of the barred galaxy enhancements of the cosmic ray energy density correspond to regions with the highest gas density. Similar results were obtained by Hanasz et al. (2009b) who also studied numerically the cosmic ray driven dynamo but in the case of normal spiral galaxies.

Although the crucial aim of this thesis was to investigate the evolution of magnetic field structures, an agreement with the earlier, dynamical studies of this problem is also very important. All the basic dynamical features of the modelled barred galaxy are very similar to those constructed by Athanassoula (1992). The nonaxisymmetric gravitational potential of the bar triggers the formation of dust lanes along the leading edges of the bar and spiral arms propagating in the outer parts of the galactic disk, outside the bar. The same characteristic structures were obtained by many authors who studied the dynamical properties of barred galaxies (Athanassoula 1996; Otmianowska-Mazur et al. 2002; Romero-Gómez et al. 2006, 2007; Kulesza-Żydzik et al. 2009, 2010). What is more, the value of the SN rate has significant influence on the gas distribution in the barred galaxy. For the highest SN rate ($f_{SN} = 1/25\,\mathrm{yr}^{-1}$, model SD1) gaseous arms are shorter than those in models with lower SN activity. Moreover, the transport of gas from the outer part to the central part of the galaxy is most efficient for the model with the highest SN rate and decreases with decreasing SN activity. For model SD5, with the lowest SN rate ($f_{SN} = 1/500\,\mathrm{yr}^{-1}$) gaseous arms form outer ring whose position corresponds to the OLR location. Thus, the existence of the outer ring in barred galaxies is also determined by the SN activity.

4.2 Ringed galaxy NGC 4736 - successes and problems with the dynamo model

According to many theoretical and numerical studies (e.g. Schwarz 1981, 1985; Buta 1999) rings in barred galaxies are formed at the ILR and OLR. The distribution of the gas density through the disk centre (Figures 3.13, 3.14, 3.15, 3.16 and 3.17) as well as the column density (third and bottom rows in Figures 3.19, 3.20, 3.21, 3.22 and 3.23) obtained for all models of the ringed galaxy confirm this assumption. Indeed the outer ring is located between $R \sim 8$ kpc and $R \sim 11$ kpc and is obviously associated with the OLR which is located at $R = 7.7$ kpc (see e.g. model RS2 for the time step $t = 2.3$ Gyr in third panel in Figure 3.20 or model RS5 for the time step $t = 3.8$ Gyr in third panel in Figure 3.23). The outer ring is formed only due to the action of the oval. Since no strong torques act beyond the OLR the outer ring is not limited outside the OLR and is quite wide (~ 3 kpc). The inner ring is less wide than the outer one and extends between $R \sim 1.0$ kpc and $R \sim 2$ kpc (see e.g. model RS3 for the time step $t = 2.8$ Gyr in third panel in Figure 3.21). As in the case of the outer ring, the position of the inner ring corresponds to the OILR of the oval and the OLR of the bar, which are located at the same radius

$R = 1.8\,\mathrm{kpc}$.

Following Bosma et al. (1977), real observations of NGC 4736 show that the inner ring is located at $R \sim 1.6\,\mathrm{kpc}$ while the outer one at $R \sim 10.6\,\mathrm{kpc}$. Positions of rings obtained in this thesis are very similar to these found from observations of NGC 4736. Moreover, the shape of the two rings is slightly elliptical which corresponds to observations of NGC 4736. Another morphological regions of NGC 4736 identified by Bosma et al. (1977) are also reproduced in the presented simulations of the ringed galaxy. In fact, using the numerical model of the ringed galaxy NGC 4736 (presented in Section 2.2.2) I was able to get the following structures observed in NGC 4736:

- The central part of the galaxy within a radii $R < 0.6\,\mathrm{kpc}$ is very bright as in this region the small bar is present.
- The inner spiral structure which is induced by the nonaxisymmetrical gravitational potential of the small bar and is encircled by the inner ring. It ranges between $R \sim 0.6$ and $R \sim 1.5\,\mathrm{kpc}$ and it is best visible in the middle of simulations (see e.g. the time step $t = 1.9\,\mathrm{Gyr}$ in third row in Figure 3.22).
- The inner ring located between $R \sim 1.0\,\mathrm{kpc}$ and $R \sim 2.0\,\mathrm{kpc}$ thus close to the OLR of the inner bar and the OILR of the oval (see e.g. the time step $t = 2.3\,\mathrm{Gyr}$ in bottom row in Figure 3.20).
- The outer spiral structure which results from the nonaxisymmetrical gravitational potential of the oval. In different models the shape of gaseous arms is distorted or coherent.
- Between the oval disk and outer spiral arms the gap of lower surface density is visible.
- The outer faint ring which is formed as a result of tight winding of spiral arms and is located near the OLR and beyond (see e.g. the time step $t = 3.8\,\mathrm{Gyr}$ in bottom row in Figure 3.23).

The concept that Lindblad resonances are responsible for positions of the inner and outer rings in the ringed galaxy NGC 4736 is not new and was studied by many authors. The pioneering work in this field were the numerical studies by Gerin et al. (1991). The authors made N-body simulations and found that the nonaxisymmetrical gravitational potential of the oval perturbs the distribution of gas and gathers it in rings at Lindblad resonances. Contrary to my model, in their simulations the formation of the inner ring is very rapid while it takes much longer to form the outer one. On the other hand, similarly to results presented in this thesis, Gerin et al. (1991) showed that the inner ring disappears during further time evolution and that the outer ring is much wider than the inner one.

Mulder & Combes (1996) used the model of NGC 4736 proposed by Gerin et al. (1991) and increased the resolution in the inner part of the galaxy. Their results are very similar to those described by Gerin et al. (1991) and again confirm that the inner and outer rings are seen to form at the inner and outer Lindblad resonances.

Gu et al. (1996) made the test-particle simulation of NGC 4736 and obtained almost the same positions of the inner and outer rings as the ones presented in this thesis. Additionally, similarly to my results the outer ring in Gu et al. (1996) work is wide with radius $R \sim 7.5\,\mathrm{kpc}$ to $R \sim 10\,\mathrm{kpc}$.

The resent hydrodynamic simulations of NGC 4736 were made by Trujillo et al. (2009). They performed SPH simulations and used almost the same models of gravitational potentials as the ones I apply in this thesis. They found that the oval distortion can lead to creation of spiral arms and the inner ring which is located close to the inner Lindblad resonance.

The distribution and motion of gas in the ringed galaxy models strictly depend on the SN activity. The amount of gas accumulated in the inner ring grows with the increasing SN rate, thus for model RS1 ($f_{SN} = 1/50\,\mathrm{yr}^{-1}$) the inner ring is significantly denser than the inner ring in model RS5 ($f_{SN} = 1/500\,\mathrm{yr}^{-1}$). The opposite situation takes place in the case of the outer ring for which the highest amount of gas gathers for model RS5 ($f_{SN} = 1/500\,\mathrm{yr}^{-1}$) while the lowest for model RS1 ($f_{SN} = 1/50\,\mathrm{yr}^{-1}$). The moment in time in which the inner ring reaches its final shape is also determined by the SN activity. Namely, the faster formation of the inner ring is observed for model RS1 (with the highest SN rate) whereas the slowest one for model RS5 (with the lowest number of SNe explosions). Additionally, the transport of gas from the outer part to the central part of the ringed galaxy is the most efficient for the model with the highest SN rate and decreases with the decreasing SN activity.

The mass outflow rate, caused by galactic winds emerging from SNe explosions in the ringed galaxy simulations, grows with the increasing SN activity and ranges from 0.7 to 3.4 $M_{\odot}\,\mathrm{yr}^{-1}$. The obtained values are similar to these calculated for the barred galaxy simulations and are comparable with observations of real galaxies (Bland-Hawthorn et al. 2007). Moreover, in all models of the ringed galaxy regions where the cosmic ray energy density is enhanced correspond to areas with the highest gas density. Similar results are present in the case of the barred galaxy (see the previous Subsection 4.1) and in the case of normal spiral galaxies (Hanasz et al. 2009b).

A radio observation of NGC 4736 was made by Chyży & Buta (2008). In my simulations I was able to reproduce some of the observational properties of the magnetic field in NGC 4736. First of all, in both numerical simulations and in radio observations the total magnetic field is strongest in the inner ring. Chyży & Buta (2008) found that the total magnetic field in the starbursting ring varies from $18\,\mu\mathrm{G}$ to even $30\,\mu\mathrm{G}$. Using the cosmic ray driven dynamo model I obtained very similar values which depending on the model range between 17.0 μG (model RS5 with the lowest SN rate) to 33.1 μG (model RS1 with the highest SN activity, see Table 3.4). There is also a good agreement between the mean total magnetic field estimated by Chyży & Buta (2008) and the one calculated for the modelled ringed galaxy. In fact, Chyży & Buta (2008) suggested that the total mean field in NGC 4736 is equal to 17 μG, whereas in my simulations this field is approximately $\sim 14\,\mu$G and it does not depend on the SN rate. Additionally, the cosmic ray driven dynamo is very efficient in the modelled ringed galaxy. The faster amplification occurs for model RS1 (with the highest SN activity), where the e-folding time equals 104 Myr. This very rapid growth of the total azimuthal flux causes that the magnetic field reaches the equipartition level at time $t \sim 1.8$ Gyr and confirms that the cosmic ray driven dynamo can be responsible for strong magnetic fields observed in early type galaxies.

The distribution of the Faraday rotation measure in NGC 4736 indicates that this galaxy possesses the large scale magnetic field which may result only from the dynamo action (Chyży & Buta 2008). The distribution of the toroidal magnetic field component obtained for modelled ringed galaxy (top and third rows in Figures 3.19, 3.20, 3.21, 3.22 and 3.23) confirms that the cosmic ray driven dynamo can produce the large scale magnetic field visible in observations of NGC 4736 as a coherent rotation measure pattern. The highly symmetric magnetic field observed in NGC 4736 can also be explained by the cosmic ray driven dynamo action. The large symmetry of the simulated magnetic field in NGC 4736 is visible in top and second rows in Figures 3.19, 3.20, 3.21, 3.22 and 3.23.

High sensitivity radio polarimetric data reveal a coherent magnetic spiral structure in the inner part of NGC 4736 (Chyży & Buta 2008). The polarized radio emission shows that the magnetic field in the central part of NGC 4736 does not follow the gas distribution. Indeed, B-vectors cross the inner ring without changing their direction and with a constant and large pitch angle of about $-35°$. Unfortunately, using the cosmic ray driven dynamo model the observed configuration of the polarized magnetic field cannot be reproduced. Face-on synthetic polarization maps (third and bottom rows in Figures 3.19, 3.20, 3.21, 3.22 and 3.23) indicate that magnetic vectors are aligned along the inner ring and follow the gas distribution. Additionally, the obtained values of the pitch angle (between $-6°$ and $-13°$, Table 3.4) are significantly smaller than these estimated from observations of NGC 4736 ($-35°$, Chyży & Buta (2008)).

The failure of the cosmic ray driven dynamo process in reproducing the structure of the polarized magnetic field in the inner part of the galaxy and large pitch angles may be explained by insufficient number of processes taken into account. Certainly, in NGC 4736 the galactic dynamo works and is responsible for most of the observational properties of the magnetic field. However, the coherent spiral structure in the inner part of the galaxy may be formed before the inner ring appears. When the inner ring is formed, the magnetic field vectors may not change their direction immediately. In fact, the magnetic field can "remember" past conditions in the galaxy (Wezgowiec et al. 2007). Moreover, the formation of the inner ring may not be related to secular evolutionary processes in the galaxy. Yu-Ting Wu (2010) made N-body simulations and suggested that rings may be formed during a head-on collision of a spiral galaxy and a dwarf galaxy. In that case the evolution of the galaxy may be described as follows. Before the collision, the spiral galaxy possesses a clear pattern of the ordered magnetic field of spiral shape created due to the galactic dynamo action. After the head-on interaction with the dwarf galaxy the inner ring can form gradually, while the magnetic field vectors still reveal a coherent spiral pattern and cross the inner ring without changing their direction. This situation is not permanent and after some time the magnetic field starts to be aligned along the inner ring. Unfortunately, this prediction is in disagreement with observations of NGC 4736 which show no signs of recent mergers or close interactions. In order to confirm these statements more numerical simulations including head-on collisions are needed. What is more, a larger sample of observations of the distribution of magnetic fields in ringed galaxies will also help to better understand all phenomena that lead to the magnetic field configuration in NGC 4736.

On the other hand, increasing the resolution of the presented simulations of the ringed galaxy NGC 4736 may drive to better results. Unfortunately, simulations with resolution two times larger than the one presented in this thesis require much longer computational time $\sim 300k$ CPU hours. In order to perform high-resolution simulations of NGC 4736 an access to the fastest supercomputers as well as the improvement of the Godunov code are needed.

Face-on polarization maps indicate that the polarized magnetic field is present in the whole modelled ringed galaxy (see third and bottom rows in Figures 3.19, 3.20, 3.21, 3.22 and 3.23). Although the magnetic field is visible in the gaseous arms during the whole simulation time, the drift of magnetic arms into the interarm region takes place only in the early phase of evolution in models RS1, RS2, RS3 and RS4. At later time steps, after $t = 1.0\,\mathrm{Gyr}$, no drift of the magnetic field, similar to that observed in the barred galaxy simulations, can be detected. It may be caused by very limited space between the oval and the outer ring which is insufficient to allow magnetic arms to drift into the interarm region.

Polarization vectors in the edge-on view reveal the so-called X-shaped structure (see vertical slices in third and bottom rows in Figures 3.19, 3.20, 3.21, 3.22 and 3.23). This configuration of the magnetic field results from a galactic wind action and is also observed in the barred galaxy simulations (to more precise description see the previous Section 4.1).

The even (quadrupole-type) symmetry of the magnetic field with respect to the galactic plane is visible in vertical slices in Figures 3.19, 3.20, 3.21, 3.22 and 3.23). The obtained symmetry is natural in the dynamo theory (e.g. Ruzmaikin et al. 1988) and has been observed in many galaxies (e.g. Beck 2009c; Heesen et al. 2009). It has also been obtained in numerical studies of the cosmic ray driven dynamo in barred galaxies (see the previous Section 4.1) and in normal spiral galaxies (Hanasz et al. 2009b).

Chapter 5

Summary and Conclusions

This thesis presents a sample of numerical simulations of the cosmic ray driven dynamo in barred and ringed galaxies. The main findings of this thesis are:

- The polarized radio emission visible in face-on synthetic polarization maps indicates that the cosmic ray driven dynamo may be responsible for many magnetic structures visible in real observations of barred galaxies.
- In the case of the simulated barred galaxy the drift of magnetic arms is observed during the whole simulation time. On the other hand, for simulations of the ringed galaxy, magnetic arms detach from gaseous arms and drift into the interarm space only during the early stage of evolution.
- The synthetic edge-on radio maps of polarized emission computed for barred and ringed galaxies show that the cosmic ray driven dynamo can reproduce the vertical magnetic field structures observed in edge-on barred and ringed galaxies.
- The large scale magnetic field grows in barred and ringed galaxies on a timescale comparable to that obtained for normal spiral and irregular galaxies. In the case of the simulated barred galaxy there is no significant dependence on the SN rate, while for simulations of the ringed galaxy the number of SNe explosions influences the growth rate of the magnetic field.
- The cosmic ray driven dynamo triggers a very fast exponential growth of the magnetic field in galaxies. Both in barred and ringed galaxies the faster amplification is obtained for the SN frequency $f_{SN} = 1/50\,\mathrm{yr}^{-1}$ and the corresponding e-folding time is 194 Myr and 104 Myr, respectively. The last value confirms that the cosmic ray driven dynamo may reproduce strong magnetic field even in early type galaxies.

- During the equipartition state the cosmic ray driven dynamo maintains the magnetic field in a steady state.
- Presented simulations show that the seed field of stellar origin is sufficiently strong to be amplified by the cosmic ray driven dynamo to values observed in real galaxies.
- In the case of the simulated barred galaxy, the average equipartition strength of the magnetic field and the maximum value of the total magnetic field in magnetic arms as well as in the bar are consistent with observational values.
- Both in simulations of the barred and the ringed galaxy the distribution of gas and cosmic ray energy density as well as the overall rate of mass outflow are determined by the SN activity.
- Using the numerical model of NGC 4736 presented in Section 2.2.2 it is possible to reproduce the observed gaseous structures of this galaxy, i.e., the inner ring which encircles the inner spiral structure, the outer spiral structure, the outer ring and the gap in density between the oval and the outer ring.
- The spiral coherent structure which does not follow the gas distribution in the inner ring in NGC 4736 cannot be reproduced using the cosmic ray driven dynamo model only. Another processes, such as galactic interactions, have to be taken into account. High-resolution simulations may also lead to better results.
- The total magnetic field in the inner ring as well as the mean magnetic field have values very similar to those observed in NGC 4736.
- In accordance with theoretical studies the quadrupole-like symmetry of the magnetic field is preferred in numerical studies of the galactic dynamo. The even symmetry of the magnetic field with respect to the midplane is visible in most of simulations of barred and ringed galaxies. Only in one model of the barred galaxy the odd symmetry of the magnetic field is observed.
- Magnetic field reversals are visible in barred and ringed galaxies' simulations. Depending on the model they can be observed during the whole simulation time or appear from time to time.

This thesis shows that the cosmic ray driven dynamo is a powerful mechanism for amplifying galactic magnetic fields. Using the cosmic ray driven dynamo many observational magnetic futures of barred and ringed galaxies can be reproduced. Additionally, the idea that the seed field may be of stellar origin was confirmed again in the presented studies. Prepared numerical simulations provide a good basis for further research.

Appendix A

Polarization maps

To obtain synthetic radio maps from simulations results at first I have to rotate the galactic disk to the position defined by an inclination and a position angle. Next I calculate the magnetic field component perpendicular to the line of sight $B_{\perp}$. In my model the line of sight corresponds to the z-direction which points towards an observer at infinity. Then the perpendicular component of the magnetic field in Cartesian coordinate system is given by $B_{\perp} = \sqrt{B_x^2 + B_y^2}$. The synchrotron emissivity ϵ_I can be written as

$$\epsilon_I \propto n_{e,cr} B_{\perp}^{(\gamma+1)/2}, \tag{A.1}$$

where γ is the energy spectral index of the relativistic electrons and $n_{e,cr}$ is the number density of cosmic ray electrons. I assume that the distribution of cosmic ray electrons is proportional to the energy density of cosmic rays e_{cr}. Then, the synchrotron emissivity is described as

$$\epsilon_I \propto e_{cr} B_{\perp}^{(\gamma+1)/2}. \tag{A.2}$$

The Faraday rotation ψ of polarized emission along the line of sight is given by equation

$$\psi = C\lambda^2 \int n_{e,th} B_{||} dz, \tag{A.3}$$

where dz is the small distance in the z direction, $B_{||} = B_z$ is the magnetic field component parallel to the line of sight, $C = 0.812\,\mathrm{rad\,m^{-2}\,cm^{3}\,\mu G^{-1}\,pc^{-1}}$ is the constant (see Ehle & Beck 1993), λ is the wavelength and $n_{e,th}$ is the number density of thermal electrons. I assume that the distribution of thermal electrons is proportional to gas density, then

$$\psi = 0.812\lambda^2 \int \rho B_z dz. \tag{A.4}$$

After computing ϵ_I and ψ I calculate Stokes parameters Q and U which are proportional to the following integrals along the line of sight (see Longair 1994, e.g.)

$$Q = \int \epsilon_I \cos(2\psi) dz, \tag{A.5}$$

$$U = \int \epsilon_I \sin(2\psi) dz. \tag{A.6}$$

Finally, I convolve the synthetic Stokes parameters with a Gaussian beam of HPBW of 40″ to qualitatively match the finite resolution of observed maps.

Appendix B

Cosmic ray transport in the Godunov code

The original version of the Godunov code written by Kowal et al. (2009) does not include several routines needed in my simulations, i.e. gravity (a module calculating gravitational potential produced by each component of a galaxy as well as a module responsible for disturbance of a gravitational potential by its nonaxisymmetrical part coming from the bar and/or the oval), the cosmic ray transport, or distribution of SNe remnants. All modules responsible for above processes were added to the Godunov code. The most important is algorithm which allows to use cosmic rays. The description of routines which calculate the cosmic ray transport in the Godunov code is reported below.

B.0.1 Incorporation of cosmic ray transport using Hanasz & Lesch (2003) method

The cosmic ray implementation to the Godunov code is based on the method proposed by Hanasz & Lesch (2003) which was adopted into the Zeus code (Stone & Norman 1992a,b) and the Piernik (Hanasz et al. 2009b) code. This algorithm was successfully tested in both codes by many authors working on galactic dynamo problems (Hanasz et al. 2004, 2009b; Otmianowska-Mazur et al. 2009; Siejkowski et al. 2010). Because this algorithm was precisely presented by Hanasz & Lesch (2003) here I only briefly describe the method, highlighting the differences between the Zeus and the Godunov code.

As mentioned in Section 2.1.2 the propagation of the cosmic ray component in the ISM is described by the diffusion-advection equation 2.7. Comparing this equation to the energy equation 2.3 one can notice that they are similar, except the diffusion term $\nabla(\hat{K}\nabla e_{cr})$. Thus, numerical algorithms of the cosmic ray and energy transport are almost the same and only the additional diffusion term in the cosmic ray transport requires an extra routine.

The numerical algorithm which incorporates the diffusion of cosmic rays along the magnetic field lines can be divided into few steps. All steps are calculated separately for each cell faces, what results from positions of vector field components in numerical codes. Namely, to satisfy the $\nabla \cdot \vec{B} = 0$ to machine precision the magnetic field is located at cell interfaces. The correct centering of the magnetic field is crucial for any numerical simulations and it is slightly different in the Zeus and the Godunove code. Lets assume that cell centers are denoted by $(i, j, k) \equiv (x_i, y_j, z_k)$, then the magnetic field in the Zeus code is stored in arrays

$$\begin{aligned} B_x(i, j, k) &= B^x_{i-1/2,j,k}, \qquad (B.1)\\ B_y(i, j, k) &= B^y_{i,j-1/2,k},\\ B_z(i, j, k) &= B^z_{i,j,k-1/2}, \end{aligned}$$

while for the Godunov code the position of the magnetic field is given by

$$\begin{aligned} B_x(i, j, k) &= B^x_{i+1/2,j,k}, \qquad (B.2)\\ B_y(i, j, k) &= B^y_{i,j+1/2,k},\\ B_z(i, j, k) &= B^z_{i,j,k+1/2}. \end{aligned}$$

This little difference in the Zeus and the Godunov code causes that the algorithm proposed by Hanasz & Lesch (2003) needs minor modifications, which are presented below.

At first step the Godunov code computes the diffusion tensor $K_{ij} = K_\perp \delta_{ij} + (K_\parallel - K_\perp) n_i n_j$, where $K_\perp$ and $K_\parallel$ are parallel and perpendicular (with respect to the local magnetic field direction) cosmic ray diffusion coefficients and $n_i = B_i/B$ are components of the unit vectors tangent to magnetic field lines. The magnetic field component on x direction[1] faces in the Godunov code is given by

$$\begin{aligned} B_x(i, j, k) = B_x(i, j, k), & \qquad (B.3)\\ &+0.25(B_y(i, j, k) + B_y(i + 1, j, k) + B_y(i + 1, j - 1, k) + B_y(i, j - 1, k))\\ &+0.25(B_z(i, j, k) + B_z(i + 1, j, k) + B_z(i + 1, j, k - 1) + B_z(i, j, k - 1)). \end{aligned}$$

In the next step the gradient of cosmic ray energy density is calculated. In the Godunov code the cosmic ray energy density is positioned at the center of each cell. Thus, to compute cosmic-ray diffusive fluxes across cell interfaces the cosmic ray energy density should be interpolated from the cell center to the corresponding cell interface. Additionally, for stability of the whole algorithm in the Godunov code the monotinization of

[1] The magnetic field component on y and z directions faces is computed in the analogous way.

derivatives is applied. Then, the gradient of cosmic ray energy density in the x-direction[2] is given by

$$\nabla e_{cr}(i,j,k) = \frac{\partial e_{cr}(i,j,k)}{\partial x} + \frac{\partial e_{cr}(i,j,k)}{\partial y} + \frac{\partial e_{cr}(i,j,k)}{\partial z}. \tag{B.4}$$

The corresponding derivatives can be written in the form

$$\frac{\partial e_{cr}(i,j,k)}{\partial x} = \frac{e_{cr}(i+1,j,k) - e_{cr}(i,j,k)}{x(i) - x(i-1)}, \tag{B.5}$$

$$\begin{aligned}\frac{\partial e_{cr}(i,j,k)}{\partial y} &= \frac{1}{4}\left(\frac{\partial^l e_{cr}(i,j,k)}{\partial^l y} + \frac{\partial^r e_{cr}(i,j,k)}{\partial^r y}\right) \\ &\quad \times\left(1 + \left(1, \frac{\partial^l e_{cr}(i,j,k)}{\partial^l y}\frac{\partial^r e_{cr}(i,j,k)}{\partial^r y}\right)\right),\end{aligned} \tag{B.6}$$

$$\begin{aligned}\frac{\partial e_{cr}(i,j,k)}{\partial z} &= \frac{1}{4}\left(\frac{\partial^l e_{cr}(i,j,k)}{\partial^l z} + \frac{\partial^r e_{cr}(i,j,k)}{\partial^r z}\right) \\ &\quad \times\left(1 + \left(1, \frac{\partial^l e_{cr}(i,j,k)}{\partial^l z}\frac{\partial^r e_{cr}(i,j,k)}{\partial^r z}\right)\right),\end{aligned} \tag{B.7}$$

where left and right derivatives are given by

$$\frac{\partial^l e_{cr}(i,j,k)}{\partial^l y} = \frac{1}{2}\frac{e_{cr}(i,j+1,k) - e_{cr}(i,j,k) + e_{cr}(i+1,j+1,k) - e_{cr}(i+1,j,k)}{y(j) - y(j-1)}, \tag{B.8}$$

$$\frac{\partial^r e_{cr}(i,j,k)}{\partial^r y} = \frac{1}{2}\frac{e_{cr}(i,j,k) - e_{cr}(i,j-1,k) + e_{cr}(i+1,j,k) - e_{cr}(i+1,j-1,k)}{y(j) - y(j-1)}, \tag{B.9}$$

$$\frac{\partial^l e_{cr}(i,j,k)}{\partial^l z} = \frac{1}{2}\frac{e_{cr}(i,j,k+1) - e_{cr}(i,j,k) + e_{cr}(i+1,j,k+1) - e_{cr}(i+1,j,k)}{z(k) - z(k-1)}, \tag{B.10}$$

$$\frac{\partial^r e_{cr}(i,j,k)}{\partial^r z} = \frac{1}{2}\frac{e_{cr}(i,j,k) - e_{cr}(i,j,k-1) + e_{cr}(i+1,j,k) - e_{cr}(i+1,j,k-1)}{z(k) - z(k-1)}. \tag{B.11}$$

The time step limit for the cosmic ray diffusion is calculated using the following stability condition

$$\Delta t_{cr} \le C_{cr}\frac{(\min(\Delta x, \Delta y, \Delta z)^2}{K}, \tag{B.12}$$

where $C_{cr} = 0.5$ is the Courant number corresponding to the diffusion problem.

The above limitation of the time step for the cosmic ray transport depends on the parallel diffusion coefficient $K_{\parallel}$. It means that using realistic values of the parallel diffusion coefficient $K_{\parallel}$ relatively very small time step is obtained. Therefore, to reduce the computational cost the diffusion term in Eqn. 2.7 can be calculated using implicit method. The iterative method of solving set of linear equations, the so-called biconjugate gradient

[2]The gradient of cosmic ray energy density on y and z directions faces is computed in the analogous way.

stabilized method of van der Vorst (1992), often abbreviated as BiCGSTAB, (see Appendix B.0.2) was added to the Godunov code by Grzegorz Kowal. Using this algorithm the time step is not limited by the parallel diffusion coefficient $K_{\|}$ and the computational cost as well as memory requirement are very low (see Appendix B.0.3). However, numerical simulations have shown that for high resolution cases the implicit method is unfortunately slower than the explicit one. To obtain the same accuracy of implicit and explicit methods in high resolution cases, the implicit method needs many iterations, what does not influence on the time step but significantly prolongs the computational time. Thus, in most of simulations the explicit method of solving the cosmic ray transport is used.

B.0.2 Implicit method - Unpreconditioned BiCGSTAB of Van der Vors

An iterative method of solving set of linear equations is based on iteration. At the start of the algorithm an initial estimation of parameters is assumed and next equations are solved. The newly obtained values of parameters are inserted back into equations and the process repeats until the desired approximate solution is reached. During each process the error in the approximate solution is reduced. The iterative method discussed here is the unpreconditioned biconjugate gradient stabilized (BiCGSTAB) method of van der Vorst (1992), which solves iteratively equations

$$\mathbf{A}\mathbf{x} = \mathbf{b}, \tag{B.13}$$

where $\mathbf{A}$ is a matrix, $\mathbf{b}$ is a source vector and $\mathbf{x}$ is a solution variable for which we seek the solution. BiCGSTAB starts with an initial guess x_0 which determines the true residual

$$\mathbf{r}_0 = \mathbf{b} - \mathbf{A}\mathbf{x}_0. \tag{B.14}$$

The arbitrary vector $\mathbf{r}_0$ is chosen to satisfy the relation

$$(\mathbf{r}_0, \mathbf{r}_0) \neq 0, \tag{B.15}$$

e.g. $\mathbf{r}_0 = \mathbf{r}_0$. In addition, the other variables are defined as:

$$\mathbf{v}_0 = \mathbf{p}_0 = 0, \qquad \rho_0 = \omega_0 = \alpha = 1. \tag{B.16}$$

To compute the approximate solution in each iteration step (from $i = 1$ to $i = imax$) the following sequence of operations are made

$$\rho_i = (\mathbf{r}_0, \mathbf{r}_{i-1}). \tag{B.17}$$

Then define

$$\beta = \left(\frac{\rho_i}{\rho_{i-1}}\right)\left(\frac{\alpha}{\omega_{i-1}}\right) \tag{B.18}$$

and solve $\mathbf{p}_i$ from

$$\mathbf{p}_i = \mathbf{r}_{i-1} + \beta(\mathbf{p}_{i-1} - \omega_i \mathbf{v}_{i-1}). \tag{B.19}$$

Next calculate

$$\mathbf{v}_i = \mathbf{A}\mathbf{p}_i \tag{B.20}$$

and

$$\alpha = \frac{\rho_i}{(\mathbf{r}_0, \mathbf{v}_i)}. \tag{B.21}$$

Solve $\mathbf{s}$ from

$$\mathbf{s} = \mathbf{r}_{i-1} - \alpha \mathbf{v}_i \tag{B.22}$$

and calculate

$$\mathbf{t} = \mathbf{A}\mathbf{s}. \tag{B.23}$$

Then the optimal value for ω_i is given by

$$\omega_i = \frac{(\mathbf{t}, \mathbf{s})}{(\mathbf{t}, \mathbf{t})}. \tag{B.24}$$

In each iteration step the approximation $\mathbf{x}_i$ is corrected by search correction

$$\mathbf{x}_i = \mathbf{x}_{i-1} + \alpha \mathbf{p}_i - \omega_i \mathbf{s}. \tag{B.25}$$

If $\mathbf{x}_i$ is accurate enough then the algorithm stops, otherwise

$$\mathbf{r}_i = \mathbf{s} - \omega_i \mathbf{t} \tag{B.26}$$

and the process repeats again. In the GODUNOV code for test problems the desired accuracy and the maximum iteration step are set to be 10^{-16} and 1000, respectively.

B.0.3 Test problems

Below I present test problems of the numerical algorithm for the cosmic ray diffusion-advection problem taken form Hanasz & Lesch (2003). From samples of test problems I made two: the active cosmic ray transport along an inclined magnetic field and the active cosmic ray transport in a vertically stratified atmosphere. All parameters as well as the initial configuration applied in both test problems are the same like these presented in Hanasz & Lesch (2003) and are not describe here again.

B.0.3.1 Active cosmic ray transport along an inclined magnetic field

In Figure B.1 the initial distribution of the cosmic ray energy density with magnetic field vectors (top panels) and the gas density with velocity field vectors (bottom panels) are shown. Middle and right panels in Figure B.1 correspond to explicit and implicit methods of solving the cosmic ray diffusion, respectively. The initial configuration of the cosmic

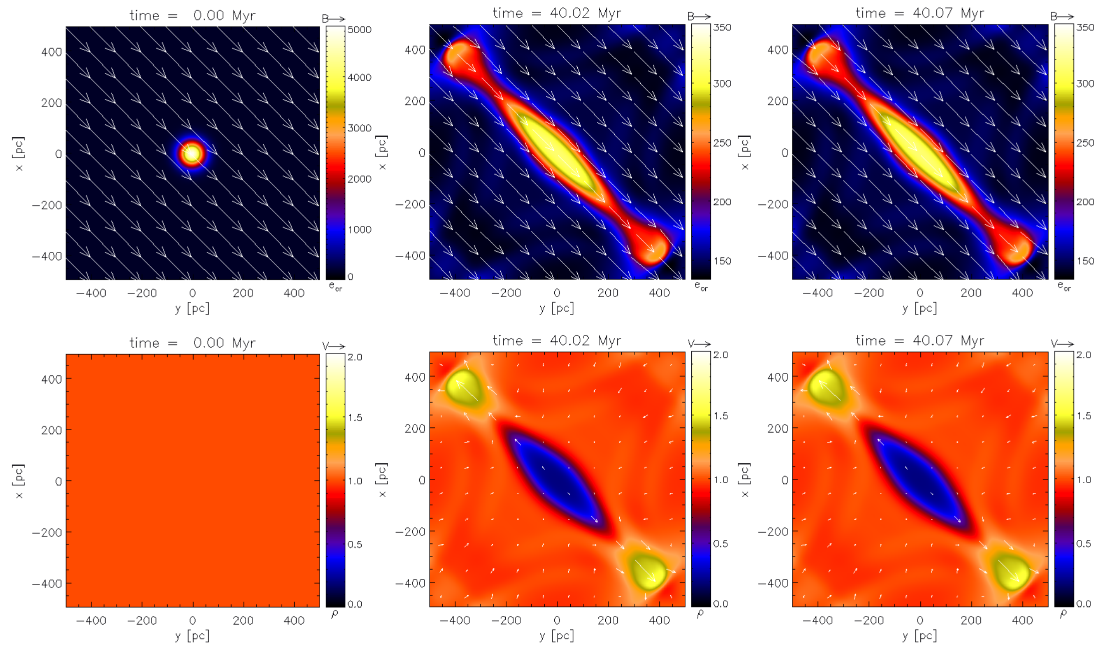

Figure B.1: The distribution of the cosmic ray energy density with overplotted vectors of magnetic field (top panels) and the distribution of the gas density with overplotted vectors of velocity field (bottom panels). Left panels represent the initial configuration of the cosmic ray energy density and gas density adopted to the active cosmic ray transport problem. Middle and right panels show results obtained for the active cosmic ray transport at $t = 40$ Myr for explicit (middle panels) and implicit (right panels) methods of solving the cosmic ray diffusion.

ray energy density is not uniform, but the enhancement of cosmic ray energy density is visible in the center of the computational box (the initial peak in this distribution represents a single SN explosion). On the other hand, initially the gas density distribution is uniform and no velocity field is present ($\vec{v} = 0.0$). At the time step $t = 40$ Myr, due to the coupling of cosmic rays to gas and magnetic field, these configurations change significantly. First of all, the velocity of the gas increases and gas accelerates preferentially along magnetic field lines. Additionally, gas is removed from the center of the computational box and accumulates outside the inner hole, upper-left and lower-right corners of bottom panels in Figure B.1. The acceleration and outflow of gas from the injection region is caused by the cosmic ray pressure. This pressure is also responsible for broadening of the cosmic ray profile across the magnetic field lines as well as for the enhancement of the cosmic ray energy density in regions where the velocity field is accelerated the most efficiently. What is more, no significant differences between implicit and explicit methods of solving the diffusion of cosmic rays is visible (compare middle and right panels in Figure B.1).

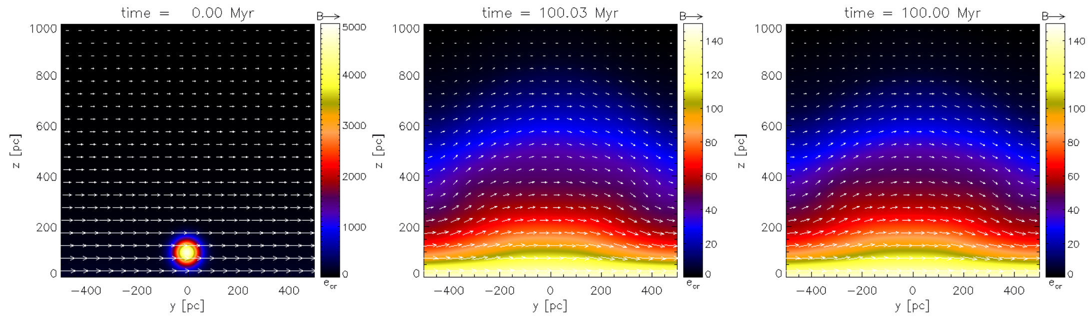

Figure B.2: The distribution of the cosmic ray energy density with overplotted vectors of the magnetic field in a gravitationally stratified galactic disk. The left panel represents the initial configuration of the cosmic ray energy density, middle and right panels show results obtained at the time step $t = 100$ Myr for explicit (middle panel) and implicit (right panel) methods of solving the cosmic ray diffusion.

B.0.3.2 Cosmic ray action in a gravitationally stratified galactic disk

This test problem is similar to that presented above, the only difference is that in this case a uniform vertical gravity is taken into account. As a results the initial distribution of the gas density is not uniform, but the gas is vertically stratified.

In Figure B.2 the evolution of the cosmic ray energy density in the case of explicit (middle panel) and explicit (right panel) methods is shown. Cosmic rays injected into the spherical volume of SN remnant diffuse anisotropically along the large-scale magnetic field and cause the formation of a fluxtube. Due to an excess of cosmic ray pressure the thermal gas outflows along the fluxtube from the SN injection center. The region becomes less dense than the surrounding medium and its central part starts to rise against the vertical gravity. At $t = 100$ Myr the flux tube forms a well defined Parker loop. The evolution of the cosmic ray energy density as well as the shape of the Parker loop are the same for implicit and explicit methods. However, the computational cost of the explicit method is eight times greater than for the implicit method.

Bibliography

Aguerri, J. A. L., Elias-Rosa, N., Corsini, E. M. & Muñoz-Tuñón, C., 2005, A&A, 434, 109

Athanassoula, E., 1992, MNRAS, 259, 345

Athanassoula, E., 1996, In: Barred Galaxies / Eds. Buta R., Crocker D. A., & Elmegreen B. G., ASP Conf. Proc. 91, 309

Athanassoula, E., Romero-Gómez, M., Masdemont, J. J., 2009, MNRAS, 394, 67

Barazza, F. D., Jogee, S. & Marinova, I., 2008, ApJ, 675, 1194

Beck, R., 1993, in The Cosmic Dynamo, eds. F. Krause, K-H Rädler, G.Rüdiger, IAU Symp. 157, Kluwer, Dordrecht, p.283-97

Beck, R. 2009, IAU Symp., 259, 3

Beck R., 2009, Astrophysics and Space Sciences Transactions, 5, 43

Beck, R., 2009, ApSS, 320, 77

Beck, R., Brandenburg, A., Moss, D., Shukurov, A. & Sokoloff, D. D., 1996, Annu. Rev. Astron. Astrophys., 34, 155

Beck, R., Shoutenkov, V., Ehle, M., Harnett, J. I., Haynes, R. F., Shukurov, A., Sokoloff, D. D. & Thierbach, M., 2002, A&A, 391, 83

Beck, R., Fletcher, A., Shukurov, A., Snodin, A., Sokoloff, D. D., Ehle, M., Moss, D. & Shoutenkov, V., 2005, A&A, 444, 739

Beck, R. & Krause, M., 2005, AN, 326, 414

Beckman, J. E., Varela, A. M., Muñoz-Tuñón, C., Vilchez, J. M. & Cepa, J., 1991, A&A, 245, 436

Berezinski, V. S., Bulanov, S. V., Dogiel, V. A., Ginzburg, V. L.,Ptuskin, V. S., Astrophysics of cosmic rays, Amsterdam:North-Holland, 1990.

Bernet, M. L., Miniati, F., Lilly, S. J., Kronberg, P. P. & Dessauges-Zavadsky, M., 2008, Nature, 454, 302

Bland-Hawthorn, J., Veilleux, S. & Cecil, G., 2007, Ap&SS, 311, 87

Block, D. L., Buta, R., Knapen, J. H., Elmegreen, D. M., Elmegreen, B. G., & Puerari, I., 2004, AJ, 128, 183

Bosma, A., van der Hulst, J. M. & Sullivan III, W.T., 1977, A&A, 57, 373

Brandenburg, A., Donner, K. J., Moss, D. et al., 1993, A&A, 271, 36

Buczilowski, U. R., Beck, R., 1991, A&A, 241, 47

Buta, R., 1986, ApJS, 61, 609

Buta, R., 1988, ApJS, 66, 233

Buta, R., 1999, Ap&SS, 269/270, 79

Buta, R. & Combes, F., 1996, Fundamentals of Cosmic Physics, 17, 95

Buta, R., Vasylyev, S., Salo, H. & Laurikainen, E., 2005, AJ, 130, 506

Buta, R., Corwin, H. G. & Odewahn, S. C., 2007, The de Vaucouleurs Atlas of Galaxies, Cambridge University Press

Buta, R., Knapen, J. H., Elmegreen, B. G., Salo, H., Laurikainen, E., Elmegreen, D. M., Puerari, I. & Block, D. L., 2009, AJ, 137, 4487

Chyży, K. T, Beck, R., Kohle, S. et al, 2000, A&A, 355, 128

Chyży, K. T., Knapik, J., Bomans, D. J., Klein, U., Beck, R., Soida, M. & Urbanik, M., 2003, A&A, 405, 513

Chyży, K. T & Buta, R. J., 2008, ApJ, 677, L17

Corsini, E. M., Aguerri, J. A. L. , Debattista, V. P., Pizzella, A., Barazza, F. D. & Jerjen, H., 2007, ApJ, 659, 121

Corsini, E. M., 2010, arXiv:1002.1245

Davis, L. J., Greenstein, J. L., 1951, ApJ, 114, 206

Del Zanna, L., Bucciantini, N. & Londrillo, P., 2003, A&A, 400, 397 de Vaucouleurs, G., 1963, ApJS, 8, 31

Durbala, A., Buta, R., Sulentic, J. W. & Verdes-Montenegro, L., 2009, MNRAS, 397, 1756

Duric, N., 1999, in ASP Conf. Ser. 168, New Perspectives on the Interstellar Medium, ed. A. R. Taylor, T. L. Landecker & G. Joncas (San Francisco: ASP), 161

Ehle, M., Beck, R., 1993, A&A, 273, 45

Elmegreen, B. G., Elmegreen, D. M., 1985, ApJ, 288, 438

Erwin, P., Sparke, L. S., 2002, AJ, 124, 65

Eskridge, P. B., Frogel, J. A., Pogge, R. W. et al., 2000, AJ, 119, 536

Evans, C. R. & Hawley, J. F., 1988, ApJ, 332, 659

Ferrers, N. M., 1877, Quart. J. Pure Appl. Math., 14, 1

Ferriére, K.,1998, ApJ, 497, 759

Fitt, A. J., & Alexander, P. 1993, MNRAS, 261, 445

Fletcher, A., Beck, R., Berkhuijsen, E. M., Horellou, C. & Shukurov, A., 2004, in How Does the Galaxy Work?, ed. E. J.Alfaro, et al. (Dordrecht: Kluwer), p. 299

Falceta-Gonçalves, D., Lazarian, A. & Houde, M., 2010, ApJ, 713, 1376

Giacalone, J., Jokipii, R. J., 1999, ApJ, 520, 204

Grouchy, R. D., Buta, R. J., Salo, H. & Laurikainen, E., 2010, AJ, 139, 2465

Gu, Q.-S., Liao, X.-H., Huang, J.-H., Qu, Q.-Y. & Su, H.-J., 1996, A&A, 314,18

Geller, M. J., Huchra, J. P., 1983, ApJS, 52, 61

Gerin, M., Casoli, F. & Combes, F., 1991, A&A, 251,32

Gaensler, B. M., Haverkorn, M., Staveley-Smith, L. et al. 2005, Science, 307, 1610

Gressel, O., Elstner, D., Ziegler, U. & Rüdiger, G., 2008, A&A, 486, 35

Hanasz, M. & Lesch, H., 2000, ApJ, 543, 235

Hanasz, M. & Lesch, H., 2003, A&A, 412, 331

Hanasz, M., Kowal, G., Otmianowska-Mazur, K. & Lesch, H., 2004, ApJ, 605, L33

Hanasz, M., Kowal, G., Otmianowska-Mazur, K. & Lesch, H. 2006, AN, 327, 469

Hanasz, M., Otmianowska-Mazur , K., Kowal, G. & Lesch, H., 2009a, A&A498, 335

Hanasz, M., Wóltański, D. & Kowalik, K., 2009b, ApJ, 706, 155

Harnett, J., Ehle, M., Fletcher, A., Beck, R., Haynes, R., Ryder, S., Thierbach, M. & Wielebinski, R., 2004, 421, 571

Heesen, V., Krause, M., Beck, R. & Dettmar, R. 2009, A&A, 506, 1123

Hildebrand, R. H., Davidson, J. A., Dotson, J. L., Dowell, C. D., Novak, G. & Vaillancourt, J. E., 2000, PASP, 112, 1215

Hummel, E., Beck, R., 1995, A&A, 303, 691

Jackson, J. D. 1999, Classical Electrodynamics (3rd ed.; New York: Wiley)

Jones, T. W, Rudnick, L., Jun, B-I., Borkowski, K. J., Dubner, G. Frail, D. A., Kang, H., Kassim, N. E. & McCray, R., 1998, PASP, 110, 125

Kennicutt, R J., 1998, ApJ, 498, 541

Knapen, J. H., Shlosman, I. & Peletier, R. F., 2000, ApJ, 529, 93

Knapen, J. H., de Jong, R. S., Stedman, S. & Bramich, D. M., 2003, MNRAS, 344, 527

Knapen, J. H., 2010, arXiv:1005.0506v2

Kohno, K., Tosaki, T., Miura, R., et al., 2008, PASJ, 60, 457

Kormendy J., 1993, IAU Symp. 153, Galactic Bulges, Habing H., Dejonghe H. (eds.). Dordrecht, p. 209

Kowal, G., Lazarian, A., Vishniac, E. T. & Otmianowska-Mazur, K. 2009, ApJ, 700, 63

Kowalik, K.,Hanasz, M., YSC'14 Proceedings of Contributed Papers (eds. G. Ivashchenko, A. Golovin), pp. 49-53

Krause, M., 2003, in Radio Studies of Galactic Objects, Galaxies and AGNs, J.L. Han, X.H. Sun, J. Yang & R. Wielebinski (eds)., Acta Astronomica Sinica, 44

Krause, M., 2004, in The Magntetized Interstellar Medium, B. Uyaniker, W. Reich, R. Wielebinski (eds.), Conf. Proceed., Antalya

Krause, M., 2009, Rev. Mexicana Astron. Astrofis., 36, 25

Krause, M., Hummel, E. & Beck, R., 1989, A&A, 217, 4

Krause, M., Wielebinski, R. & Dumke, M., 2006, A&A, 448, 133

Kronberg, P. P., 1994, Reports on Progress in Physics, 57, 325

Kulesza-Żydzik, B., Kulpa-Dybeł, K., Otmianowska-Mazur, K., Kowal, G. & Soida, M., 2009, A&A, 498L, 21K

Kulesza-Żydzik, B., Kulpa-Dybeł, K., Otmianowska-Mazur, K., Soida, M. & Urbanik, M., 2010, A&A, 522, 61

Kulpa-Dybeł, K., Kowal, G., Otmianowska-Mazur, K., Lazarian, A.& Vishniac, E. T., 2010, A&A, 700, 63

Kulsrud, R. M. & Zweibel, E. G., 2008, Rept. Prog. Phys. 71, 0046901

Lazarian, A., & Vishniac, E. T., 1999, ApJ, 517, 700

Lindblad, P. O., 1960, Stockholms Observatorium Ann., Vol. 21, No. 4

Lindblad, P. A. B., Lindblad, P. O. & Athanassoula, E., 1996, A&A, 313, 65

Londrillo, P. & Del Zanna, L., 2000, ApJ, 530, 508

Longair M. S., 1994, High energy astrophysics, Cambridge University Press, Cambridge

Matsubayashi, K., Sugai, H., Hattori, T., Kawai, A., Ozaki, S., Kosugi, G., Ishigaki, T., Shimono, A., 2009, ApJ, 701, 1636

Marinova, I. & Jogee, S., 2007, ApJ, 659, 1176

Menéndez-Delmestre, K., Sheth, K., Schinnerer, E., Jarrett, T. H. & Scoville, N. Z., 2007, ApJ, 657, 790

Mignone, A. 2007, Journal of Computational Physics, 225, 1427

Miyamoto, M. & Nagai, R., 1975, PASJ, 27, 533

Möllenhoff, C., Matthias, M. & Gerhard, O. E., 1995, A&A, 301,359

Moss, D., Korpi, M., Rautiainen, P., Salo, H., 1998, A&A, 329, 895

Moss, D., Rautiainen, P., Salo, H., 1999, MNRAS, 303,125

Moss, D., Shukurov, A., Sokoloff, D., Beck, R., Fletcher, A., 2001, A&A, 380, 55

Moss, D., Snodin, A., Englmaier, P., Shukurov, A., Beck, R., Sokoloff, D., 2007, A&A, 465, 157

Moss D., Sokoloff, D., Beck, R. & Krause, M., 2010, A&A, 512, 61

Mulder, P. S. & van Driel, W., 1993, A&A, 272, 63

Mulder, P. S. & Combes, F., 1996, A&A, 313, 723

Odewahn, S. C., 1996, ASP Conf. Ser. 91: IAU Colloq. 157: Barred Galaxies, 91, 30

Otmianowska-Mazur, K., von Linden, S., Lesch, H., Skupniewicz, G., 1997, A&A, 323, 56

Otmianowska-Mazur, K., Elstner, D., Soida, M., Urbanik, M., 2002, A&A, 384, 48

Otmianowska-Mazur, K., Kowal, G. & Hanasz, M., 2007, ApJ, 668, 1100

Otmianowska-Mazur, K., Soida, M., Kulesza-Żydzik, B., Hanasz, M. & Kowal, G., 2009, ApJ, 693, 1

Pacholczyk, A. G., 1970, Series of Books in Astronomy and Astrophysics, San Francisco: Freeman, 1970

Parker, E. N., 1966, ApJ, 145, 811

Parker, E. N., 1967, ApJ, 149, 535

Parker, E. N., 1979, *Cosmical Magnetic Fields*, (Oxford, USA: Clarendon Press)

Parker, E. N., 1992, ApJ, 401, 137

Phillips, A. C., 1996, ASP Conf. Ser. 91: IAU Colloq. 157: Barred Galaxies, 91, 44

Piner, B. G., Stone, J. M., Teuben, P. J., 1995, ApJ, 449, 508

Price D. J. & Bate M. R., 2009, MNRAS, 398, 33

Rees, M. J., 1987, QJRAS, 28, 197

Reese, A. S., Williams, T. B., Sellwood, J. A., Barnes, E. I. & Powell, B. A., 2007, AJ, 133, 2846

Reynolds, S. P., 1996, ApJ, 459, L13

Robishaw, T., Quataert, E., & Heiles, C., 2008, ApJ, 680, 981

Rohde, R., Elstner, D. & Rüdiger, G., 1998, A&A, 329, 911

Romero-Gómez, M., E., Masdemont, J. J., Athanassoula & García-Gómez, C., 2006, A&A, 453, 39

Romero-Gómez, M., Athanassoula, E., Masdemont, J. J., García-Gómez, C., 2007, A&A, 472, 63

Ruzmaikin, A. A., Shukurov, A. M. & Sokoloff, D. D., 1988, Magnetic Fields of Galaxies, Kluwer, Dordrecht

Ryu, D., Kim, J., Hong, S. S. & Jones, T. W., 2003, ApJ, 589, 338

Salo, H., Laurikainen, E., Buta, R. & Knapen, J. H., 2010, ApJ, in press

Sandage, A., 1961, The Hubble Atlas of Galaxies (Washington DC: Carnegie Institution of Washington)

Sandage, A. & Bedke, J., 1988, Atlas of Galaxies, Washington DC

Schlickeiser, R. & Lerche, I., 1985, A&A, 151, 151

Schmidt, M., 1959, ApJ, 129, 243

Schwarz, M. P., R., 1981, ApJ, 247, 77

Schwarz, M. P., R., 1985, MNRAS, 212, 677

Seigar, M. S., Chorney, N. E. & James, P. A., 2003, MNRAS, 342, 1

Sellwood, J. A. & Wilkinson, A., 1993, Rep. Prog. Phys., 56, 173

Shlosman, I., Frank, J. & Begelman, M. C., 1989, Nature, 338, 45

Shukurov, A. 2002, Ap&SS , 281, 285

Siejkowski, H., Soida, M., Otmianowska-Mazur, K., Hanasz, M. & Bomans, D. J., 2010, A&A, 510, 97

Silchenko, O. K. &Moiseev, A. V., 2006. AJ, 131, 1336

Sofue, Y. & Takano, T., 1981., Publ. Astron. Soc. Jpn., 33, 47

Sofue Y., Fujimoto M. & Wielebiński R., 1986, ARA&A, 24, 459

Sofue, Y., Tutui, Y., Honma, M., Tomita, A., Takamiya, T., Koda, J. & Takeda, Y., 1999, ApJ, 523, 136

Soida, M., 2005, in The Magnetized Plasma in Galaxy Evolution, ed. K. T. Chyzy, K. Otmianowska-Mazur, M. Soida & R.-J. Dettmar, (Kraków: Jagiellonian Univ.), 185

Sokoloff, D., Shukurov, A. & Krause M., 1992, A&A, 264, 396

Stone, J. M. & Norman, M. L., 1992a, ApJs, 80, 753

Stone, J. M. & Norman, M. L., 1992b, ApJs, 80, 791

Strong, A. W., Moskalenko, I. V. & Ptuskin, V. S., 2007, Annu. Rev. Nucl. Part. Sci., 57, 285

Subramanian, K., 2010, AN, 331, 110

Syrovatskii, S., 1970, in Interstellar Gas Dynamics, ed. H. Habing, IAU Symp. 39, Dordrecht, Holland, D. Reidel Pub. Co., 192

Tapken, C., Appenzeller, I., Noll, S., Richling, S., Heidt, J., Meinköhn, E. & Mehlert, D., 2007, A&A, 467, 63

Toomre, A., 1969, ApJ, 158, 899

Tremaine, S. & Weinberg, M. D. 1984, ApJ, 282, L5

Trujillo, I., Martinez-Valpuesta, I., Martínez-Delgado, D., Peñarrubia, J., Gabany, R. J. & Pohlen, M., 2009, ApJ, 704, 618

Tubbs, A. D., 1982, ApJ, 255, 458

Tüllmann, R., Dettmar, R.-J., Soida, M., Urbanik, M. & Rossa, J., 2000, A&A, 364, L36

Tüllmann, R., Pietsch, W., Rossa, J., Breitschwerdt, D. & Dettmar, R.-J. 2006, A&A, 448, 43

Turner, M. S. & Widrow, L. M., 1988, Phys. Rev. D, 37, 2743

Quashnock, J. M., Loeb, A. & Spergel, D. N., 1989, ApJ, 344, L49

Valenzuela, O., Rhee, G., Klypin, A., Governato, F., Stinson, G., Quinn, T. & Wadsley, J., 2007, ApJ, 657, 773

van der Kruit, P. C., 1976, A&A, 52, 85

van der Vorst, H., SIAM Journal of Scientific and Statistical Computing, 1992, 13, 631

Vega Beltrán, J. C., Zeilinger, W. W., Amico, P., et al., 1998, A&AS, 131, 105

Waller, W. H., Fanelli, M. N., Keel, W. C. et al., 2001, AJ, 121, 1395

Wezgowiec, M., Urbanik, M., Vollmer, B., Beck, R., Chyzy, K. T., Soida, M. & Balkowski, C., 2007, A&A, 471, 93

Widrow, L. M., 2002, Rev. Mod. Phys., 74, 775

Xu, H., OShea, B.W., Collins, D.C., Norman, M.L., Li, H. & Li, S., 2008, ApJ, 688, L57

Yu-Ting Wu, 2010, in Astrophysical Dynamics: From Stars to Galaxies, IAU Symp. 271